The Dark Side of the Gravitational Force: Lessons from Astrophysics on Gravity, Black Holes, and Dark Matter

Kristofer M. Pardo

A Dissertation
Presented to the Faculty
of Princeton University
in Candidacy for the Degree
of Doctor of Philosophy

Recommended for Acceptance
by the Department of
Astrophysical Sciences
Adviser: Professor David N. Spergel

September 2019

Abstract

There remain several unanswered questions about gravity in our universe: Does general relativity accurately describe gravity? Do supermassive black holes ever merge? What is the dark matter? Can it be explained by an alternative theory of gravity? This dissertation develops several astrophysical tests that serve to further our understanding of gravity, black holes, and dark matter. The first section of the thesis develops two tests using gravitational waves: 1) using a recent gravitational wave event, GW170817, to place limits on extra spatial dimensions; 2) using a newly discovered supermassive black hole binary to place limits on the gravitational wave background and its implications for the 'final parsec problem'. The second half of this thesis develops three tests of alternative theories for the dark matter: 1) self-interacting dark matter using galaxy warps; 2) a specific modified gravity theory, Verlinde's Emergent Gravity theory, using isolated dwarf galaxy kinematics; 3) general modified gravity theories using the cosmic microwave background polarization spectrum and the low-redshift galaxy correlation function. As we enter the next era of galaxy survey data and gravitational wave observations, these tests and others like them will hopefully bring us closer to answering these questions about gravity and our universe.

Acknowledgements

The best part about finally finishing this thesis is having the opportunity to thank everyone who made it possible.

First and foremost, I would like to thank my adviser, David Spergel, for his guidance on this thesis and graduate school in general. This thesis would not have been possible without his support and great ideas. I feel very lucky to have had the chance to work with him.

I would also like to thank Andy Goulding and Jenny Greene. They have both been instrumental in my growth as a person and scientist since the first day I got to Princeton. I truly appreciate all of the advice and support they have both given me, especially during the tough times. I am so grateful that I had the chance to work with them, especially on the work that ended up in this dissertation. I want to especially thank Andy for being incredibly encouraging, while also pushing me to do my best.

I would like to thank my thesis committee members, David Spergel, Michael Strauss, Jo Dunkley, and Mariangela Lisanti, for their guidance throughout the last few years. I would also like to thank my readers, Michael Strauss and Matias Zaldarriaga, for taking the time to read this dissertation and give helpful comments. I am also very grateful to Bhuv Jain for traveling to Princeton to serve on my dissertation defense committee.

Over the last few years, I have had the pleasure of working with many external collaborators on projects. I would like to especially thank Maya Fishbach, Daniel Holz, Harry Desmond, Pedro Ferreira, Jason Rhodes, Tim Eifler, Elizabeth Krause, and Phil Bull for teaching me so much through these experiences.

I would not have made it to graduate school at all without the wonderful mentors and teachers I had in grade school and my undergraduate years. I would like to thank my undergraduate adviser, Bill Baker, who has been incredibly supportive during my time at Furman and since. I am also especially appreciative of Ed Bertschinger – I would not be here today without him. Ed spent many hours working with me during the summers of 2013 and 2014, and I can never thank him enough for his support and encouragement during that time.

Many people and animals contributed to the fond memories I have made at Princeton. Thank you to everyone at Forbes College, especially my first year of ‘zees’, Michael Hecht, and fellow RGS Jenn Kasbohm, for making Forbes a home for me here at Princeton. I would like to also thank all of the perfect doggos around Princeton, including Cosmo, Loki, and Tucker, for always wagging their tails and making my days brighter.

My time in Peyton was made especially enjoyable thanks to all of the other basement dwellers. First, I would like to thank Polly Strauss for her care and support – the graduate students are so lucky to have her. I am also very thankful to all of the older Peytonites (and honorary Peytonites), especially Simone Ferraro, Johnny Greco, Brandon & Carla Hensley, Cole Holcomb, Diane Loring, and Manu Schaan, for their friendship and for putting up with all of my questions over the years. Thanks to Ben Thorne, David Vartanyan, and Joshua Wallace for all of the solidarity over this last year as we applied for jobs and wrote up our dissertations. Finally, I’d like to thank all of the current graduate students, including Avery Bailey, Erin Flowers, Goni Halevi, Erin Kado-Fong, Christina Kreisch, Brianna Lacy, Lachlan Lancaster, Zack Li, Alwin Mao, Mackenzie Moody, Heather Prince, Amy Secunda, and especially Luke Bouma for making such a positive impact on the department and making my last few years in Peyton so fun.

To my friends, Andrea and Devan: thank you for your amazing friendship and support over the years. This thesis would not have happened without your encouraging FaceTime chats, cute cat pictures, and intercontinental visits.

Finally, I would like to thank my family. To my grandparents: thank you for your love and constant encouragement. To my little brother Eric: thank you for always making me laugh and for being so kind to me and everyone around you. To my parents: thank you for all of the support and unconditional love you have given me. I am incredibly grateful for your encouragement of my various interests and hobbies, and your infinite patience with my stubbornness. And last, but definitely not least, thank you to Misty for being the best dog we could have ever asked for – we all miss you.

For my parents, Tony & Nadja

Relation to Published Work

Many of the chapters in this dissertation have been published, submitted for publication, or are in preparation to be submitted. The results from some of these chapters has also been presented at conferences. The relevant publications and presentations are listed below.

- Chapter 2: *Limits on the number of spacetime dimensions from GW170817*
  Kris Pardo, Maya Fishback, Daniel Holz, & David Spergel, J. Cosmology Astropart. Phys., 07, 048 (2018).

- Chapter 3: *Discovery of a Close-separation Binary Quasar at the Heart of a z 0.2 Merging Galaxy and Its Implications for Low-frequency Gravitational Waves*
  Andy D. Goulding, Kris Pardo, Jenny E. Greene, Chiara M.F. Mingarelli, Kristina Nyland, & Michael A. Strauss, ApJL, 879, 2, L21, (2019).

- Chapter 4: *Testing Self-Interacting Dark Matter with Galaxy Warps*
  Kris Pardo, Harry Desmond, Pedro G. Ferreira, submitted to Phys. Rev. D. Results from this chapter were also presented at the 233rd American Astronomical Society Meeting (2019).

- Chapter 5: *Testing Emergent Gravity with Isolated Dwarf Galaxies*
  Kris Pardo, submitted to J. Cosmology Astropart. Phys.. Results from this chapter were also presented at the UCLA Dark Matter Symposium (2018).

- Chapter 6: This chapter, written in collaboration with David Spergel, is being prepared for submission to a journal.

Contents

List of Tables

List of Figures

Chapter 1

Introduction

Over the last several centuries, we have gathered an incredible amount of data about our universe. From the data that we collect, we create theories for how the universe works. Of course, as soon as we create a new model for our universe, we soon find evidence that this may not be the full picture. For example, it was believed that Newtonian gravity could perfectly explain the planets' movements around the Sun. Then, Uranus' orbit was found to have certain irregularities that could not be accounted for by applying Newtonian gravity to the 7 known planets of the solar system at the time. This led astronomers to posit that there must be another planet that we had not yet identified (Le Verrier, 1846b,a) – this turned out to be Neptune (Galle, 1846; Adams, 1846). Mercury also has an irregular orbit that was noticed not long after (Le Verrier, 1859). Again, astronomers believed it was an extra planet, named Vulcan, that must be perturbing its orbit (Le Verrier, 1859); however, this was actual evidence for a departure from Newtonian gravity. Einstein's theory of general relativity (GR) beautifully predicts the correct deviation of Mercury's orbit from the Newtonian prediction (Misner et al., 2017; Nobili & Will, 1986).

The moral of these stories is two-fold: 1) data can illuminate new, totally unexpected, departures from our current models and we should continue to look for tools that can help us find these issues; 2) our first theories for how to explain phenomena may not always be correct – we must continue to test theories and develop new ones that may explain those phenomena that are not yet fully understood.

In this thesis, I will touch on both of these themes. The first half of my thesis is dedicated to gravitational waves, disturbances in spacetime caused by events like black hole mergers. These distortions of spacetime are a new way of seeing the universe that will hopefully lead to new, unexpected discoveries. I will discuss how we can use gravitational waves to learn more about the structure of spacetime and the dynamics of black holes. The second half of my dissertation focuses on dark matter. This substance is a signal that our theories for the universe may not be correct, and it is one for which we still do not have an adequate explanation. I will discuss how we have tested a few different theories for dark matter.

1.1 Gravitational Waves as a Tool for Testing New Theories

Until recently, all of our observations of the universe were made using electromagnetic signals (i.e. light). On September 14th, 2015, the Laser Interferometer Gravitational-Wave Observatory (LIGO) observed gravitational waves for the first time (Abbott et al., 2016). Gravitational waves are distortions of spacetime that are predicted by GR (Einstein, 1916, 1918). When extreme events, like the collision of two black holes, occur they release energy into spacetime itself, which leads to a propagating wave of distortions in spacetime. LIGO measures these distortions by monitoring the length of two ‘arms’ very precisely. Gravitational waves lengthen distances in one direction while shortening distances in the perpendicular direction. These waves are now another way we can observe the universe.

1.1.1 GW170817

On August 17th, 2017, a very special gravitational wave event occurred: two neutron stars merged with each other and produced *both* gravitational waves and light (Abbott et al., 2017c,b). This event, known as GW170817, allowed us to directly compare how gravitational waves and electromagnetic waves move through spacetime. In particular, we can use this event to place constraints on the damping of gravitational waves, which is predicted by some theories with extra spatial dimensions (Deffayet & Menou, 2007). These theories predict that gravitational waves should decrease in amplitude as they travel through spacetime; however, the same should not happen to photons. In GR, this does not occur, and so the distance to a gravitational wave event is related to the amplitude of the signal by[1] $\propto 1/\text{distance}$ (Misner et al., 2017). This formula does not account for any damping that may occur if gravity behaves differently than GR. Thus, if we use this formula and there is damping, we would predict the wrong distance with the gravitational waves – we would think it was further away than the true distance.

Without other observations, we would not be able to measure the true distance and we would not know if gravitational waves are damped. But, we also received photons from GW170817, which are not biased by the damping that affects gravitational waves in these theories. Thus, given a few other reasonable assumptions about our universe, we can exactly measure the distance to GW170817 using just the photons. If the gravitational wave distance is very different from this electromagnetic distance, then that would be evidence for damping of gravitational waves. In Chapter 2, I discuss how we use GW170817 to place constraints on these extra-dimensional theories.

---

[1] Note that this is the same as the electromagnetic relation; however, we normally see the equation for light in terms of *flux* instead of amplitude. The flux is related to the distance as $\propto 1/\text{distance}^2$.

1.1.2 Supermassive Black Holes and Nanohertz Gravitational Waves

The gravitational waves that LIGO measures are created by neutron stars and stellar mass black holes; but, these are not the only sources of gravitational waves in the universe. We know that most massive galaxies host supermassive black holes (SMBHs), black holes that are 1 million times the mass of the sun or greater, at their centers (e.g., Kauffmann et al., 2003). As galaxies evolve, they tend to merge with other galaxies to form even larger galaxies (Volonteri et al., 2003; Springel et al., 2005). We expect their supermassive black holes to also merge (Begelman et al., 1980). As these SMBHs get very close together ($\lesssim$ 0.1 pc) they emit gravitational waves at very low frequencies – more than a billion times lower than the frequencies LIGO measures. These can be measured by Pulsar Timing Arrays (PTAs), which monitor pulsars. These are rapidly spinning neutron stars that are incredibly accurate clocks. If a gravitational wave were to move through our galaxy, then we would see these clocks 'glitch' in a coherent pattern. Thus, by monitoring these pulsars, we hope to someday detect these low-frequency gravitational waves.

We think that our first detection of these nanoherz gravitational waves will not be of a single gravitational wave, but rather the collection of gravitational waves emitted by all SMBH pairs that are inspiralling towards each other (cf. Taylor et al., 2016). This creates what we call the gravitational wave background, which we expect to have a very specific signal (Hellings & Downs, 1983; Phinney, 2001). The PTAs around the world have been looking for this signal and have not yet found it (Arzoumanian et al., 2018).

In fact, it is unknown if these SMBH binaries can merge. At large separations, stars can easily help take away angular momentum from the SMBH binary orbit; however, once the binary is within 1 pc, it is unclear how they shed the extra energy (Begelman et al., 1980; Yu & Tremaine, 2003). This is referred to as the 'final parsec problem'. There are some suggestions for how this barrier can be overcome – either with gas or other orbital mechanics (i.e. three body interactions with additional SMBHs that enter the system through later mergers Bonetti et al., 2018; Ryu et al., 2018). Given that we do see evidence for extreme SMBHs in nearby galaxies, it is likely that the final parsec problem can be overcome in some way. Gravitational waves detected with PTAs will tell us definitively whether the final parsec problem is solved.

Meanwhile, astronomers have been looking for systems that might be emitting these gravitational waves – close-separation SMBHs (Rodriguez et al., 2006; Liu et al., 2013; Koss et al., 2018; Woo et al., 2014). So far, none have been found that contribute directly to the GWB. In Chapter 3, we discuss our discovery of an SMBH binary that points to a population of these binaries that would contribute to the GWB. This then lets us place bounds on the strength of this background and when we expect to measure it, given that mergers do occur. As we find more of these systems and finally detect the GWB, this will allow us to either rule out or confirm the final parsec problem.

1.2 Testing Dark Matter Theories

It is exciting to have gravitational waves as a new medium with which to search for evidence of new physics. However, there are still mysteries we have yet to explain from our observations with electromagnetic waves. Most of the matter in our universe is made of a substance that we cannot yet properly explain: dark matter. This was first noticed by observations that showed irregularities, like the irregular orbits of Uranus and Mercury. The effects of dark matter are apparent by looking at the velocities of galaxies in galaxy clusters (Zwicky, 1933) and stars within galaxies (Rubin et al., 1980). In both cases, the objects move much too fast given the number of stars and amount of gas we measure in these systems. This shows that there must be extra matter there. The 'dark' part of the name refers to how we cannot see it with light – it does not interact electromagnetically.

1.2.1 Cold Dark Matter – its successes and failures

The preferred theory for dark matter is cold dark matter (CDM), which is a particle that 'decoupled'[2] from all other matter at a very early stage in the Universe's history and does not interact with itself or any other matter. This seems to fit the data at large scales quite well (e.g., Spergel et al., 2003). However, we have yet to find any particles that fit this description (or any new particles outside of the Standard Model; e.g., Akerib et al., 2017; Aprile et al., 2018).

There are also hints of some issues with CDM at small scales (see Bullock & Boylan-Kolchin, 2017, for a recent review). The two classical problems here are the 'missing satellites' problem and the 'cusp versus core' problem. CDM predicts a large number of satellite galaxies around the Milky Way; however, we have so far only found a small portion of them. In addition, the satellites we seem to be missing are the largest ones, which we would expect to see most easily[3]. Although ,there is evidence that there may be no problem here at all (Kim et al., 2018). The other possible problem for CDM is the cusp versus core problem – CDM predicts 'cuspy' density profiles in the central parts of galaxies (Navarro et al., 1997, 2010). Observations of nearby dwarfs show that the density profiles only rise slowly in the central regions (e.g., McGaugh et al., 2001). However, this flattening of the density profile could also be due to baryonic feedback – if supernovae or SMBHs are able to push out large quantities of gas, this may affect the dark matter density profile (Mashchenko et al.,

---

[2] Decoupling refers to when a particle falls out of thermal equilibrium from the other particles in the universe. We expect all particles to be in thermal equilibrium at the 'beginning'. As the universe expands and cools down, particles will decouple once the temperature of the universe is less than the interaction energy between the particles and the rest of the particles in the universe.

[3] This is often referred to as a separate, but related problem: 'too big to fail' (Boylan-Kolchin et al., 2011).

2008). Regardless of the existence of these small scale issues, we have yet to find a suitable dark matter particle and we should be open to testing other types of particles or even non-particle theories that could explain dark matter.

1.2.2 Another Particle Explanation for Dark Matter

In the second half of this thesis, I will focus on tests of three types of dark matter theories. The first is a common particle theory – self-interacting dark matter (SIDM). In this theory, the dark matter has self-interactions – in other words, it can scatter off of itself. SIDM was first proposed as a way of solving the small-scale problems with CDM mentioned above (Spergel & Steinhardt, 2000). By allowing for interactions amongst dark matter particles, it allows for the evaporation of halos and the thermalization (and subsequent coring) of halo centers. There have been many limits placed on self-interacting dark matter throughout the intervening decades (Gnedin & Ostriker, 2001; Markevitch et al., 2004; Randall et al., 2008; Miralda-Escudé, 2002). However, none have definitively ruled out this property of dark matter as an astrophysically impactful DM property. In Chapter 4, I discuss how we use galaxy shapes, specifically the warping of stellar disks, to place limits on the strength of DM self-interactions. We discuss how future data may let us finally rule out this property as astrophysically interesting.

1.2.3 Modified Gravity as an Explanation of Dark Matter

Another way of possibly explaining dark matter is by modifying GR. There is a long history of these types of theories, starting from Modified Newtonian Dynamics (MOND; Milgrom, 1983). These models have the attractive possibility that we do not need to account for another particle in our theories – gravity can be fully explained by the visible matter, as long as we have the correct theory for gravity. For the most part, these theories have fallen out of fashion because they fail to predict cosmological signatures well (e.g., Dodelson, 2011). In addition, the relativistic counterparts, such as TeVeS (Bekenstein, 2004), have recently been ruled out by GW170817, since they rely on the speed of gravitational waves differing from the speed of light (Ezquiaga & Zumalacárregui, 2017; Baker et al., 2017). Of course, until we have a definitive detection of a dark matter particle or definitive proof that modified gravity could never explain dark matter, it is worthwhile to consider these theories. The last two chapters of this thesis focus on modified gravity explanations for dark matter.

Recent years have seen some interesting new theories, such as Verlinde's Emergent Gravity (Verlinde, 2017). Like MOND, Emergent Gravity does not have a cosmology associated with it. In its current formulation, it specifies a force law that is applicable only in the nearby universe. In this case, one of the best tests of the theory involves using the rotation curves of dwarf galaxies, which are galaxies with 30% the stellar mass or less than the Milky Way. Most massive galaxies seem to have very close to the same ratio of dark matter to normal (baryonic) matter regardless of their stellar mass (Faber & Jackson, 1976; Tully & Fisher, 1977). However, dwarf galaxies do not seem to follow this trend. Modified gravity theories must then explain how dwarf galaxies with the same baryonic mass somehow show different dark matter effects. Chapter 5 focuses on testing Emergent Gravity with isolated dwarf galaxies.

Many modified gravity theories also have difficulties explaining the growth of structure in the universe – how structure evolves from the tiny fluctuations we see in the cosmic microwave background to the galaxies and galaxy clusters we see today. Dark matter is absolutely pivotal in this process and we have found that CDM explains this process well (Lifshitz, 1946; Peebles & Yu, 1970; Sunyaev & Zeldovich, 1970; Bond & Efstathiou, 1984). In the early universe, the temperature of the universe is very high and baryons are coupled to photons – in other words, baryons are constantly feeling pressure from all of the radiation. CDM does not interact with photons, so it is able to collapse into self-gravitating halos. The baryons attempt to fall toward these halos, but the radiation pressure of the photons pushes them out. Likewise, the photons feel the gravitational force of the CDM through their coupling to the baryons. This causes sound waves to form in the baryon and photon structures. These sounds waves, called baryonic acoustic oscillations (BAO), are seen as oscillations in both the cosmic microwave background and in the positioning of galaxies around us today. Although on very large scales the universe is homogeneous, we see an overdensity of galaxies on scales of about 150 Mpc. This exactly matches the predictions of CDM and is a hallmark of the theory. The penultimate chapter of this thesis, Chapter 6, focuses on how we can use the BAO signal to describe the necessary form any modified gravity trying to explain the dark matter must take.

The final chapter, Chapter 7, gives a brief summary of this dissertation, including the main takeaways from each of the previous chapters.

Chapter 2

GW170817 & the Propagation of Gravitational Waves

Gravitational wave (GW) events with electromagnetic (EM) counterparts are powerful tests of modified gravity theories. Importantly, such joint observations are sensitive to differences between the propagation of GW and EM waves through spacetime. The recent detection of the first multi-messenger GW system, GW170817 (Abbott et al., 2017c), allows us to constrain modified gravity in this way for the first time.

From the time delay between the electromagnetic and GW signals, powerful limits can be placed on the speed of GW propagation (Abbott et al., 2017b). Many papers have already discussed how this constrains specific modified gravity theories (e.g., Lombriser & Taylor, 2016; Lombriser & Lima, 2017; Ezquiaga & Zumalacárregui, 2017; Baker et al., 2017; Creminelli & Vernizzi, 2017; Visinelli et al., 2018; Sakstein & Jain, 2017; Nersisyan et al., 2018).

The independent distance measures of the GW source and its EM counterpart can also place constraints on the damping of GWs. Since GWs are standard sirens, we can directly extract the luminosity distance to the GW source (Schutz, 1986; Holz & Hughes, 2005; Dalal et al., 2006; Nissanke et al., 2010, 2013; Chen et al., 2018a). In addition, we can make an independent measurement of the distance to the source by measuring the redshift of the EM counterpart and using our knowledge of cosmology (in particular, the Hubble constant, since GW170817 is at low redshift) to convert the observed redshift into a luminosity distance. By comparing these two distances, we can place limits on the damping of GWs. A number of authors have discussed the power of gravitational waves sources to place these sorts of constraints (Nishizawa, 2018; Arai & Nishizawa, 2018; Belgacem et al., 2018; Amendola et al., 2018; Linder, 2018); in what follows we focus on general constraints provided by the recent observations of GW170817 and its associated EM counterpart.

In this chapter, we constrain GW damping by considering modifications to the signal's attenuation with luminosity distance. According to GR, the GW amplitude decreases inversely with luminosity distance. However, extra-dimensional theories of gravity with non-compact extra dimensions generally predict a deviation from this relationship. Comparing the luminosity distance of GW170817 extracted under the assumption of GR to the EM-measured distance to its host galaxy, NGC 4993, we find stringent constraints on theories with gravitational leakage. We use these limits to set bounds on the number of additional non-compact spacetime dimensions and characterize properties of the modifications, such as the screening scale and the lifetime of the graviton. Section 2.1 describes the waveforms that we consider and gives a qualitative description of our analysis. Section 2.2 describes our methods. Section 2.3 gives our results and explores other applications.

2.1 Gravitational leakage and gravitational waves

In this section, we summarize the effects of gravitational leakage on the GW waveform and its relation to higher-dimensional theories. We also give a qualitative introduction to how GW170817 constrains gravitational leakage. This section relies heavily on the work of Deffayet & Menou (2007).

In GR, the strain goes as:

$$h_{\mathrm{GR}} \propto \frac{1}{d_L}, \tag{2.1}$$

where d_L is the luminosity distance of the GW source. For a higher-dimensional theory where there is some leakage of gravity we would expect, due to flux conservation, damping of the wave in the form of a power-law(Deffayet & Menou, 2007):

$$h \propto \frac{1}{d_L^{\gamma}}, \tag{2.2}$$

where γ is related to the number of dimensions, D, by:

$$\gamma = \frac{D-2}{2}. \tag{2.3}$$

More generally, we may consider theories that have an associated screening scale, R_c. These theories behave like GR below this scale, but exhibit gravitational leakage above R_c. In such theories the GW strain scales as (Deffayet & Menou, 2007):

$$h \propto \frac{1}{d_L \left[1 + \left(\frac{d_L}{R_c}\right)^{n(D-4)/2}\right]^{1/n}}, \tag{2.4}$$

where n gives the transition steepness. This waveform reduces to Equation 2.2 for $d_L \gg R_c$.

Finally, we consider theories in which the graviton has a decay channel. In this case, the amplitude of the GW would scale as:

$$h \propto \frac{\exp\left[-d_L/R_g\right]}{d_L}, \tag{2.5}$$

where R_g is the 'decay-length' (i.e. the distance a graviton travels during its average lifetime).

If we assume that, outside of these overall damping factors, the waveforms remain unchanged from the predicted GR form, then the gravitational leakage would simply result in a measured d_L greater than the true d_L for the source (i.e. the GW would appear to have come from farther away because it would have a smaller amplitude in the detectors). An event only measured in GWs would not allow us to distinguish the measured d_L from the true value. However, GW170817 was also detected electromagnetically; thus, we have an independent measurement of the luminosity distance for this source. By comparing the measured GW distance and the measured EM distance, we can constrain the gravitational leakage parameter γ (defined in Equation 2.2) and therefore place limits on the number of spacetime dimensions, the screening scale, or the lifetime of the graviton. In this we implicitly assume that the luminosity distance inferred from EM observations is the true luminosity distance: $d_L^{\mathrm{EM}} = d_L$; in practice, our approach quantifies the difference between the EM and GW distance estimates, and is insensitive to the true value of d_L.

Since the GW170817 standard siren measurement of the Hubble constant is consistent with expectations (Abbott et al., 2017a), this implies that, for reasonable assumed values of the Hubble constant, the inferred GW and EM distances are similarly consistent. We therefore expect that general relativity provides an excellent description, and we would not expect strong evidence for gravitational leakage and extra dimensions. In what follows we quantify this expectation.

2.2 Method

To measure gravitational leakage, we compare the EM luminosity distance to the source, d_L^{EM}, with the GW luminosity distance, d_L^{GW}, extracted from the waveform under the assumption that GR is the correct theory of gravity. To find the EM luminosity distance to the source, we use Hubble's law to relate the host galaxy's "Hubble velocity", v_H, to its luminosity distance. In the nearby universe, this relationship can be approximated by:

$$v_H = H_0 d_L^{\mathrm{EM}}. \tag{2.6}$$

The Hubble velocity is the recessional velocity that the galaxy would have if it was stationary with respect to the Hubble flow. To find the Hubble velocity of the host galaxy NGC 4993, we follow Abbott et al. (2017a) and correct the recessional velocity of the galaxy group to which NGC 4993 belongs, ESO-508, by its peculiar velocity. The EM observables are then the measured recessional velocity, v_r, of the group of galaxies to which NGC 4993 belongs, and the measured peculiar velocity, $\langle v_p \rangle$, in the neighborhood of NGC 4993. We denote the true peculiar velocity by v_p, so that the true recessional velocity is the sum of v_H and v_p. We adopt the conservative uncertainty on v_p from Guidorzi et al. (2017), which sets the Hubble velocity to be $v_H = 3017 \pm 250$ km s^{-1}. Together with a prior measurement of the Hubble constant, the measured velocities, v_r and $\langle v_p \rangle$, yield a measurement of the EM luminosity distance to the system.

Meanwhile, the GW data, x_{GW}, gives the posterior probability of the GW luminosity distance, d_L^{GW}, marginalized over all other waveform parameters, except the sky position, which is fixed to the position of the optical counterpart. We recover the GW distance posterior from the LIGO-Virgo Collaboration's publicly available H_0 posterior samples (Abbott et al., 2017a). The H_0 posterior is given by marginalizing the joint probability of H_0, the GW distance posterior probability, $p(d_L^{\mathrm{GW}} \mid x_{\mathrm{GW}})$, and the velocities v_H and v_p, over all parameters except H_0 (Equation 9 of Abbott et al., 2017a). We recover the GW distance posterior (marginalized over inclination angles) from the H_0 posterior by deconvolving the v_r and v_p terms, which are given by Gaussians. We approximate the integral in Equation 9 of Abbott et al. (2017a) by

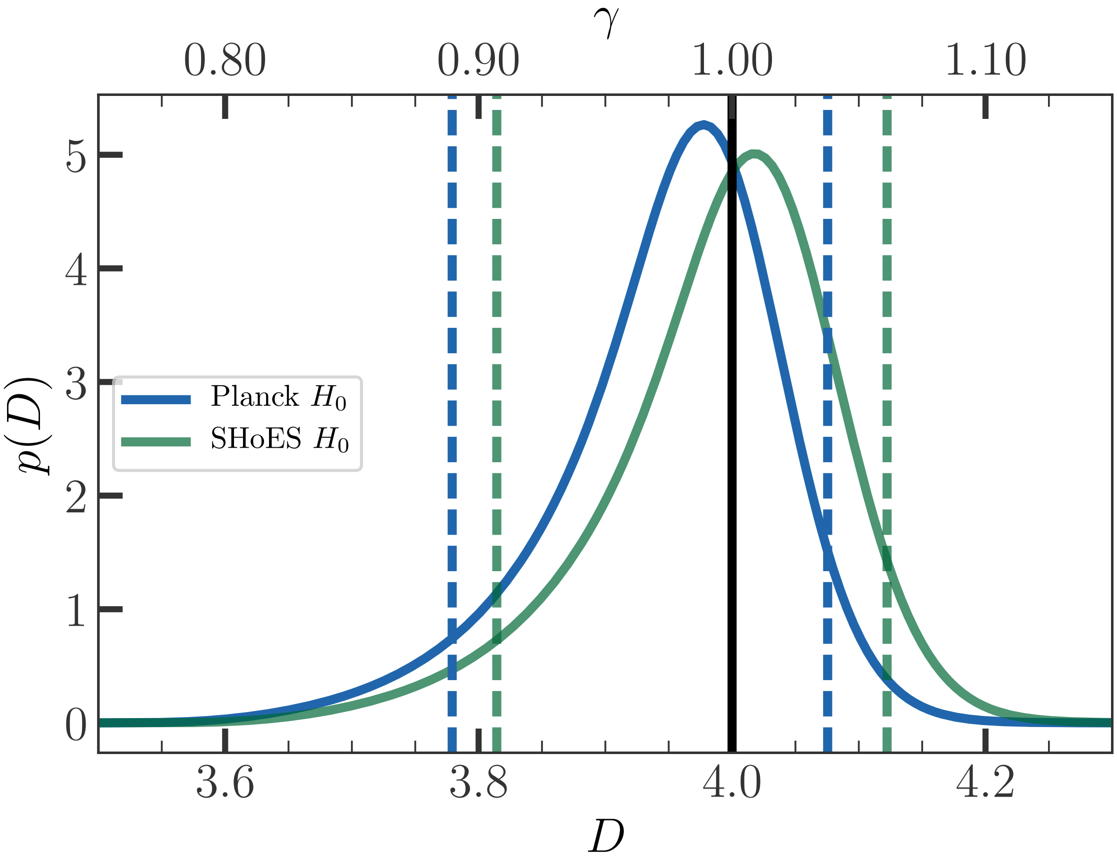

Figure 2.1: Posterior probability distribution for the number of spacetime dimensions, D, using the GW distance posterior to GW170817 and the measured Hubble velocity to its host galaxy, NGC 4993, assuming the H_0 measurements from Planck Collaboration et al. (2016) (blue curve) and Riess et al. (2016) (green curve). The dashed lines show the symmetric 90% credible intervals. The equivalent constraints on the damping factor, γ, are shown on the top axis. GW170817 constrains D to be very close to the GR value of $D = 4$ spacetime dimensions, denoted by the solid black line.

a Riemann sum. Then the term $p(x_{\mathrm{GW}} \mid d_L^{\mathrm{GW}}) p(d_L^{\mathrm{GW}})$ is obtained by solving a system of linear equations.

We carry out a Bayesian analysis to infer the posterior of the gravitational leakage parameter, γ, and the number of spacetime dimensions, D, given the GW and EM measurements described above. The statistical framework is described in detail in the Appendix.

H_0 prior km s^{-1} Mpc^{-1}	γ	D
$H_0 = 73.24 \pm 1.74$ (Riess et al., 2016)	$1.01^{+0.04}_{-0.05}$	$4.02^{+0.07}_{-0.10}$
$H_0 = 67.74 \pm 0.46$ (Planck Collaboration et al., 2016)	$0.99^{+0.03}_{-0.05}$	$3.98^{+0.07}_{-0.09}$

Table 2.1: Constraints on the damping parameter, γ, and the number of dimensions, D, assuming a waveform of the type Equation 2.2 from GW170817.

2.3 Results & Discussion

The posterior for D assuming a waveform with the scaling shown in Equations 2.2 and 2.3 is given in Figure 2.1. Since the results depend on the assumed H_0 prior, we compute the D posterior for both the SHoES H_0 value (Riess et al., 2016) and the Planck H_0 value (Planck Collaboration et al., 2016). The maximum a posteriori (MAP) values and minimal 68% credible interval values for γ and D are given in Table 2.1. As can be seen, the results are completely consistent with GR.

We can also use these constraints to place limits on waveforms with a scaling given by Equation 2.4. For the higher-dimensional theories that give rise to such waveforms, the d_L^{GW} measured under the assumption of GR will be greater than the true luminosity distance, d_L^{EM}. Thus, while our posterior for γ allows for both $\gamma > 1$ and $\gamma < 1$ (allowing for the relative damping of both the GW and EM signals), in the following analysis we restrict $\gamma > 1$. Using our joint posterior on d_L^{GW} and $d_L^{\mathrm{EM}} = (d_L^{\mathrm{GW}})^{1/\gamma}$ for GW170817, we can apply Equation 2.4 to constrain the screening radius, R_c:

$$R_c = \frac{d_L^{\mathrm{EM}}}{\left[\left(\frac{d_L^{\mathrm{GW}}}{d_L^{\mathrm{EM}}}\right)^n - 1\right]^{\frac{2}{n(D-4)}}}. \tag{2.7}$$

Thus, given our posterior samples for d_L^{GW} and γ (restricted to $\gamma > 1$), we can calculate the associated R_c for a fixed transition steepness, n, and number of dimensions, D. Marginalizing over H_0 and v_p, this gives us a joint posterior on R_c and d_L^{GW}.

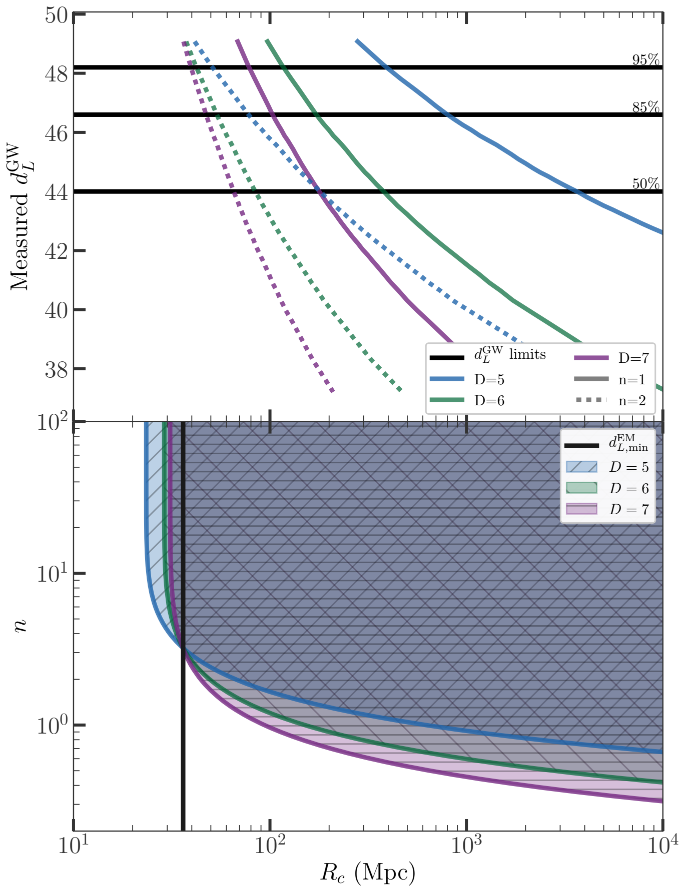

Figure 2.2: *Top:* Measured luminosity distance from GWs, $d_L^{\rm GW}$, versus the gravitational screening scale, R_c, for a number of spacetime dimensions given by $D = 5$ (blue), $D = 6$ (green), and $D = 7$ (purple). The solid lines assume a transition steepness of $n = 1$ and the dotted lines assume $n = 2$. The black horizontal lines give the 95%, 85% and 50% upper limits on $d_L^{\rm GW}$, after restricting our samples to $d_L^{\rm GW} > d_L^{\rm EM}$. *Bottom:* Allowed parameter regions for the transition steepness, n, and screening scale R_c, for $D = 5$ (blue), $D = 6$ (green), and $D = 7$ (purple), assuming a waveform of the type Equation 2.4. The vertical black line gives the 2.5% lower limit for $d_L^{\rm EM}$. We use the 5% lower limit for R_c to set these constraints.

Figure 2.2 (top panel) shows the correlation between $d_L^{\rm GW}$ and R_c for $D = 5$ (blue), $D = 6$ (green), and $D = 7$ (purple), and for $n = 1$ (solid) and $n = 2$ (dashed). As can be seen, a steeper transition (i.e. larger value of n) allows for theories to have a smaller screening scale; the steeper the transition, the closer the distance must be to the screening scale for a difference in the physics to be noticeable. Increasing numbers of dimensions also allow for smaller screening radii given the same transition steepness; however, the screening radii cannot be much smaller than the minimum EM distance. This is illustrated in the bottom panel of Figure 2.2, where we plot the allowed regions of parameter space within the n–R_c plane for $D = 5$–7. We use the 5% lower limit for R_c, which corresponds to the 95% upper limit on $d_L^{\rm GW}$ after restricting $d_L^{\rm GW} > d_L^{\rm EM}$, or the 97.5% upper limit for $d_L^{\rm GW}$ (and 2.5% lower limit for $d_L^{\rm EM}$) for the unrestricted samples. For $R_c \gtrsim d_{L,\mathrm{min}}^{\mathrm{EM}} = (d_{L,\mathrm{min}}^{\mathrm{GW}})^{1/\gamma_{\mathrm{max}}}$ (black, solid line), larger dimensions allow for softer transitions between GR and the higher-dimensional theories. If $R_c \ll d_{L,\mathrm{min}}^{\mathrm{EM}}$, then these higher dimensional theories are not allowed. As seen in the upper left of Figure 2.2, the minimum screening radius increases with increasing numbers of dimensions. These results show that theories with extra dimensions that have no screening mechanisms and that affect gravitational propagation at all scales are disfavored by GW170817. In addition, theories with screening mechanisms must have $R_c \gtrsim 20$ Mpc regardless of the transition steepness.

The final modification to GR we consider is theories in which the graviton has a finite lifetime. In such theories, the GW strain scales as Equation 2.5, so that setting $d_L = d_L^{\mathrm{EM}}$, the decay-length is given by:

$$R_g = \frac{d_L^{\mathrm{EM}}}{\log\left(d_L^{\mathrm{GW}}/d_L^{\mathrm{EM}}\right)}. \tag{2.8}$$

Using our posterior samples for d_L^{GW} and $d_L^{\mathrm{EM}} = (d_L^{\mathrm{GW}})^{1/\gamma}$, and again restricting $\gamma > 1$ to enforce $d_L^{\mathrm{GW}} > d_L^{\mathrm{EM}}$, we find a 5% lower limit for the decay length of the graviton of $R_g > 138\,\mathrm{Mpc}$. Since we know that gravitons must travel at the speed of light (Abbott et al., 2017b), we infer that the lifetime of the graviton can be given as $t = R_g/c > 4.50 \times 10^8\,\mathrm{yr}$.

We have only considered waveforms that are the same as GR, up to some overall multiplicative factor. It could be possible to evade these constraints by changing the waveforms in other ways. A full analysis of the LVC data using a more general framework (Agathos et al., 2014; Loutrel et al., 2014; Berti et al., 2015) would provide more insight into non-GR waveforms.

Our analysis relies on a crossing scale for the EM and GW luminosity distances. Equation 2.2 implicitly sets the crossing scale to 1 Mpc, assuming that $h \propto 1/d_L \times (1\ \mathrm{Mpc/d_L})^{\gamma-1}$. This ensures the correct units for the strain. From a theoretical perspective, the choice of scale is completely arbitrary; our choice of 1 Mpc is motivated by typical galaxy length scales. Figure 2.3 shows the effects on the posterior for γ as a function of different choices for the crossing scale. For scales that are comparable to the distance to GW170817, our constraints degrade considerably, since if the crossing occurs at precisely the distance of the binary then we would be unable to measure deviations as the theory would preclude them by assumption. A crossing scale that happened to be similar to the distance to this particular event would be quite fine-tuned. Scales smaller than a Mpc or larger than a Gpc give similar, or tighter, constraints to what we found above. As we accumulate GW events at different distances, we will be able to fit for the crossing scale directly, in addition to constraining γ.

We stress that our results do not hold for extra-dimensional theories with compact extra dimensions (e.g. string theory or the ADD model). The extra dimensions need to be at least on the order of the wavelength of the gravitational waves (~ 100 km) in order to have a damping effect. In addition, there may be complications for theories with larger extra dimensions. For example, we find that Randall-Sundrum II and DGP are poorly constrained by GW170817. In Randall-Sundrum II, the massless mode for the graviton is constrained to the 3D-brane; thus, energy cannot efficiently leak into extra non-compact dimension (Randall & Sundrum, 1999). For DGP, only very low frequency waves (i.e. ones with wavelengths on the scale of the cosmic horizon) are allowed to leak into the extra dimension (Dvali et al., 2001). Our calculation is a phenomenological one—it gives the total damping allowed considering a very general type of leakage for large extra dimensions. Applying these limits to specific theories is beyond the scope of this paper; however, these constraints should be considered carefully by extra-dimensional theories with dimensions of sizes ~ 100 km and greater.

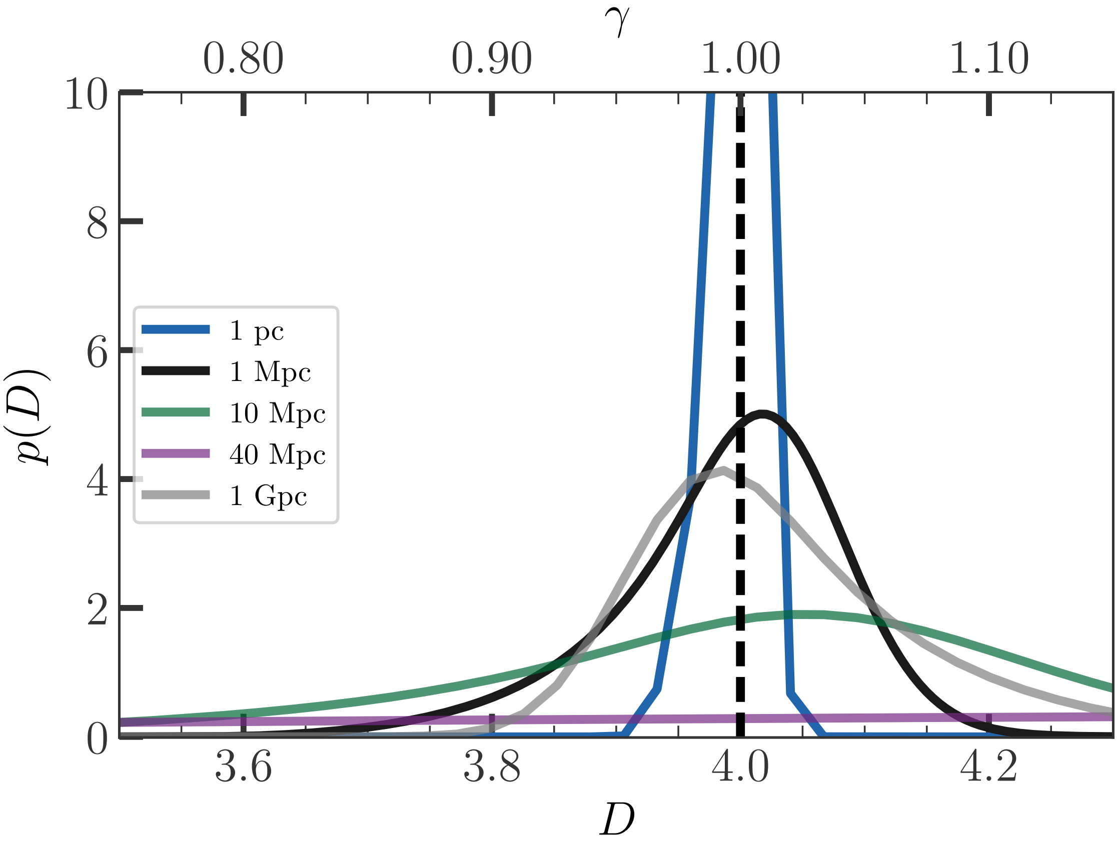

Figure 2.3: Posterior probability distribution for the number of spacetime dimensions, D, assuming different implicit crossing scales. The constraints degrade considerably for a crossing scale equal to the distance to the object, ~ 40 Mpc. However, scales either much smaller or larger than this show results that agree well with our choice of crossing scale of 1 Mpc.

In principle any higher-dimensional theories would allow for extra polarization modes (see, for example, Andriot & Lucena Gómez, 2017). However, the polarization constraints for GW170817 are quite poor, since the signal was not detected in Virgo and the LIGO detectors are aligned (Abbott et al., 2017c). Future events observed by three or more detectors would provide for tighter constraints on extra dimensions.

In this chapter, we have derived constraints from GW170817 on gravitational leakage by searching for a discrepancy between the measured gravitational luminosity distance, d_L^{GW}, and the measured EM luminosity distance, d_L^{EM}. We quantify the gravitational leakage via a damping parameter, γ, which can be related to the number of non-compact spacetime dimensions, D, through which gravity propagates. We find that $D = 4.02^{+0.07}_{-0.10}$ (for SHoES) and $D = 3.98^{+0.07}_{-0.09}$ (for Planck). In addition, we use these constraints to place bounds on extra-dimensional theories with screening mechanisms or decaying gravitons. We find the graviton decay length to be $R_g > 138\,\text{Mpc}$, implying a lifetime of the graviton of $t > 4.50 \times 10^8$ years. In summary, we find that GW170817 is fully consistent with GR.

Appendix

Statistical Model

Variable	Value	Variable	Value
d_L^{GW} prior	$\propto (d_L^{GW})^2$	v_r	3,327 km/s
γ prior	flat, [0.75, 1.15]	$\sigma_{v_r}, \sigma_{v_p}$	72, 239 km/s
H_0 prior (SHoES)	$\mathcal{N}(\mu_{H_0} = 73.24\ \text{km/s Mpc}^{-1},\ \sigma_{\mathrm{H_0}} = 1.74\ \text{km/s Mpc}^{-1})$	$\langle v_p \rangle$	310 km/s
H_0 prior (Planck)	$\mathcal{N}(\mu_{H_0} = 67.74\ \text{km/s Mpc}^{-1},\ \sigma_{\mathrm{H_0}} = 0.46\ \text{km/s Mpc}^{-1})$	v_p prior	flat, [-1,000,1,000] km/s

Table 2.2: Values & Priors Assumed for the MCMC Analysis

In the following, we describe the statistical framework assuming a waveform scaling as in Equation 2.2; however, this is easily extended to any other type of waveform that would cause the GW measurements and EM measurements of the luminosity distance to differ.

We can write the joint likelihood for the GW data, x_{GW}, and EM observables, $\langle v_p \rangle$ and v_r, given γ, H_0, d_L^{GW}, and v_p as:

$$p(x_{\mathrm{GW}}, \langle v_p \rangle, v_r \mid \gamma, H_0, d_L^{\mathrm{GW}}, v_p) = p(x_{\mathrm{GW}} \mid d_L^{\mathrm{GW}}) p(\langle v_p \rangle \mid v_p) p(v_r \mid \gamma, H_0, d_L^{\mathrm{GW}}, v_p)\ , \tag{2.9}$$

where we have assumed that all three observations, $x_{\rm GW}$, $\langle v_p \rangle$, and v_r are statistically independent. We can write the third factor in the above equation as:

$$p(v_r \mid \gamma, H_0, d_L^{\rm GW}, v_p) = p(v_r \mid v_r^t = v_p + H_0 d_L^{\rm EM} = v_p + H_0 (d_L^{\rm GW})^{1/\gamma}) \ , \tag{2.10}$$

where v_r^t is the true recessional velocity of the source. The likelihoods $p(\langle v_p \rangle \mid v_p)$ and $p(v_r \mid v_r^t)$ are assumed to be Gaussians (Abbott et al., 2017a), and are given as:

$$p(\langle v_p \rangle \mid v_p) \ = \ \mathcal{N}(v_p, \sigma_{v_p}^2)(\langle v_p \rangle) \ , \tag{2.11}$$

$$p(v_r \mid v_r^t) \ = \ \mathcal{N}(v_r^t, \sigma_{v_r}^2)(v_r) \ . \tag{2.12}$$

Applying Bayes' theorem, the joint posterior for γ, H_0, $d_L^{\rm GW}$, and v_p is then:

$$\begin{aligned} p(\gamma, H_0, d_L^{\rm GW}, v_p \mid x_{\rm GW}, \langle v_p \rangle, v_r) \propto p(x_{\rm GW} \mid d_L^{\rm GW}) p(\langle v_p \rangle \mid v_p) \\ \times\, p(v_r \mid \gamma, H_0, d_L^{\rm GW}, v_p) p_0(\gamma, H_0, d_L^{\rm GW}, v_p) \ . \end{aligned} \tag{2.13}$$

The posterior for γ is found by marginalizing over all other parameters:

$$\begin{aligned} p(\gamma \mid x_{\rm GW}, \langle v_p \rangle, v_r) = \frac{1}{p_{\rm det}(\gamma)} \int p(x_{\rm GW} \mid d_L^{\rm GW}) p(\langle v_p \rangle \mid v_p) \\ p(v_r \mid \gamma, H_0, d_L^{\rm GW}, v_p) p_0(\gamma, H_0, d_L^{\rm GW}, v_p) dH_0 dd_L^{\rm GW} dv_p \ , \end{aligned} \tag{2.14}$$

where $p_{\rm det}(\gamma)$ is a normalization term to account for selection effects and ensure that the integral over all detectable datasets integrates to unity. As shown below, this term is negligible for our analysis.

We choose the prior:

$$p_0(\gamma, H_0, d_L^{\rm GW}, v_p) = p_0(v_p) p_0(d_L^{\rm GW}) p_0(\gamma) p_0(H_0) \ . \tag{2.15}$$

This assumes a flat prior for the peculiar velocity, $p_0(v_p) \propto$ constant. For the GW distance, we use the default "volumetric" prior used in the LVC analysis, $p_0(d_L^{\mathrm{GW}}) \propto (d_L^{\mathrm{GW}})^2$. For the prior on the Hubble constant, $p_0(H_0)$, we take either the SHoES measurement or the Planck measurement. We choose the prior on γ to be flat, so the marginal posterior is proportional to the marginal likelihood. Our results are mildly sensitive to these prior choices; for example, taking a flat prior on d_L^{GW} shifts the posteriors towards slightly lower values of γ, so that the MAP and minimal 68% credible intervals become $1.00^{+0.04}_{-0.06}$ (SHoES H_0) and $0.98^{+0.04}_{-0.06}$ (Planck H_0) for a flat d_L^{GW} prior. (This alternative prior choice also leads to stricter lower limits on the screening scale R_c.) Except for the conservative value of $\sigma_{v_p} = 239$ km s^{-1} from Guidorzi et al. (2017), all other variable values and priors are the same as those given in Abbott et al. (2017a). All of our values and priors are given in Table 2.2.

The normalization term, $p_{\mathrm{det}}(\gamma)$, in Equation 2.14 is given by the integral of the marginal likelihood over all detectable datasets (Loredo, 2004; Mandel et al., 2019):

$$\begin{aligned} p_{\mathrm{det}}(\gamma) &= \int_{\mathrm{detectable}} p(x_{\mathrm{GW}}, \langle v_p \rangle, v_r \mid \gamma) dx_{\mathrm{GW}} d\langle v_p \rangle dv_r \\ &= \int_{\mathrm{detectable}} \int p(x_{\mathrm{GW}} \mid d_L^{\mathrm{GW}}) p(\langle v_p \rangle \mid v_p) p(v_r \mid \gamma, H_0, d_L^{\mathrm{GW}}, v_p) p_0(v_p) \\ &\times p_0(H_0) p_0(d_L^{\mathrm{GW}}) dH_0 dd_L^{\mathrm{GW}} dv_p dx_{\mathrm{GW}} d\langle v_p \rangle dv_r. \end{aligned} \tag{2.16}$$

We follow Abbott et al. (2017a) and neglect the EM selection effects. This is justified because the GW horizon for a BNS system during O2 was only 190 Mpc, whereas an EM counterpart would have been observable at distances greater than 400 Mpc. Thus, the integrals over detectable EM datasets, $\langle v_p \rangle$ and v_r integrate to unity. If we neglect the effects of GW redshifting on the detectability of the GW source (which is valid at these low redshifts), the GW selection effects are a function of GW luminosity distance alone. Defining:

$$\int_{\text{detectable } \mathrm{x}_{\mathrm{GW}}} p(x_{\mathrm{GW}} \mid d_L^{\mathrm{GW}}) dx_{\mathrm{GW}} \equiv p_{\mathrm{det}}(d_L^{\mathrm{GW}}) \ , \tag{2.17}$$

we have:

$$p_{\mathrm{det}}(\gamma) = \int p_{\mathrm{det}}(d_L^{\mathrm{GW}}) p_0(v_p) p_0(H_0) p_0(d_L^{\mathrm{GW}}) dH_0 dd_L^{\mathrm{GW}} dv_p \ . \tag{2.18}$$

The above equation is independent of γ, and so we can ignore this term in our analysis. However, if we had chosen to carry out the analysis by setting a prior on the redshift or v_H rather than GW distance, Equation 2.18 would have a γ dependence in the term $p_{\mathrm{det}}(d_L^{\mathrm{GW}} = (\frac{v_H}{H_0})^{\gamma})$, which varies significantly over the posterior support for γ. In this case, $p_{\mathrm{det}}(\gamma)$ cannot be neglected.

To compute the posterior for γ, we sample directly from the joint posterior given by Equation 2.13 with an MCMC analysis using the python package PyMC3 (Salvatier et al., 2016).

Chapter 3

A Binary Supermassive Black Hole System & the Stochastic Gravitationl Wave Background

Cosmological models of structure formation predict that galaxies undergo frequent mergers throughout their history (Volonteri et al., 2003; Springel et al., 2005). Supermassive black holes (SMBHs) from each progenitor quickly sink towards the central 0.1–1 kpc region of the merger remnant due to dynamical friction. This SMBH pair may eventually form a bound binary system capable of emitting gravitational waves (GWs) before final coalescence (Begelman et al., 1980). SMBH binaries with masses of $M_{\mathrm{BH}} \approx 10^8$–$10^9 M_\odot$ are expected to comprise the dominant contribution to the as-yet undetected GW background (GWB) signal at the nanohertz frequencies accessible to pulsar timing arrays (PTAs; Sesana et al. 2008; Burke-Spolaor et al. 2019). The current theoretical predictions on the precise amplitude and composition of the GWB vary dramatically, and are limited, in part, by the lack of overall empirical constraints on the occurrence of high-mass SMBH pairs.

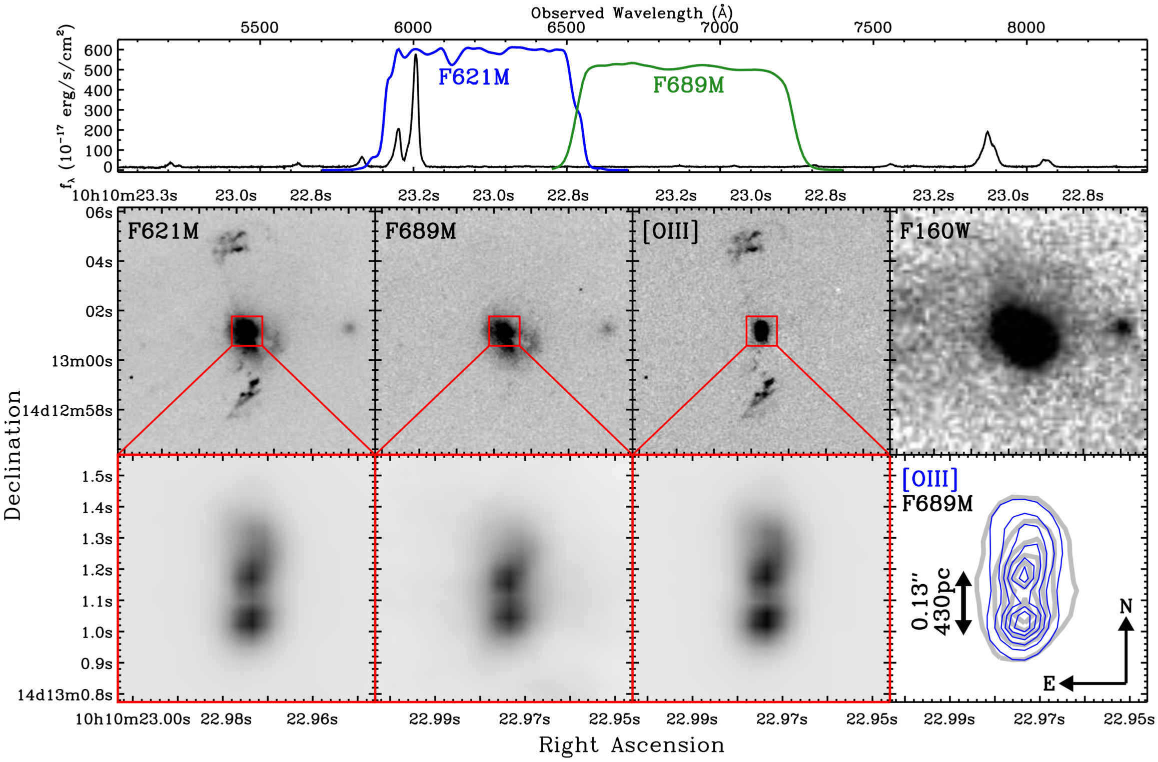

Figure 3.1: Analysis of the central region of J1010+1413. Upper panel: SDSS 2″ fiber spectrum, overlaid are the WFC3/UVIS transmission curves for the F612M (blue) and F689M (green) filters. Middle panels left to right: WFC3/UVIS medium-bands F621M; F689M; [OIII]=F621M–F689M; F160W. Lower panels left to right: zoom and contrast rescaling of the middle panels. Contours of F689M continuum (black) and [OIII] images (blue) are shown in the lower-right panel. Both the F689M stellar continuum-only image and the [OIII] images clearly show two distinct point sources, suggesting two nuclei each with their own accreting SMBHs.

Emission produced through accretion acts as a useful signpost for evidence of SMBHs. Indeed, extremely high-resolution radio observations have serendipitously identified very close separation sub-parsec scale SMBH binary candidates (Rodriguez et al., 2006). While there have been several claims of binary SMBHs in some nearby galaxies (e.g., Fabbiano et al. 2011), these have subsequently been challenged with expanded datasets and/or improved analysis techniques (e.g., Finlez et al. 2018 and references therein). AGN surveys have identified wider-separation (several to tens kpc) SMBH-pair candidates by harnessing highly-penetrating X-rays and follow-up with ground-based near-IR adaptive optics systems (Liu et al., 2013; Koss et al., 2018). Due to limitations in angular resolution, these investigations are typically performed at lower redshifts, where the AGN studied tend to be relatively low-luminosity ($L_{\rm AGN} < 10^{44}$ erg s^{-1}). Consequently, these dual SMBH systems are predisposed to lower masses ($M_{\rm BH} \approx 10^7 M_\odot$), often at kiloparsec separations (Liu et al., 2010; Woo et al., 2014), such as the well-studied nearby merging galaxy NGC 6240, which hosts two actively growing SMBHs separated by ~1 kpc (Müller-Sánchez et al., 2018). Systems such as NGC 6240 do not appreciably contribute to the GWB that will be detected in the PTA band due to their low $M_{\rm BH}$ (Sesana et al., 2008). Much larger volumes must be searched to find the most luminous quasars, and hence most massive binary BHs, that contribute to the PTA signal. Utilizing high spatial-resolution observations with the Hubble Space Telescope (*HST*), studies have begun to identify a more massive population of kpc-scale separation SMBH pairs through the detection of distinct multiple nuclear cores coincident with unresolved AGN emission (Xu & Komossa, 2009; Fu et al., 2012). However, to begin to place empirical constraints on the GWB we must characterize the number of $10^8 - 10^9 M_\odot$ SMBH pairs with sufficiently small separations that they may merge before the present day.

Here we present an observational anchor to predictions for a GWB signal that can be detected in the PTA band. SDSSJ101022.96+141300.9 (hereafter, J1010+1413) is a late-stage merging galaxy at $z \sim 0.198$ (angular scale of 3.27kpc/$''$) with high equivalent-width emission lines (Mullaney et al., 2013) in the Sloan Digital Sky Survey (SDSS; York et al., 2000). At mid-infrared wavelengths ($22\mu m$), it is one of the most luminous systems ($L_{\rm AGN} \gtrsim 6 \times 10^{46}$ erg s^{-1}) at $z \sim 0.2$ identified with the Wide-field Infrared Survey Explorer (WISE). Using high spatial resolution (0.03$''$/pixel) multi-band imaging from HST's Wide Field Camera 3 (WFC3) instrument, we identified two distinct quasar-produced [OIII]5007-emitting regions that are spatially co-incident with two nuclear stellar cores buried close to the center. These two point sources are separated by 0.13$''$, a projected separation of only 430 parsecs at the distance of

J1010+1413, providing strong evidence for a central SMBH pair at the heart of this merging galaxy.

3.1 Target Selection and Observations

J1010+1413 was initially characterized as having strong asymmetries in its [OIII]5007 emission line profile as part of an in-depth study of nearby accreting SMBHs identified in SDSS (Mullaney et al., 2013). It is one of the most luminous quasars at $z \sim 0.1$–0.2 based on both [OIII] ($L_{\text{[OIII],dered}} \sim 1.2 \times 10^{44}$erg s^{-1}) and 22$\mu$m emission. The central few kpc of J1010+1413 is strongly AGN dominated ([OIII]/H$\beta \sim 12.4$) and was previously found to be irregular and kinematically complex, with broad, spatially unresolved [OIII] and Hβ emission ($W_{80} \sim 1350 - 1450$ km s^{-1}) based upon Gemini-GMOS IFU data (Harrison et al., 2014).

3.1.1 HST medium & broad-band imaging

J1010+1413 was imaged on October 17 2017 with WFC3/IR in the F160W filter, and with the WFC3/UVIS instrument in two optical medium bands, F621M and F689M for a total of one orbit (Proposal:14730; PI:Goulding). Our F160W observation with a spatial resolution of $0.13''$/pixel provides a relatively clean measure of the stellar light (rest-frame 1.3μm). An azimuthally-symmetric surface brightness (SB) profile was constructed from the F160W image to measure the stellar light of J1010+1413. The SB profile is detected to $r \sim 7.1''$ ($\sim$ 23 kpc), and is dominated by inhomogeneous low SB emission beyond $r \sim 2.25''$, consistent with tidal debris from a merger event. We measure a total flux of $f_{160W} \sim 3.23 \pm 0.03 \times 10^{-12}$ erg s^{-1}cm^{-2}, i.e., a total luminosity of $L_{160} \sim 1.1 \times 10^{11} L_{\odot}$, from which we infer a total stellar mass of $M_{*} \sim 0.7$–$1.5 \times 10^{11} M_{\odot}$.

The WFC3/UVIS F621M observation ($0.04''$/pixel) provides a detailed image of the continuum galaxy light combined with emission from the AGN-dominated [OIII]4959+5007Å emission line doublet, which is redshifted into the filter. By contrast, the F689M filter covers no significant emission lines and thus only detects emission arising from the galaxy continuum. On small scales, the F689M filter image reveals two distinct and resolved stellar-continuum point sources that are separated by $0.13''$ in the nuclear region of J1010+1413 (Figure 3.1). The amplitudes of the two nuclear cores are very similar, 1:1.2, suggesting similar stellar masses but the two cores are not uniquely resolved in the F160W image due to the lower resolution and S/N.

We subtracted the F621M from the F689M image to investigate the spatial distribution of the combined [OIII] doublet emission, and test for the presence of two distinct narrow-line regions (NLR) in the center of J1010+1413. We solved for the marginal ($<0.02''$) astrometric offset between the two F621M and F689M filters, and normalized the flux-calibrated images to give a net-zero sum of the extended galaxy light. Within the central kpc region ($r\lesssim0.3''$), we identify two distinct [OIII]-emitting regions that are spatially co-incident with the two nuclear point sources observed in the F689M continuum image. We interpret this as evidence for two remnant cores from the galaxy merger that each possess a central accreting SMBH, producing two distinct [OIII]-luminous NLRs.

Using the [OIII] image, we confirm the presence of the extended emission line region at large radial scales of $r \sim 4$" (14 kpc), the kinematics of which was previously studied in Sun et al. (2017). Their previous Magellan IMACS spectroscopy shows that the extended [OIII] emission is kinematically cold and not necessarily an outflow from the central galaxy. Combined with our sensitive WFC3/UVIS observations, the large-scale [OIII] appears to be emitted from gas that was tidally stripped during the galaxy merger (Harrison et al., 2014), and is now being illuminated by the central quasars.

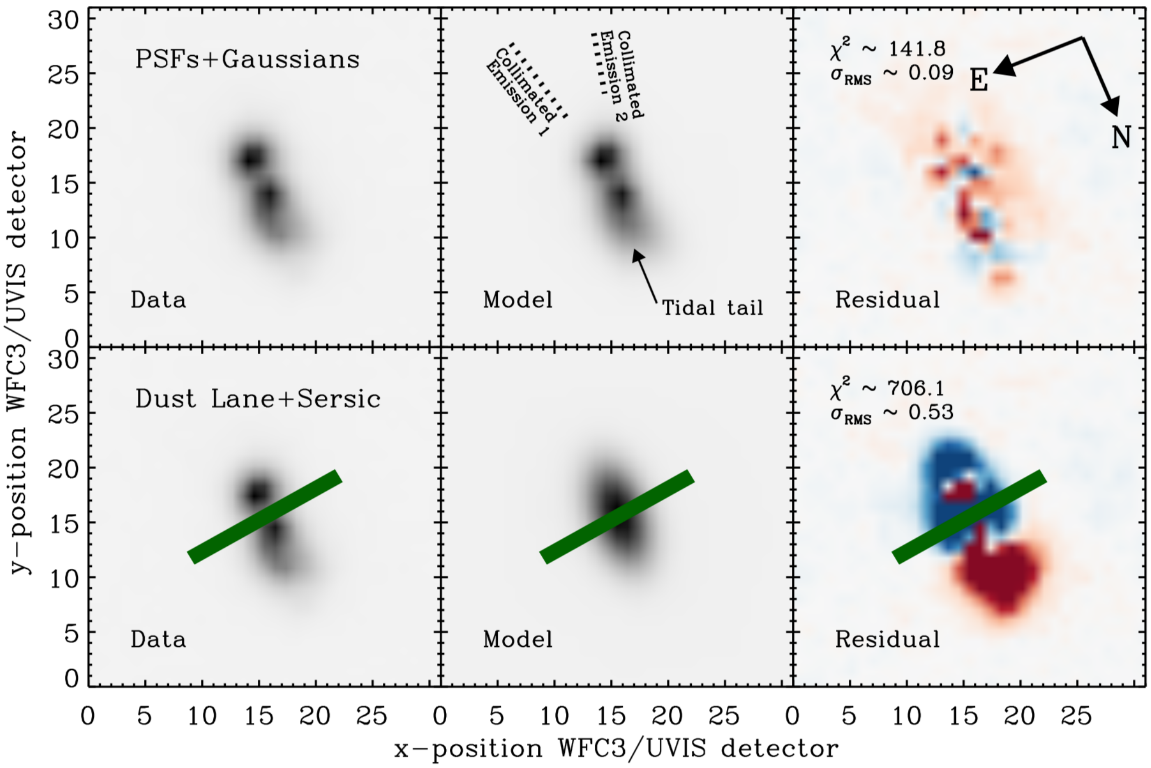

Figure 3.2: Morphological analysis of emission in the central 1″x1″ region of J1010+1413 using the GALFIT software package. Upper: our preferred 4-parameter model (two PSFs and two extended Gaussians). The residual image (data – model) consists of only unstructured Poisson noise with no distinct features. Lower: Sersic profile with a (presumed) dust lane (represented by a mask; green line) splitting the observed emission in two. The residuals show significant structure with a high RMS noise.

Indeed, we find evidence for two collimated emission features oriented at ∼11 and 342 degrees from North, consistent with the presence of two distinct accretion disks (Figure 3.2).

3.1.2 Chandra ACIS-S observations

J1010+1413 was observed on January 20, 2016 with the Advanced CCD Imaging Spectrometer (ACIS) on board the NASA Chandra X-ray Observatory (Proposal:17700576; PI:Pardo). The data were reduced following standard procedures using the Chandra Interactive Analysis of Observations (CIAO) software package provided by the Chandra X-ray Center. After standard grade filtering, the total exposure in good time intervals was ∼24.1 ks. The native spatial resolution of ACIS-S (0.492″/pixel) is insufficient to resolve two distinct point sources separated by only 0.13″, even when using more sophisticated sub-resolution techniques, and hence, the quasars should appear as a single X-ray point source. The soft-band image (0.5–3.5 keV) is characterized by marginally extended ($r \sim 1.9''$) diffuse emission with 59±8 counts. A spectral analysis of the X-ray emission (extracted from a 2″ aperture and grouped to 1 photon/bin using `grppha`) involving a simple absorbed power law combined with a Galactic foreground absorber ($N_{\rm H} = 3.4 \times 10^{20}{\rm cm}^{-2}$) produces a best-fit $\Gamma \sim 2.8 \pm 0.3$ and $N_{\rm H} < 10^19{\rm cm}^{-2}$, which is inconsistent with X-ray emission arising directly from an AGN. An APEC plasma model is also found to be a reasonable description of the data with $kT \sim 3.1 \pm 0.6$, although the soft power law model is marginally preferred ($\Delta C_{\rm stat}$ ∼2.2). The best-fit X-ray flux is only $f_{\rm X,0.5-7keV} \sim 2.0 \pm 0.5 \times 10^{-14}{\rm erg\ s^{-1}\ cm^{-2}}$, i.e., a low luminosity of $L_{0.5-7\rm keV} \sim 1.5 \times 10^{42}{\rm erg\ s^{-1}}$, and is a factor $\gtrsim$ 650 below the naive expectation based upon the $L_{6\mu\rm m}$–$L_{\rm X}$ relation (Chen et al., 2017). Such a deficit in the observed X-ray emission compared with other mid-IR/optical $L_{\rm AGN}$ indicators (Alexander et al., 2008; Goulding et al., 2011) suggests obscuration by heavily Compton-thick ($N_{\rm H} \sim 10^{25}\ {\rm cm}^{-2}$) gas. The additional inclusion of a second absorbed power law to assess the presence of a heavily obscured Compton-thick quasar was left unconstrained due to the small number of photons.

Given its low luminosity, spectral shape, and the fact that it is resolved, the soft X-ray emission most likely arises from star formation or quasar-produced *scattered* light, similar to the well-studied quasar SDSSJ1356+1026 (Greene et al., 2014). However, the observed Hα emission ($L_{H\alpha} \sim 1.3 \times 10^{42}{\rm erg\ s^{-1}}$) allows us to place a conservative upper limit (i.e., assuming no AGN contribution to Hα) on the star-formation rate (SFR) of $\lesssim 10 M_\odot$/yr. When coupled with the total stellar mass and the relation of Lehmer et al. (2010), we can place an upper limit on the X-ray emission from star formation of $L_X \lesssim 3 \times 10^{40}$erg s^{-1}. Hence, the slightly higher observed X-ray luminosity is more suggestive of a scattered light origin.

3.2 Morphological Evidence for a Pair of Accreting SMBHs

Due to the presence of two distinct nuclear stellar cores with cospatial [OIII] emission radiating at quasar-like luminosities, our preferred interpretation is that J1010+1413 contains two rapidly accreting SMBHs close to its photometric center. Such a scenario is consistent with the very late-stage merging galaxy found from previous SDSS and Gemini-IFU data. However, even though both the F689M continuum and [OIII] images strongly suggest two distinct, spatially-separated point sources, complicated structures and morphologies in the NLRs can make the identification of SMBH pairs ambiguous (Shen et al., 2011a).

To better elucidate the nature of the nuclear region in J1010+1413, we performed an imaging decomposition in the F689M and [OIII] images using the GALFIT package (Peng et al., 2010). The GALFIT analysis requires an accurate representation of the WFC3/UVIS point spread function (PSF) to convolve with the model components. We constructed the PSF using a hybrid methodology (Grogin et al., 2011), which combines a model of the instrument PSF (produced by the STScI software package TinyTim) with real point-like stellar objects detected in the observation. We confirmed that our PSF model produces an accurate subtraction of a point source in the WFC3 images, with no clear systematic residuals beyond the image noise.

The [OIII] emission is not well fit using only two PSF functions; rather it requires the inclusion of two extended Gaussians, centered close to each of the point sources. Conversely, a fit using only two Gaussians produces a significantly lower quality fit ($\Delta\chi^2 = (\chi^2_{\rm 4comp} - \chi^2_{\rm 2comp}) \sim -189$) leaving residual point sources in the image, and hence, two PSF functions are also required. The best-fit solution from the 4-component model is shown in Figure 3.2 (upper panel), producing an excellent fit to the data; the residual is consistent with Poisson noise. Each Gaussian component is a factor ∼2-3 brighter than its associated PSF component; this is to be expected as NLRs are typically observed on scales of several hundred parsecs in local galaxies and should therefore require a bright component extended beyond the PSF. Furthermore, one of the Gaussian components is marginally offset $\sim 0.1''$ north of the northern nucleus, and is consistent with the termination of a stream of stellar material, presumably the result of the on-going merging of the two cores. This component is observed in both the F689M and [OIII] images, while a continuation of this stream is clearly visible to the west of the core in the F689M image shown in Figure 3.1.

A potential alternative scenario for the observed features could be a single SMBH residing at the center of a large extended stellar bulge and NLR, split along the minor axis by a dust lane. This dust lane would fully obscure the would-be point source emission arising from a single quasar. If the gas is uniformly distributed, the [OIII] emission arising from a single SMBH would appear as an elongated component above and below the dust lane. To test this, we attempted to model both the continuum and [OIII] images using a single Sersic component with the centroid constrained to the region hidden by an artificial dust lane (represented by a GALFIT mask region; Figure 3.2 lower panels). The resultant Sersic component has an extremely flat profile ($n \sim 0.4$), similar to that of a Gaussian. However, in comparison to our best-fit model, the Sersic+dust-lane model is an extremely poor fit $\Delta\chi^2 = (\chi^2_{\rm Best} - \chi^2_{\rm DL+Sersic}) \sim -564.3$; the residual RMS noise is a factor $\gtrsim 5$ larger than our best-fit model, and the two previously determined point sources are strongly under-subtracted in the residual image. Hence, the HST data do not support a scenario involving a single SMBH hidden by a dust lane.

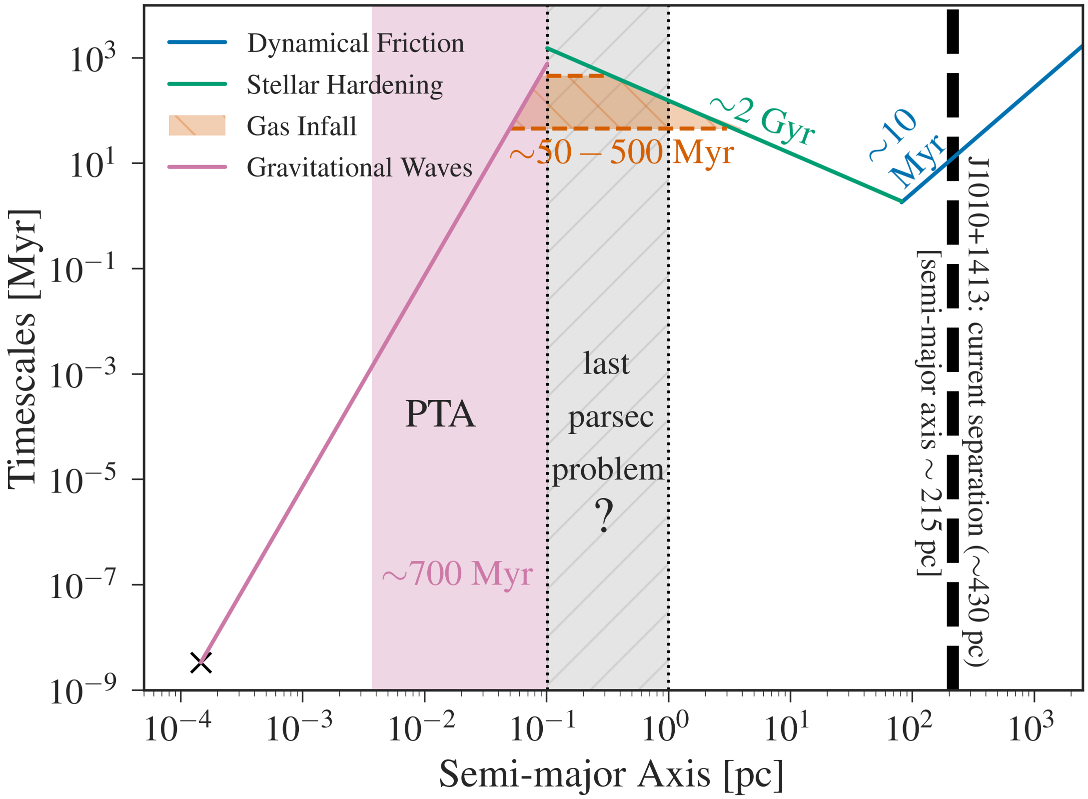

Figure 3.3: Dynamical timescales for J1010+1413 as a function of binary semi-major axis (assuming a circular orbit). Dynamical friction, stellar hardening, and GW emission phases are shown with blue, green, and pink lines, respectively. Current pair semi-major axis is shown with the black, dashed line. The PTA band for an object of J1010+1413's chirp mass is indicated by the pink region.

We further tested whether the very luminous [OIII] emission could be produced by shock heating from powerful starburst-driven winds, ignited as a result of the galaxy merger. Given either the [OIII] or 22μm luminosities, such a scenario would require SFR$\gg 10^3 M_\odot$/yr in the central 500 pc region. However, this is inconsistent with the non-detection of J1010+1413 at 100μm in IRAS, and is orders of magnitude higher than the upper limit of $\lesssim$10$M_\odot$/yr set by Hα. We thus conclude that the [OIII] and IR emission must arise from quasar activity.

Our GALFIT simulations confirm the presence of two continuum and [OIII]-emitting cores in the nuclear region of J1010+1413. The southern nuclear region is

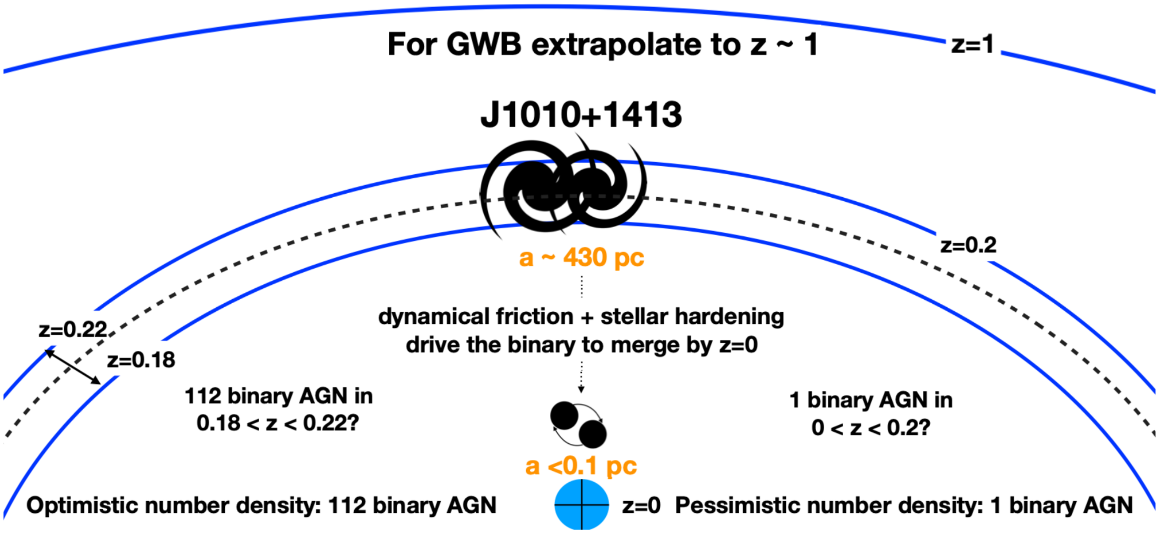

Figure 3.4: Schematic of GWB amplitude assumptions given the SMBH pair in J1010+1413. Dynamical friction and stellar hardening will drive SMBH pairs like J1010+1413 to merge by $z = 0$ (Fig.3), implying that there is at least one local SMBH binary emitting GWs. The expectation of this one GW source is used to estimate $n_{\rm binary}(z = 0)$, which is extrapolated to $z = 1$ to compute a pessimistic GWB amplitude estimate, $A \sim 1.8 \times 10^{-17}$. Alternately, a more optimistic $n_{\rm binary}(z = 0)$ can be estimated based on the population of known luminous quasars similar to J1010+1413 within $0.18 \leq z \leq 0.22$, producing $A \sim 3 \times 10^{-16}$.

marginally more luminous in [OIII] than the northern nucleus with $\Delta m_{\rm [OIII]} \sim 0.14$, i.e., a flux ratio of 1:1.3. Using the previously measured Balmer decrement (Mullaney et al., 2013) and an extinction-corrected bolometric correction (Kauffmann & Heckman, 2009), we measure intrinsic quasar luminosities of $L_{\rm AGN,N} \sim 4.2 \times 10^{46}$ and $L_{\rm AGN,S} \sim 5.4 \times 10^{46}$ erg s^{-1} for the north and south nucleus, respectively. The combined luminosities are consistent with $L_{\rm bol}$ determined in the mid-IR. Under the presumption that both quasars are accreting at $L/L_{\rm Edd} = 1$, we are able to place a *minimum* mass of $4 \times 10^8 M_\odot$ for each SMBH in the pair.

We conclude that when all lines of evidence are taken together – (1) the measured mid-IR and [OIII] luminosity; (2) the morphology of the [OIII] emission; and (3) the spatial coincidence of the stellar-continuum and [OIII] point sources – J1010+1413, in all likelihood, harbors two roughly equal-mass $M_{\rm BH} \gtrsim 4 \times 10^8 M_\odot$ SMBHs separated in projection by ∼430pc. Further evidence for a pair of SMBHs in J1010+1413

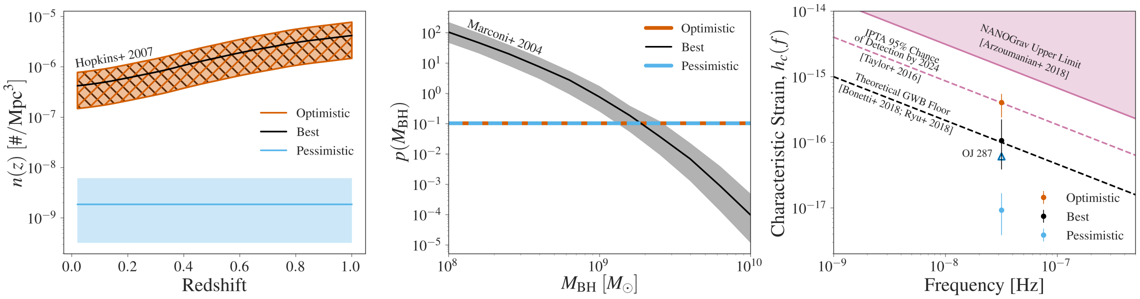

Figure 3.5: *Left:* Number density $n(z)$ of AGN binaries pessimistically assuming J1010+1413 is the only binary AGN in SDSS to $z < 0.2$ and constant number density (blue) or assuming an evolving $n(z)$ normalized to the number of J1010+1413-like systems at $z \sim 0.18$–0.22 in SDSS for our most optimistic (orange) and best-case (black) scenarios, which themselves differ by the assumed SMBH mass function (center panel). Shaded regions provide estimated uncertainties. *Center:* Assumed SMBH mass functions for binary AGN. *Right:* Estimated characteristic strain (h_c) of the GWB following our well-motivated $n(z)$ and $n(M_{\rm BH})$ assumptions. For reference, we provide h_c (95% lower limit) assuming the blazar OJ287 is a true SMBH binary (Zhu et al., 2019; Dey et al., 2019).

must await on-going follow-up with JVLA, HST, and ground-based adaptive optics telescopes.

3.3 Relevance to Gravitational Waves

J1010+1413 is not currently emitting GWs in the PTA band. However, as we describe below, the predicted time to the PTA band for J1010+1413 is less than the lookback time to the object (Figure 3.3). Thus, we expect a population of objects like J1010+1413 that would be emitting GWs in the PTA band *today* (Figure 3.4). Using well-motivated assumptions on their number density ($n_{\rm binary}$), we can place limits on the GWB (Fig. 3.5).

3.3.1 Coalescence predictions

The evolution of SMBH pairs is expected to proceed through three main stages leading to coalescence: (1) dynamical friction, (2) stellar hardening, and (3) GW emission

(Begelman et al., 1980). The SMBH pair in J1010+1413, currently separated by 430 pc, should be nearing the end of its dynamical friction phase (Figure 3.3). This phase has a timescale given by (Binney & Tremaine, 2008):

$$t_{\rm dyn} = \frac{19\ {\rm Gyr}}{\ln \Lambda} \left(\frac{a}{5\ {\rm kpc}} \right)^2 \frac{\sigma}{200\ {\rm km/s}} \frac{10^8\ M_\odot}{M_2}\ , \tag{3.1}$$

where a is the semi-major axis of the binary, σ is the velocity dispersion of the stars, and M_2 is the mass of the lighter SMBH. We use the virial theorem with our measured values for the M_* and $r_{\rm gal}$ to estimate the stellar velocity dispersion. We expect the SMBH pair will enter the stellar hardening phase within ∼10 Myr, at which time the SMBH pair's angular momentum will be transferred to slower-moving stars that pass close to the pair, decreasing the orbital separation. This stellar hardening happens on a timescale given by (Sesana & Khan, 2015):

$$t_{\rm sh} = \frac{\sigma_{\rm inf}}{G H \rho_{\rm inf} a_{\star/{\rm gw}}}\ , \tag{3.2}$$

where $\sigma_{\rm inf}$ is σ at the BH influence radius, $\rho_{\rm inf}$ is the mass density at this radius, $H = 15$ is a dimensionless hardening rate constant (see Quinlan, 1996, for more details), and $a_{\star/{\rm gw}}$ is the semi-major axis at which GW emission begins to dominate the decay of the orbit. We follow the usual procedure of assuming a Dehnen profile with $\gamma = 1$ for the stars (Dehnen, 1993; Sesana & Khan, 2015; Mingarelli et al., 2017). However, there may be insufficient stars to eject for the pair to reach the sub-pc scale, and merge via GW emission (Yu & Tremaine, 2003). In this 'final parsec problem' scenario, the time to coalescence becomes significantly longer than a Hubble time, causing the pair to stall. Without taking this effect into account, the expected hard binary timescale is ~ 2 Gyr. Large quantities of gas surrounding the SMBH pair will decrease the binary's time to coalescence. For approximately equal-mass systems, the timescale for migration is about equal to the accretion timescale (Gould & Rix, 2000).

Assuming the SMBH pair in J1010+1413 continues to accrete at $\lambda_{\rm Edd} = 0.1$–1.0, the gas accretion phase will require (Begelman et al., 1980):

$$t_{\rm gas} \sim \frac{M_1}{M_\odot} \left(\frac{\dot{M}}{1\ M_\odot/{\rm yr}} \right)^{-1} \ {\rm yr}\ , \tag{3.3}$$

where $\dot{M}$ is the accretion rate, i.e., a gas accretion timescale of $t_{\rm gas} \sim 100$ Myr. Thus, we expect the SMBH pair to reach sub-parsec separations within $0.1 - 2$ Gyr. Once $r_{\rm sep} \lesssim 0.1$ pc, GW emission will lead to final coalescence within ∼700 Myr. If merging SMBH binaries do not stall, by the present day we expect J1010+1413-like systems at $z \sim 0.2$ to be emitting GWs, anchoring the number of possible GW-emitting SMBH binaries since $z \sim 0.2$.

3.3.2 Contribution to the GWB

A GWB produced by the incoherent superposition of GWs from all inspiralling SMBH binaries over cosmic history is expected to be observed by PTAs in the next few years (Taylor et al., 2016; Kelley et al., 2017). SMBH pairs at $z < 1$ and in the $10^8 - 10^9 M_\odot$ range, i.e., systems similar to J1010+1413, are expected to be the primary source population of this signal. The GWB amplitude depends strongly on the SMBH mass function, SMBH occupation fraction, and galaxy-galaxy merger rates, while the shape of the characteristic strain (h_c) spectrum holds clues to the final parsec problem (Sampson et al., 2015; Arzoumanian et al., 2016). See Mingarelli (2019) for a brief review and Burke-Spolaor et al. (2019) for a comprehensive one.

Here we use the existence of the SMBH pair in J1010+1413 to put limits on the space density of similar objects.

As a lower limit, we assume that J1010+1413 is the only $> 10^8 M_\odot$ SMBH binary detectable in the SDSS to $z = 0.2$. This would imply that an analogous system would be merging today i.e., $n_{\rm binary}(z = 0) = 1 \times 10^{-9}$ Mpc^{-3}, Figure 3.4. Assuming $n_{\rm binary}$

is *constant* with both $M_{\rm BH}$ and z, we estimate there are $\sim$ 300 binary AGN that contribute to the GWB to $z < 1$.

Our most optimistic scenario assumes that J1010+1413 is representative of luminous Type-2 quasars ($L_{\rm bol} \gtrsim 10^{46}$ erg s^{-1}) in merging systems that are detectable by SDSS, WISE and the NRAO VLA Sky Survey at $z \sim 0.18$–0.22. By selecting all Type-2 AGN from Mullaney et al. (2013) at $z \sim 0.18$–0.22, and assuming $L/L_{\rm Edd} = 0.3$ (typical of SDSS quasars; Shen et al. 2011b) and the $z = 0.2$ observed fraction of AGN in merging systems ($f_{\rm merge} = 0.25$; Hickox et al. 2014), we predict there are potentially 112 binary AGN with $M_{\rm BH} > 10^8 M_\odot$ in SDSS, i.e., $n_{\rm binary}(z = 0) = 2 \times 10^{-7}$ Mpc^{-3}. Uncertainties are estimated using a range of Eddington ratios ($L/L_{\rm Edd} = 0.1 - 1.0$). We predict the evolution of $n_{\rm binary}$ to $z = 1$ by normalizing the quasar number density of Hopkins et al. (2007) to $n_{\rm binary}(z = 0)$, providing a total of $\sim 1.2 \times 10^6$ binary AGN to $z < 1$.

Our more realistic ("best") scenario also accounts for the dependence of $n_{\rm binary}$ on $M_{\rm BH}$. We expect SMBHs in binaries to follow an $M_{\rm BH}$ function (Marconi et al., 2004), which corrects for the smaller number of very massive ($M_{\rm BH} > 10^{10}$ $M_\odot$) SMBHs in the Universe. Our limits do not differ greatly if we instead adopt the observed quasar luminosity function and a fixed Eddington ratio. Allowing the number density to vary with $M_{\rm BH}$ and z gives the same total number of binary AGN, but distributes their $M_{\rm BH}$ differently. We do not expect the SMBH mass function to vary significantly to $z < 1$ in the range $M_{\rm BH} = 10^8 - 10^{10} M_\odot$ (Merloni & Heinz, 2008).

We use our three scenarios to compute the GWB h_c using the Phinney (2001) formalism:

$$h_c^2(f) = \frac{4G^{5/3}}{3\pi^{1/3}c^2}\frac{1}{f^{4/3}}\int n(z, \mathcal{M})\frac{(\mathcal{M})^{5/3}}{(1+z)^{1/3}}\, dz\, d\mathcal{M}\ , \tag{3.4}$$

where $\mathcal{M} = (1/(1+q)^2)^{3/5} M_1$ is the chirp mass of the binary, q is the binary mass ratio, and M_1 is the primary mass. We integrate over $z = 0 - 1$ and $\mathcal{M} = 10^{7.6} - 10^{9.6}$ $M_\odot$, where this mass range corresponds to $M_{\rm BH} = 10^8 - 10^{10}\ M_\odot$ and $q = 1$. We note that computing the integral to $z = 2$ increases our final h_c estimate by a factor $\lesssim$2.

We predict a range of limits on $h_c(f = 1\ {\rm yr}^{-1})$ from 9.2×10^{-18} to 4.0×10^{-16}, with a best estimate of $h_c(f = 1\ {\rm yr}^{-1}) = 1.1 \times 10^{-16}$. This is $\sim$$1 - 10\%$ of the most recent upper limit on the GWB, $h_c(f = 1\ {\rm yr}^{-1}) < 1.45 \times 10^{-15}$ (Arzoumanian et al., 2018), and well within the reach of PTAs in the next decade (Taylor et al., 2016).

Our predicted range for h_c brackets the theoretical lower limit of $\sim$$10^{-16}$, which would be produced by SMBH binaries stalled at the last parsec, assuming conservative $M_{\rm BH}$ estimates (Sesana et al., 2016; Shankar et al., 2016). These stalled SMBHs ultimately merge via many body interactions with SMBHs introduced by additional galaxy mergers (Bonetti et al., 2018; Ryu et al., 2018). There are therefore two intriguing implications for the GWB following our discovery of J1010+1413: (1) if the true GWB amplitude is marginally below the current sensitivity limits, then SMBH pairs similar to that of J1010+1413 contribute $1 - 10\%$ of the GWB signal, and thus there must be little stalling of the SMBH pairs in nature; or (2) if the GWB amplitude is lower than our predicted limits, then we would have evidence that $M_{\rm BH}$ have been overestimated and/or that nature does not have a solution to the final parsec problem. In concert with future simulations and/or the improving GWB upper-bound, the SMBH pair in J1010+1413 will anchor source population estimates, merger rates, and even the volume of the GWB.

The identification of the SMBH pair in J1010+1413 has yielded new empirical insight into the nature of the nanohertz GWB. Our investigation has highlighted the benefit of combining quasar detections made in the mid-IR with high-resolution optical imaging to confirm the presence of a SMBH pair. However, our current estimates for h_c are limited by our ability to (1) accurately measure the number of J1010+1413-like systems in the redshift slice $z \sim 0.18 - 0.22$, and (2) constrain the evolution of such merging systems out to $z < 1$ where the GWB signal may peak.

The combination of sensitive large-scale surveys that are optimized for AGN detection and/or galaxy morphologies (e.g., SphereX; WFIRST) will allow the future discovery and characterization of a population of small-separation SMBH pairs, similar to J1010+1413.

Chapter 4

Galaxy Disk Warps & Self-Interacting Dark Matter

All particles in the Standard Model have non-gravitational interactions, which makes it reasonable to consider self-interactions in the dark sector as well. In addition, self-interacting dark matter (SIDM) could alleviate the possible small-scale CDM issues by redistributing dark matter out of the centers of halos and suppressing small-scale structure formation (Spergel & Steinhardt, 2000). For velocity-independent interactions, SIDM cross sections per unit DM mass of $\sigma/m \sim 0.1-1$ cm^2/g would be needed to fit the current observations (Rocha et al., 2013). However, there are constraints on SIDM from a wide variety of systems and experiments (for a comprehensive review, see Tulin & Yu, 2018). For example, SIDM would lead to the evaporation of halos due to high-momentum-transfer collisions. Thus, the existence of DM halos in dwarf galaxies places constraints on the cross section (Gnedin & Ostriker, 2001; Kahlhoefer et al., 2014). SIDM would also allow for the spherical relaxation of cluster halos. The observation of elliptical cluster halos places strong limits on the SIDM cross section from cluster ellipticites (Miralda-Escudé, 2002), although these are disputed (Peter et al., 2013).

SIDM also modifies the distribution of DM in galaxy and galaxy cluster collisions. In the canonical CDM picture, the DM halos do not interact but pass through one another without collision, while the gas shock-heats and decelerates. If DM has self-interactions, then we would expect the DM to experience a drag as well, with a magnitude depending on the interaction cross section. Thus, the centroid of the DM compared to that of the gas could be used to constrain the SIDM cross section. This method has been employed successfully for galaxy cluster collisions: most famously for the Bullet Cluster, which disfavors interaction cross sections $\sigma/m > 0.7 - 1$ cm^2/g (Markevitch et al., 2004; Randall et al., 2008), although some simulations contend that these constraints may be overstated (Robertson et al., 2017).

We can also expect this effect to leave imprints in the subhalos of clusters – from galaxies falling into clusters. Specifically, we can look for the separation between the centroid of the stars and the DM. The centroid separation technique has been successfully used in simulations (Massey et al., 2011). Unfortunately, a clear detection of this effect in data is challenging due to the weak-lensing accuracy required, as well as other systematics (Harvey et al., 2013). However, recent work has shown that the infall of galaxies into clusters can leave signatures at larger scales (Banerjee et al., 2019).

Instead, we can try to look for other markers of this centroid separation. Secco et al. (2018) recently considered the SIDM dynamics of a disk galaxy falling into a large galaxy cluster. Using numerical simulations, they found that the separation between the DM and stellar centroids should also produce a warp in the stellar disk of the galaxy. This would be a U-shaped warp facing in the direction of motion – a signature difficult to mimic with baryonic effects. The largest warps should occur in galaxies on first infall into galaxy clusters. The dark matter densities are highest in galaxy clusters and the first infall allows for ample time to form the warp before the direction of the drag force changes at periapsis. However, warps are most easily measured in disk galaxies, which are typically not found in galaxy clusters. Although at lower magnitude, this warping should in fact occur in *any* galaxy moving in a dark matter medium. There have been no observational searches for this signal in data thus far.

In this chapter, we place constraints on the SIDM cross section by measuring the warps of stellar disks. Section 4.1 presents the different types of interaction and physical effects that we consider. Section 4.2 describes our methods, including our forward-modelling of SIDM warps and measurements of real warps. Section 4.3 gives our results, while Section 4.4 discusses these results and concludes.

4.1 Theory

DM self-interactions will generally induce a drag force on the DM halo of a galaxy traveling through some background over-dense region. The form of the drag force will depend on the type of self-interaction. For a contact (velocity-independent) interaction, we expect a fluid-type drag force[1] $\propto \rho_{\mathrm{bg}} v^2$, where ρ_{bg} is the density of the background dark matter and v is the relative velocity between the halo and the background. For a long-range interaction (velocity and angle-dependent), we expect a drag force $\propto \rho_{\mathrm{bg}}/v^2$ (e.g., Kahlhoefer et al., 2014). For intermediate-range interactions (i.e. where the mass of the mediator is close to the mass of the DM particle), we expect a force law between the contact and long-range cases.

Other physics will also affect the final force law. For any one collision between particles, there is a probability of the halo particle being ejected. Over time, this leads to an evaporation of the halo, which will damp the drag force. Finally, we expect some velocity dispersion in both the halo and the background. This will cause a distribution of incoming particle velocity directions, further damping the drag force.

---

[1] This assumes the interaction times are small enough for the fluid approximation to hold. We discuss this further in Section 4.4.

In this section, we develop the equations for the expected stellar warp produced by self-interactions between the DM in a galactic halo and a background overdensity. We begin by finding the drag force per particle mass for the three different types of DM self-interactions (contact, long-range, and intermediate-range), along with the modifications due to evaporation and velocity dispersion of the halo. We then describe the warp this produces within the galaxy's stellar disk.

4.1.1 Halo deceleration from DM self-interactions

Consider a halo moving through some background medium with relative velocity $\vec{v}$. We would like to find the force per unit mass on the halo in the direction of $\vec{v}$ from DM self-interactions between particles in the halo and particles in the medium. This drag force law will depend on several factors, such as the angular and velocity dependencies of the self-interaction and the effects of evaporation and velocity dispersion.

Contact interactions

Let us first consider velocity-independent interactions arising from a contact force. For now, focus on a two-particle interaction: one particle from the halo and one from the background overdensity. In the center of mass (COM) frame, the velocity of the halo particle in the direction of the relative velocity will change by:

$$\delta v_{||} = |\vec{v}|(\cos\theta - 1) \ , \tag{4.1}$$

where θ is the scattering angle in the COM frame. Note that $\delta v_{||}/|\vec{v}| \leq 0$ always.

The total number of interactions is given by:

$$dN = \frac{\rho_{\rm bg}}{m_{\rm DM}} \frac{d\sigma}{d\Omega} |\vec{v}| \ dt \ d\Omega \ , \tag{4.2}$$

where $\rho_{\rm bg}$ is the density of the background overdensity and $d\sigma/d\Omega$ is the differential cross section.

The total drag acceleration is given by integrating over all interactions, which can be written as:

$$\vec{a}_{\rm drag} = \frac{\vec{F}_{\rm drag}}{m_{\rm DM}} = \frac{\rho_{\rm bg}}{m_{\rm DM}} |\vec{v}|^2 \int \frac{d\sigma}{d\Omega} (\cos\theta - 1) \; d\Omega \; \hat{v} \tag{4.3}$$

As Secco et al. (2018) show, for an isotropic interaction, this leads to a drag acceleration of the form:

$$\vec{a}_{\rm drag} = -\frac{1}{4} \left(\frac{\tilde{\sigma}}{m_{\rm DM}} \right) \rho_{\rm bg} \vec{v}^2 \; , \tag{4.4}$$

where $\tilde{\sigma} = \int d\sigma/d\Omega \; d\Omega$ is the total cross section. Since we are assuming an isotropic cross section here, $\tilde{\sigma}$ is just a constant.

However, this does not take into account the effects of evaporation on the halo. If we allow for evaporation, the drag acceleration is given by (Markevitch et al., 2004; Kummer et al., 2018):

$$\vec{a}_{\rm drag} = -\frac{\chi_{\rm d}}{4} \left(\frac{\tilde{\sigma}}{m_{\rm DM}} \right) \rho_{\rm bg} \vec{v}^2 \; , \tag{4.5}$$

where $\chi_{\rm d}$ is the fraction of events that lead to deceleration rather than evaporation. Markevitch et al. (2004) find this fraction by considering the momentum change per collision and comparing this to the escape velocity of the halo. This gives:

$$\chi_{\rm d} = 1 - 4 \int_{\sqrt{x^2/(1+x^2)}}^{1} dy \; y^2 \sqrt{y^2 - x^2(1-y^2)} \; , \tag{4.6}$$

where $x \equiv |\vec{v}_{\rm esc}|/|\vec{v}|$ and $v_{\rm esc}$ is the escape velocity for the halo. If we assume a virialized halo, then $v_{\rm esc} = 2v_{\rm disp}$, where $v_{\rm disp}$ is the velocity dispersion of the halo.

Both of these cases assume that all of the particles in the halo are traveling with velocity $\vec{v}$. More realistically, the particles in the halo will have some velocity dispersion. Kummer et al. (2018) find that, for a Maxwellian velocity distribution, this leads to a suppression of the drag force, which is well approximated by:

$$\chi_{\mathrm{p}} = \frac{|\vec{v}|^3}{|\vec{v}|^3 + |\vec{v}_{\mathrm{disp}}|^3} \tag{4.7}$$

where v_{disp} is again the velocity dispersion of the particles. The background should also have a velocity dispersion, but we ignore this for the purposes of this paper since it will be small compared to the dispersion of the halo.

Our final equation for the contact drag acceleration is then:

$$\vec{a}_{\mathrm{drag}}^{\,\mathrm{contact}} = -\frac{1}{4}\chi_{\mathrm{d}}\chi_{\mathrm{p}}\left(\frac{\tilde{\sigma}_{\mathrm{DM}}}{m_{\mathrm{DM}}}\right)\rho_{\mathrm{bg}}\vec{v}^2 \ . \tag{4.8}$$

Long-range interactions

Long-range interactions describe DM that interacts via a massless mediator. This introduces angle and velocity dependencies in the cross section, which can be written as (Kummer et al., 2018; Tulin & Yu, 2018):

$$\frac{d\sigma}{d\Omega} = \frac{\sigma_0 \sin\theta}{\left(\frac{v}{c}\right)^4 \sin^4\left(\frac{\theta}{2}\right)} \ , \tag{4.9}$$

where σ_0 describes the coupling strength of the interaction. This is the well-known Rutherford scattering formula.

To find the drag force, we now proceed similarly as in Sec. 4.1.1. Using Equation 4.3, we find that the drag acceleration given by long-range interactions is:

$$\vec{a}_{\mathrm{drag}}^{\,\mathrm{long}} = -\frac{1}{4}\left(\frac{\tilde{\sigma}}{m_{\mathrm{DM}}}\right)\rho_{\mathrm{bg}}\frac{c^4}{|\vec{v}|^2}\ \hat{v} \ , \tag{4.10}$$

where we define an effective cross section $\tilde{\sigma} \equiv -32\pi(2+\pi)\sigma_0$ (see Kahlhoefer et al., 2014, for a similar approach).

Unlike the drag force from contact interactions, the drag force from long-range interactions is maximized for *small* relative velocities. The lack of high-momentum-transfer collisions (for suitably small $\tilde{\sigma}/m_{\rm DM}$) means that evaporation is negligible in this case (see, for example, Kummer et al., 2018). The velocity dispersion correction does not depend on cross section, and so is the same as for the contact case. This gives a full long-range interaction drag acceleration of:

$$\vec{a}_{\rm drag}^{\rm \ long} = -\frac{1}{4}\chi_p \left(\frac{\tilde{\sigma}}{m_{\rm DM}}\right) \rho_{\rm bg} \frac{c^4}{|\vec{v}|^2}\ \hat{v}\ . \tag{4.11}$$

Intermediate-range interactions

As our final case, we consider intermediate-range interactions, where the mediator mass can range from massless to infinitely massive (i.e. the contact limit). We do this by interpolating the drag acceleration between the two previous cases:

$$\vec{a}_{\rm drag}^{\rm \ inter} = -\frac{1}{4}\left(\frac{\tilde{\sigma}_{\rm DM}}{m_{\rm DM}}\right) \rho_{\rm bg} \vec{v}^2 \left(\frac{c}{|\vec{v}|}\right)^m\ \hat{v}\ , \tag{4.12}$$

where $0 \leq m \leq 4$. When $m = 0$, this exactly equals the contact case; when $m = 4$, this exactly equals the long-range case. We do not assume a particular differential cross section equation; however, we presume that any actual differential cross section would map onto this form for the drag force. For example, a common cross section for this type of interaction is (e.g., Kummer et al., 2018):

$$\frac{d\sigma}{d\Omega} = \frac{\sigma_0 \sin\theta}{2\left(1 + \frac{(v/c)^2}{w^2}\sin^2\frac{\theta}{2}\right)^2}\ , \tag{4.13}$$

where $w = m_\phi/m_\chi$, ϕ is the mediator, χ is the DM particle, $\sigma_0 = (4\pi\alpha^2 m_\chi^2)/m_\phi^4$, and α is the coupling constant. We find that this gives similar results to our interpolating case (see Section 5.3).

As with the previous cases, we would like to include the effects of both velocity dispersion and evaporation. The velocity dispersion does not depend on the cross section, so this is trivial to add. However, the evaporation effect requires some more thought. The evaporation fraction calculation requires knowing the differential cross section equation (Markevitch et al., 2004; Kummer et al., 2018). We circumvent this by noting that the evaporation rate should be bracketed by the contact and long-range cases, which means it must be a rapidly decreasing function of the variable m that governs the range of the interaction. We adopt:

$$\chi_d^{\text{inter}} = 1 - (1 - \chi_d)\exp[-2m]\ . \tag{4.14}$$

When $m = 0$, $\chi_d^{\text{inter}} = \chi_d$; however, when $m = 4$, $\chi_d^{\text{inter}} \sim 1$ and there is no evaporation. Unless there is some extra physics leads to interesting behavior, the evaporation fraction should smoothly interpolate between the two cases and this function should approximately capture its effect.

Then our final equation for this interaction, including all physics, is:

$$\vec{a}_{\text{drag}}^{\ \text{inter}} = -\frac{1}{4}\chi_d^{\text{inter}}\chi_p\left(\frac{\tilde{\sigma}}{m_{\text{DM}}}\right)\rho_{\text{bg}}\vec{v}^2\left(\frac{c}{|\vec{v}|}\right)^m\ . \tag{4.15}$$

4.1.2 Galaxy warping in SIDM

We now know the force on the galaxy halo from these self-interactions. However, we cannot measure the force directly – we must instead examine its effect on the morphology of the galaxy. In particular, the displacement between the halo and disk induced by dark matter self-interactions sets up a potential gradient across the disk, which warps it into a U-shape. We calculate this warp by considering the difference in acceleration between the disk's center and a general point along the disk, following the methods of Desmond et al. (2018a).

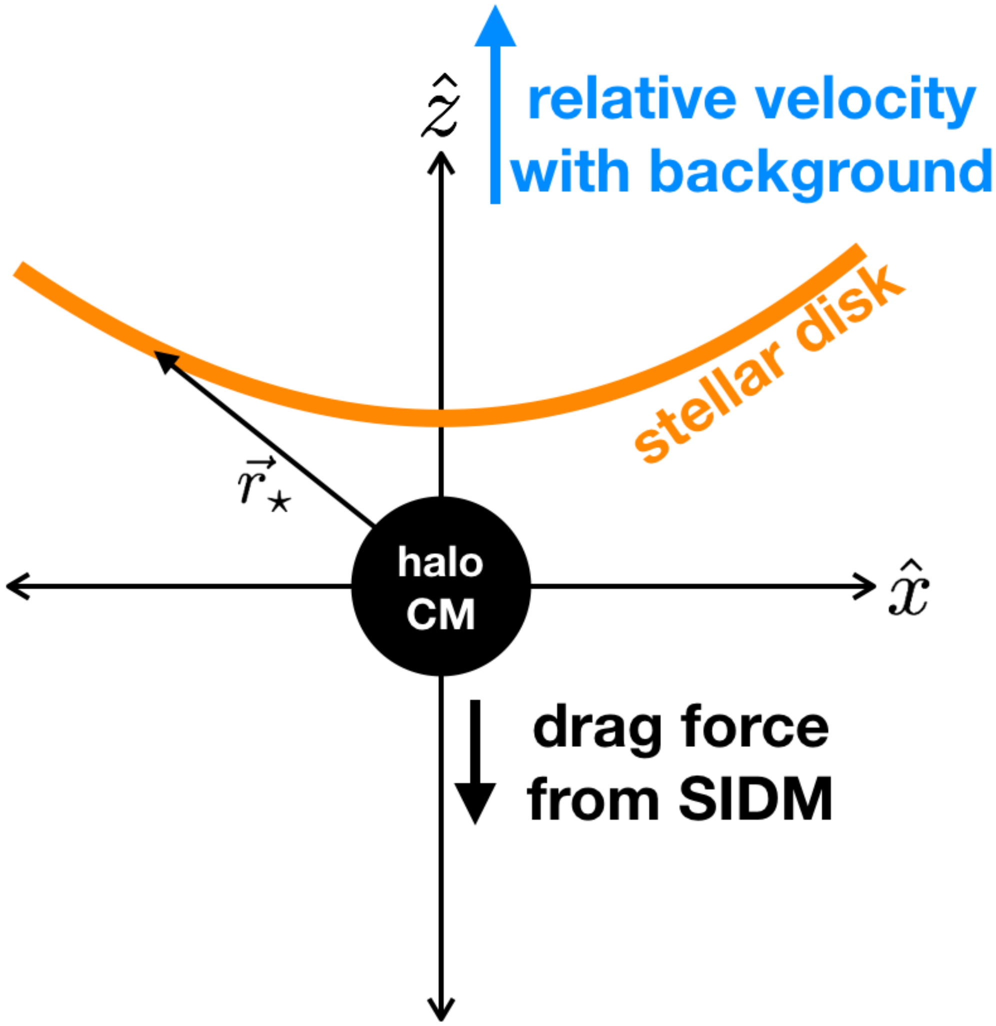

Figure 4.1: Cartoon of how a warp is induced by SIDM. In this picture, the galaxy's stellar disk (orange) and its halo (the center of mass, CM, of the halo is given as the black circle) are falling within an ambient dark matter medium with the relative velocity indicated by the blue arrow. As they fall, the halo experiences a drag force from DM self-interactions, but the stars are collisionless and continue unimpeded. This causes a separation between the centers of the disk and halo, which bends the disk into a U-shaped warp.

Let us define the center of the halo to be at the origin of an $x - z$ plane, where $\hat{z}$ points along the disk normal (see Figure 4.1). The stars are collisionless, but the halo is subject to the drag force derived above. The total acceleration of the halo is:

$$\vec{a}_{\mathrm{h}} = \vec{a}_{\mathrm{bg}} - \vec{a}_{\mathrm{drag}} \ , \tag{4.16}$$

where $\vec{a}_{\mathrm{bg}}$ is the gravitational acceleration due to surrounding matter and $\vec{a}_{\mathrm{drag}}$ is the drag acceleration due to SIDM. The total acceleration of a point on the stellar disk is:

$$\vec{a}_{\star} = \vec{a}_{\mathrm{bg}} - \frac{GM_{\mathrm{h}}}{r_{\star}^2}\hat{r} \ , \tag{4.17}$$

where $r_{\star}$ is the equilibrium distance from the point to the center of the halo and M_h is the halo mass enclosed within $r_{\star}$. The second term is the restoring force caused by the offset of the disk from the halo center.

Since we are looking for the equilibrium positions of the stars, we will require that the stars and DM halo move together. This sets $\vec{a}_{\star} = \vec{a}_{\mathrm{h}}$, which gives:

$$\vec{a}_{\mathrm{drag}} = \frac{GM_{\mathrm{h}}}{r_{\star}^2}\hat{z} \ . \tag{4.18}$$

If we assume a spherically-symmetric halo, then the points along the stellar disk will experience different accelerations:

$$\vec{a}_{\mathrm{drag}} = \frac{GM_{\mathrm{h}}}{r_{\star}^2}\hat{z}\cos\theta = \frac{GM_{\mathrm{h}}}{r_{\star}^2}\hat{z}\left(\frac{z}{x}\right) \ . \tag{4.19}$$

We will assume that the warp is slight and thus $x \approx r_{\star}$. This now allows us to write an equation for the z positions of the stars in terms of the drag and the mass of the background halo:

$$z = a_{\mathrm{drag}}\frac{|x|^3}{GM_{\mathrm{h}}} \tag{4.20}$$

To go further, we must assume a mass profile for the halo. We will use a power-law density profile

$$\rho(r) = \rho_s \left(\frac{r_s}{r}\right)^n \tag{4.21}$$

within the extent of the disk, with scale radius r_s, $\rho(r_s) \equiv \rho_s$, and a free index n (e.g., $n = 1$ for an NFW profile). This gives an enclosed mass $M_h = 4\pi\rho_s/(3-n)r_*^{3-n}$. Substituting this in to our equation for the warp curve above, we find:

$$z = a_{\rm drag}\frac{3-n}{4\pi\rho_s}|x|^n \; . \tag{4.22}$$

In order to compare to observations, we would like a summary statistic that can quantitatively describe the warp. We will employ the w_1 statistic used by Vikram et al. (2013) & Desmond et al. (2018a) – this is essentially a measure of the average z position across the disk:

$$w_1 = \frac{2}{L^3}\int_0^L z'x \, dx \; , \tag{4.23}$$

where $z' = z - \langle z\rangle$, $\langle z\rangle$ is the average $z(x)$ value across the disk, and we implicitly assume a stellar disk that is symmetric about the z axis. Substituting in Equation 4.22 and integrating, we find:

$$w_1 = \frac{n(3-n)}{(n+1)(n+2)}\frac{a_{\rm drag}}{4\pi G\rho_s}\left(\frac{L}{r_s}\right)^n \frac{1}{L} \; . \tag{4.24}$$

4.2 Methods

In this section, we describe the construction of our galaxy sample and explain how we measure the warp curve. Then we describe our model for the estimated warp produced by SIDM.

4.2.1 Candidate selection & warp measurement

We use the NASA Sloan Atlas (NSA) (Blanton et al., 2011) v.1.0.1 catalog[2], a catalog based mainly on Sloan Digital Sky Survey (SDSS) photometry, to select our galaxies. This catalog contains 641,409 galaxies. General quality cuts (positive mass, radius, flux, and redshift measurements) reduce this number to 640,566. We select only those galaxies that have stellar mass greater than $10^9\ M_\odot$ and an axis ratio of $b/a = 0.15$, which leaves us with 22,414 galaxies. This mass cut allows us to use abundance matching to set the dark matter halo masses for our galaxies: the galaxy–halo connection for lower-mass galaxies is considerably more uncertain. The axis ratio cut selects galaxies that are both thin and viewed edge-on. There is some degeneracy between inclination and warp – an inclined galaxy will always have a smaller warp measurement if we do not properly account for the inclination. Selecting only edge-on galaxies therefore makes the warp curve measurement more robust. We select galaxies within 250 Mpc, which allows us to use the BORG algorithm to estimate the background density at their positions (see below). Finally, we cut 5 galaxies with defects in their images (cosmic ray streaks across the disk or no galaxy in the r-band image at the NSA catalog position or corrupted image file). This leaves a final sample of 3,213 galaxies.

To measure the warp curves, we employ the methods of Desmond et al. (2018a). We give a short summary of the procedure here. First, we rotate the r-band image of a galaxy such that the major axis is aligned with the 'x-axis'. The warp curve is given by the intensity-weighted z value at each x slice. We then measure the warp using the w_1 statistic introduced in Vikram et al. (2013):

$$w_{1,\mathrm{obs}} = \frac{\int_{-L}^{L} \frac{x}{L}\frac{z}{L}\frac{dx}{L}}{\int_{-L}^{L} \frac{x}{L}\frac{dx}{L}} = \frac{1}{L^3}\int_{-L}^{L} xz\ dx\ , \tag{4.25}$$

---

[2] `https://www.sdss.org/dr13/manga/manga-target-selection/nsa/`

where integration from $-L$ to L allows for asymmetry across the 'z-axis' (perpendicular to x on the plane of the sky). In practice, we set $L = 3R_{\text{eff}}$, where R_{eff} is the stellar effective radius.

4.2.2 Parameters for estimating the warp

To calculate the expected warp due to SIDM, we require several pieces of information for each galaxy: the effective radius of the stellar disk (R_{eff}), the density of the background at the position of the galaxy (ρ_{bg}), the relative velocity between the galaxy and the background overdensity (v), the angle between this relative velocity and the disk normal (θ), the scale radius of the DM halo (r_s), the density of the DM halo at the scale radius (ρ_s), the power-law index for the DM density profile (n), and the velocity dispersion of the halo (v_{disp}).

We estimate R_{eff} by multiplying the measured Sersic half-light radius from the NSA catalog, `SERSIC_TH50`, by the angular diameter distance to the galaxy[3], with the redshift given by the NSA parameter `ZDIST`.

We find the halo parameters (r_s, ρ_s, and v_{disp}) using halo abundance matching and N-body simulations. Abundance matching (AM) assigns dark matter halos to galaxies by assuming a positive, monotonic relationship between the luminosity or stellar mass of the galaxy and the 'proxy', a function of the halo mass and concentration (Kravtsov et al., 2004). Specifically, we use the AM model of Lehmann et al. (2017), which maps the r-band absolute magnitude, M_r, to a halo proxy given by $v_{\text{vir}}(v_{\text{max}}/v_{\text{vir}})^{\alpha}$, with a Gaussian scatter σ_{AM}. We take the values $\alpha = 0.6$ and $\sigma_{\text{AM}} = 0.16$ dex, which best reproduce clustering statistics. We use the DARKSKY-400 simulation (Skillman et al., 2014) post-processed with the ROCKSTAR halo finder (Behroozi et al., 2013) for the halo properties. For each matched galaxy–halo pair we calculate r_s and ρ_s from the ROCKSTAR output, assuming an NFW profile (Navarro et al.,

---

[3] We assume a flat ΛCDM cosmology with $h = 0.7$, $\Omega_\Lambda = 0.7$, and $\Omega_m = 0.3$ for this calculation.

1997). Velocity dispersions, v_{disp}, are calculated by applying the virial theorem to the halos.

The density of the background, ρ_{bg}, is estimated from the Bayesian Origin Reconstruction from Galaxies (BORG) algorithm (Jasche et al., 2010; Jasche & Wandelt, 2012, 2013; Jasche et al., 2015; Jasche & Lavaux, 2015; Lavaux & Jasche, 2016; Jasche & Lavaux, 2019). This algorithm reconstructs the dark matter density field with a resolution of ∼2.3 Mpc/h out to ∼250 Mpc by forward-modeling primordial density perturbations with a particle–mesh code and comparing this to the number density field of galaxies in the 2M++ survey (Lavaux & Hudson, 2011). To fill in the smaller-scale power, we also include the mass associated with the 2M++ galaxies themselves, which are linked to halos using the same AM routine as above (Desmond et al., 2018b).

We use one of two models for galaxy velocities. First, we set v to the same constant for all of our galaxies, where we consider velocities from $50 - 10,000$ km/s. This is clearly an idealized case, but it gives us a basic idea of the constraining power of our dataset. Second, we use the CosmicFlows-3 (CF3) catalog (Tully et al., 2016) of peculiar velocities. We first assign each galaxy a peculiar velocity, v_{pec}, belonging to the CF3 galaxy closest to it in 3D space. We then assume that the galaxy is falling towards the nearest 2M++ galaxy. The SIDM prediction for the warp we see on the sky is proportional to the relative velocity projected onto the sky. We assign the galaxy velocity in the plane of the sky to be equal to the peculiar velocity.

We must then subtract the velocity of the ambient dark matter medium. We use the public large-scale velocity maps of (Carrick et al., 2015) for this purpose,[4] evaluated at the positions of our galaxies. These maps are estimated using linear perturbation theory and a reconstruction of the large-scale density in the nearby Universe from the 2M++ catalog. They have resolution 4 Mpc/h, and do not provide

---

[4] `https://cosmicflows.iap.fr/`

uncertainty information. We take each of these background velocities and project them onto the sky. We then subtract this velocity from the total galaxy velocity on the sky. The magnitude of this projected velocity is what we call v. We then assign the on-sky angle between this velocity and the disk normal, θ, again assuming that our galaxy is falling towards the nearest 2M++ galaxy. The CF3 peculiar velocities and 2M++ galaxy directions should give us a better idea of the order of magnitude of these relative velocities. However, we also consider fractions f of the relative velocity when we use the CF3 velocities – from $1 - 500\%$. Note that all of our velocities are in the CMB restframe.

We note that the relative velocities we find here are similar to those seen in simulations. We find that the distribution of fractional velocity differences ($(v_{\rm halo} - v_{\rm LS})/v_{\rm halo}$, with $v_{\rm halo}$ the average velocity of DM particles within $R_{\rm vir}$ and $v_{\rm LS}$ the average velocity of DM particles out to 10 $R_{\rm vir}$ in the direction of halo velocity) in the Horizon-AGN simulation (Dubois et al., 2014) is similar to that of the galaxies in our model, with $v_{\rm halo}$ approximated by $v_{\rm CF3}$ and $v_{\rm LS}$ from the large-scale velocity reconstruction described above. This indicates that the level of halo velocity bias (Biagetti et al., 2014; Baldauf et al., 2015; Chen et al., 2018b) in our model is similar to that predicted by cosmological hydrodynamical simulations.

Parameter	Source of Uncertainty	Model Used
$P(n)$	Inner DM halo density slope	Uniform prior $n \in [0.5, 1.5]$
$P(\rho_s, r_s \mid M_r; \alpha, \sigma_{\rm AM})$	Stochasticity in galaxy–halo connection	200 mock AM catalogs at fixed α and $\sigma_{\rm AM}$
$P(\rho_{\rm bg}\|\vec{x})$	Background DM density	10 draws from BORG posterior
$P(v)$	Galaxy relative velocity	Delta function at set velocity (see Sec. 4.2.2)
$P(\theta)$	Unknown relative velocity direction	Delta function at set angle (see Sec. 4.2.2)

Table 4.1: Priors used to find the likelihood of the warp statistic for given $\tilde{\sigma}/m_{\rm DM}$ and m.

With all of these parameters, we can calculate the predicted w_1 statistic for each galaxy using Equation 4.24, for any given $\tilde{\sigma}/m_{\rm DM}$. However, this equation is for a single set of parameter values. We instead want a likelihood function for w_1 that takes into account the uncertainties on these parameters. For each parameter, we either set it directly (v, θ, R_{eff}) or we sample over some prior distribution (all the rest). For the halo parameters, we perform the AM step independently 200 times, in each case producing a slightly different galaxy–halo connection due to the stochasticity introduced by σ_{AM}. This generates distributions for ρ_s and r_s, separately for each galaxy. We then build our prior for the background density, ρ_{bg}, by finding the density within BORG at the position of the galaxy, $\vec{x}$, at 10 independent steps of the BORG Markov chain. Finally, we use a uniform prior for n from 0.5 to 1.5 independently for each galaxy. This range is chosen to include the NFW value ($n = 1$) as well as profiles that are slightly shallower or steeper.

We then perform Monte Carlo sampling for each galaxy independently to determine the w_1 likelihood function. Since $w_1 \propto \tilde{\sigma}/m_{\text{DM}}$, we can generate the likelihood function at $\tilde{\sigma}/m_{\text{DM}} = 1\ \text{cm}^2/\text{g}$ and then simply scale it up or down when sampling $\tilde{\sigma}/m_{\text{DM}}$:

$$\begin{aligned}\mathcal{L}\left(w_1\middle|\frac{\tilde{\sigma}}{m_{\text{DM}}} = 1\ \text{cm}^2/\text{g}, \text{m}\right) = \int \mathcal{L}\left(w_1\middle|\frac{\tilde{\sigma}}{m_{\text{DM}}} = 1\ \text{cm}^2/\text{g}, \text{m}, \rho_{\text{s}}, \text{r}_{\text{s}}, \text{n}, \rho_{\text{bg}}, \text{v}, \theta\right)\\ \times \mathcal{L}\left(\rho_s, r_s \mid M_r; \alpha, \sigma_{\text{AM}}\right) \mathcal{L}(\rho_{\text{bg}}, v \mid \vec{x})\\ \times P(\theta) P(n)\ d\rho_s\ dr_s\ d\rho_{\text{bg}}\ dv\ d\theta\ dn\ ,\end{aligned} \tag{4.26}$$

where the probability distributions for each of these priors is given in Table 4.1. We test for convergence of the likelihood function for each galaxy by requiring that the mean, variance, and skew of $\mathcal{L}(w_1|\tilde{\sigma}/m_{\text{DM}} = 1\ \text{cm}^2/\text{g}, \text{m})$ does not change by more than 1% in the last 10% of the samples, which we find requires at least 100,000 Monte Carlo draws from the prior distributions. Note that by building these distributions directly into the likelihood we are effectively sampling from the priors in these quantities rather than the posteriors, which would be computationally too expensive.

4.2.3 Parameter inference

We now have a measured warp statistic for each galaxy, $w_{1,\mathrm{obs}}$, and the likelihood of a given warp statistic under an SIDM model with $\tilde{\sigma}/m_{\mathrm{DM}} = 1\ \mathrm{cm}^2/\mathrm{g}$. This enables us to derive constraints on $\tilde{\sigma}/m_{\mathrm{DM}}$ and m using Bayes' theorem and a Markov Chain Monte Carlo (MCMC) algorithm. Note that Equation 4.24 is linear in $\tilde{\sigma}/m_{\mathrm{DM}}$ and in the other factors that affect the particular physics of the interactions, outside of m. Thus, for our parameter estimation of $\tilde{\sigma}/m_{\mathrm{DM}}$, we simply sample from $\mathcal{L}(w_1|\tilde{\sigma}/m_{\mathrm{DM}} = 1\ \mathrm{cm}^2/\mathrm{g}, \mathrm{m})$ and then scale by the particular $\tilde{\sigma}/m_{\mathrm{DM}}$ value the Markov chain is sampling. We then compare this to the measured $w_{1,\mathrm{obs}}$ value for each galaxy, as described below. In the contact and long-range cases, we fix m at the appropriate values and do not sample over it.

For the most part, the measured warp values are many orders of magnitude larger than the estimated warp parameters, given a reasonable cross section. In other words, noise dominates the warp signal. Given that we have no reasonable model for how other processes may produce U-shaped warps, we assume that the noise is normally distributed and marginalise over its variance, $\sigma^2_{w_1}$. This modifies the w_1 likelihood to:

$$\mathcal{L}\left(w_{1,\mathrm{obs}}\middle|\frac{\tilde{\sigma}}{m_{\mathrm{DM}}}, m, \sigma_{w_1}\right) = \int \frac{dw_1}{\sqrt{2\pi\sigma^2_{w_1}}} \times \mathcal{L}\left(w_1\middle|\frac{\tilde{\sigma}}{m_{\mathrm{DM}}}, m\right) \exp\left[\frac{-(w_{1,\mathrm{obs}} - w_1)^2}{2\sigma^2_{w_1}}\right], \tag{4.27}$$

In practice, we evaluate this integral by discretizing w_1 into 50 bins between its minimum and maximum values, separately for each galaxy.

We sample this likelihood using the *emcee* affine-invariant Markov sampler (Foreman-Mackey et al., 2013). We set the flat prior $\tilde{\sigma}/m_{\mathrm{DM}} \in (0, 10^4)$ and check that varying this prior does not significantly change the results. For the intermediate-range results, we sample $\log_{10}(\tilde{\sigma}/m_{\rm DM}/[{\rm cm}^2\ {\rm g}^{-1}]) \in (-20, 2)$. The power-law index, m, has a flat linear prior over $m \in [0, 4]$. Finally, we sample in $\log_{10}\sigma_{w_1}$, with no restrictions on its range.

For the contact and long-range interactions, we use 10 walkers and take 20,000 samples, after burn-in. This gives a Gelman-Rubin convergence parameter $R < 0.01$. For the intermediate-range case we require $\gtrsim 25,000$ samples after burn-in to give the same level of convergence.

4.3 Results

Our main results are:

1. There is no preference for SIDM ($\tilde{\sigma}/m_{\rm DM} > 0$) over the null hypothesis that warps are generated purely by astrophysical or measurement noise. This indicates no net correlation between the direction of the warps and the galaxy velocities on the plane of the sky, or between the warp magnitude and the expectation of Equation 4.24.[5]

2. For contact interactions, we find a 1σ limit of $\tilde{\sigma}/m_{\rm DM} < 0.5$ cm^2/g for fixed galaxy velocity $v = 300$ km/s. Assuming all galaxies have the same velocity, this limit scales as $\sim v^{-2}$ for $v < 1000$ km/s. If we use the fractions of the CF3 velocities, we find that the limit scales as $\sim v^{-1.8}$. Overall, we place a range of 68% upper bounds on the cross section from $\tilde{\sigma}/m_{\rm DM} \lesssim 0.2-60$ cm^2/g, assuming a galaxy velocity from $v \sim 10^4$ km/s $-$ 50 km/s or alternatively considering a galaxy-by-galaxy variation in v, in accordance with the CF3 results.

3. For long-range interactions, we place a limit of $\tilde{\sigma}/m_{\rm DM}(v = 300\ {\rm km/s}) < 3 \times 10^{-13}$ cm^2/g, scaling as $\sim v^{1.0}$ assuming a constant velocity $v < 1000$ km/s. This

---

[5] This is predictable from the results of Ref. Desmond et al. (2018a), who show that there *is* a positive correlation between the warp direction and the orientation of the fifth-force field in thin-shell-screened modified gravity theories, which is largely anti-aligned with galaxies' velocities.

scaling goes as $\sim v^{-0.028}$ for the velocities set using fractions of the CF3 velocities. Including the possibility of variation in the galaxy velocities, we find a range of 68% upper bounds on the cross section from $\tilde{\sigma}/m_{\rm DM} \lesssim 2\times10^{-13} - 10^{-10}$ cm^2/g, with assumed median galaxy velocity from $v \sim 50$ km/s $- 10^4$ km/s.

4. For intermediate-range interactions we find that contact-like drag forces are marginally preferred, with a corresponding constraint on the cross section.

In the rest of this section, we use different assumptions about the relative velocities of our galaxies to give more detailed results. These results are summarized in Figures 4.2–4.5, and Table 4.2. Note that in all cases we marginalize over the variance of the noise term, σ_{w_1}. We find that σ_{w_1} is not degenerate with any other model parameter and its posterior is invariant for all of the models we consider. It is peaked at the measured variance of $w_{1,\rm obs}$, indicating that it picks up the overall magnitude of the measured warps. The constraints on SIDM parameters instead depend on the correlation of $\hat{w}_1$ with environment and galaxy/halo properties.

For the contact interactions case, we give our main results in Figure 4.2. As described in Section 4.2.2, we use either of two assumptions for the velocities: 1) we set all velocities to the same value; or 2) we set the velocities to some fraction of the measured velocities from the CF3 data. The limit on the cross section differs by at most a factor ~ 2 between these models. Our limits for average velocities greater than ~ 500 km/s are tighter than the Bullet Cluster constraints (Markevitch et al., 2004; Randall et al., 2008; Kahlhoefer et al., 2014). In Figure 4.3, we show how the evaporation and velocity dispersion effects change our limits. Adding both of these effects, as is done in all other figures, weakens our limits by about one order of magnitude, regardless of the velocity scale.

Our long-range limits are given in Figure 4.4. As with the contact case, we report our limits as a function of the assumed velocity and include two curves with the different velocity models. The results in Figure 4.4 include the effects of velocity

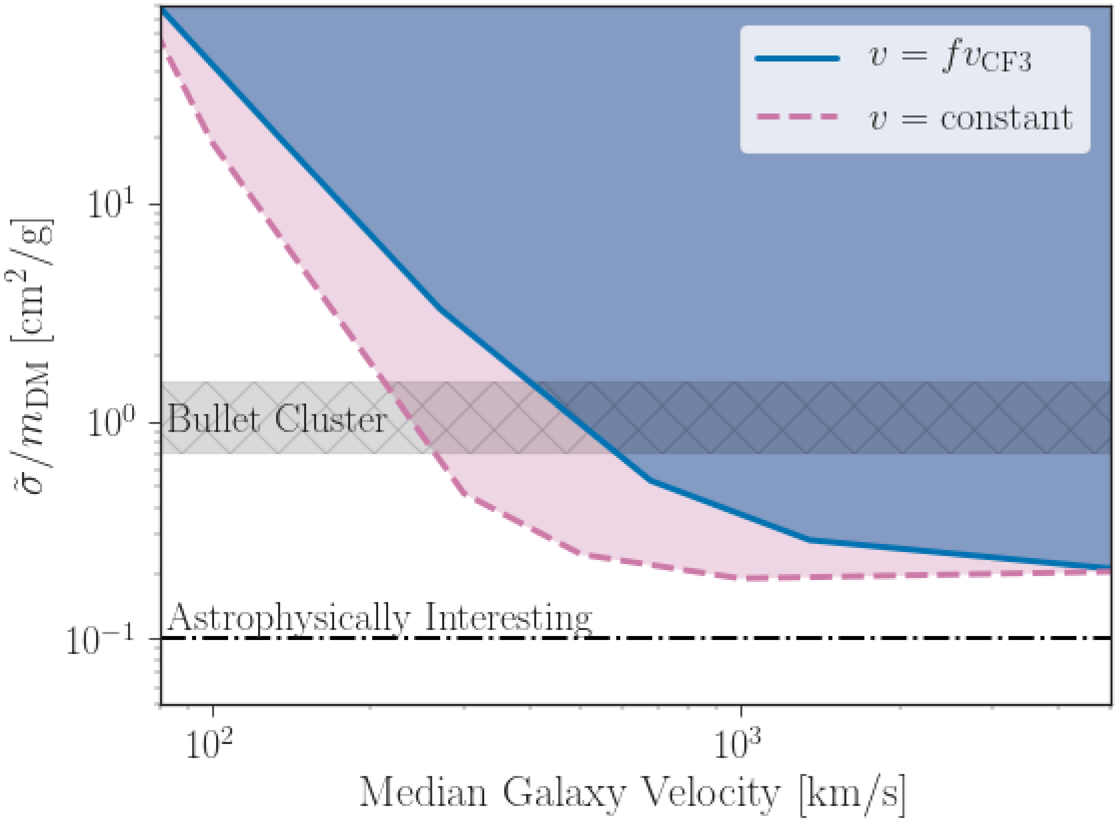

Figure 4.2: 68% upper limits on the SIDM cross section assuming a contact interaction versus the median assumed velocity. We show our limits assuming all galaxies have the same relative velocities (pink) and assuming they have velocities set by some fraction of their CF3 velocities (blue). The grey, hatched region gives the range of constraints on the cross section from the Bullet Cluster (Markevitch et al., 2004; Randall et al., 2008; Kahlhoefer et al., 2014). The dotted-dashed line gives the minimum SIDM cross section needed to provide astrophysically interesting effects (i.e., suppression of small scale structure and DM halo cores; Rocha et al., 2013).

dispersion but not evaporation (see Section 4.1). We find our limits to be considerably stronger than those from dwarf galaxy evaporation (Kahlhoefer et al., 2014).

Finally, we consider the intermediate case in Figure 4.5. This shows the posterior distributions for $\tilde{\sigma}/m_{\mathrm{DM}}$ and m, the power-law index for the velocity dependence of the interaction. Contact interactions (low m values) are slightly preferred, although this may be solely because they allow a larger volume of the $\tilde{\sigma}/m_{\mathrm{DM}}$ prior. As in the other cases, the limits on $\tilde{\sigma}/m_{\mathrm{DM}}$ strengthen when higher velocities are assumed;

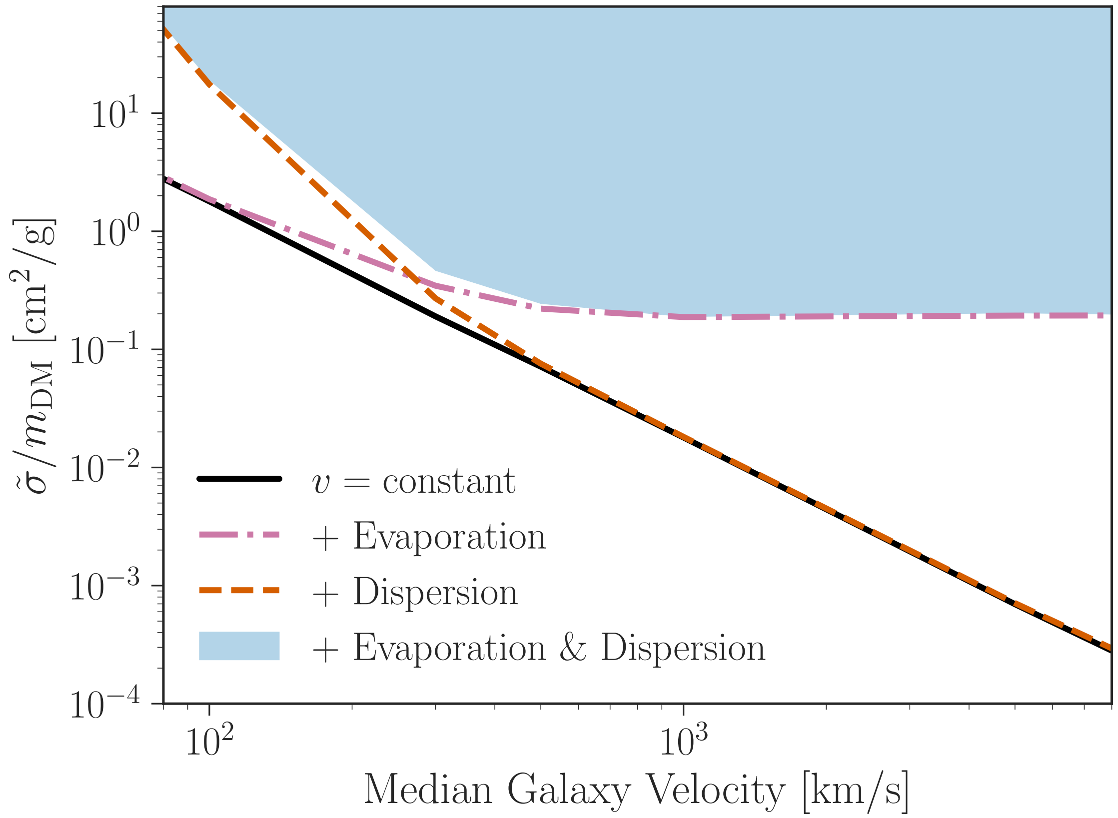

Figure 4.3: 68% upper limits on the SIDM cross section assuming a contact interaction versus the median assumed velocity. Here we show the effects of velocity dispersion and evaporation on our results. The black line shows the limits if we do not consider either of these physical effects. The pink, dotted-dashed line includes evaporation and the orange, dashed line includes velocity dispersion. The blue region shows the same limits as Figure 4.2, which includes both effects.

however, this does not significantly affect the m posterior. Note that we use a log-prior on the cross-section in this case due to the enormous width of the posterior as m varies. However, since the posterior peaks at $\tilde{\sigma}/m_{\mathrm{DM}} = 0$ cm^2/g, confidence limits depend on the arbitrary lower limit of the prior and are therefore not reliable. The shapes of the posteriors and their dependence on velocity are nevertheless robust.

Interaction Type	Assumed Velocity km/s	Evaporation?	Dispersion?	68% Upper Limit cm^2/g	95% Upper Limit cm^2/g
contact	$v = 300$	-	-	0.19	0.43
		✓	-	0.35	0.76
		-	✓	0.27	0.61
		✓	✓	0.46	1.0
	$v = v_{\rm CF3}$	-	-	0.032	0.071
		✓	-	0.26	0.49
		-	✓	0.033	0.073
		✓	✓	0.28	0.53
long-range	$v = 300$	N/A	-	2.0×10^{-13}	4.4×10^{-13}
		N/A	✓	2.7×10^{-13}	6.1×10^{-13}
	$v = v_{\rm CF3}$	N/A	-	4.7×10^{-14}	1.2×10^{-13}
		N/A	✓	3.9×10^{-13}	9.4×10^{-13}

Table 4.2: Limits on the self-interaction cross section for contact and long-range interactions

4.4 Discussion

Our results in the previous section show that we can place new constraints on the SIDM cross section by measuring the warps of stellar disks. In this section, we discuss possible systematics and how we attempt to mitigate them. We also discuss the prospects for improving constraints with next-generation surveys.

As shown in Figures 4.2 and 4.4, the bounds on the cross section are dictated by the magnitudes of the galaxies' relative velocities. We have provided a range of constraints based on different reasonable assumptions, but more robust limits require more precise velocity measurements. The CF3 velocities have very large errors, in excess of 100% at times. In addition, the CF3 catalog does not include most of the galaxies in our sample, forcing us to assign velocities by means of a nearest neighbour algorithm. Most of our sample is within ~ 10 Mpc of a CF3 galaxy. We find that, within the CF3 catalog, the velocities are well-correlated on these scales. We therefore expect this to be an adequate estimator of the true velocity, but caution that it must

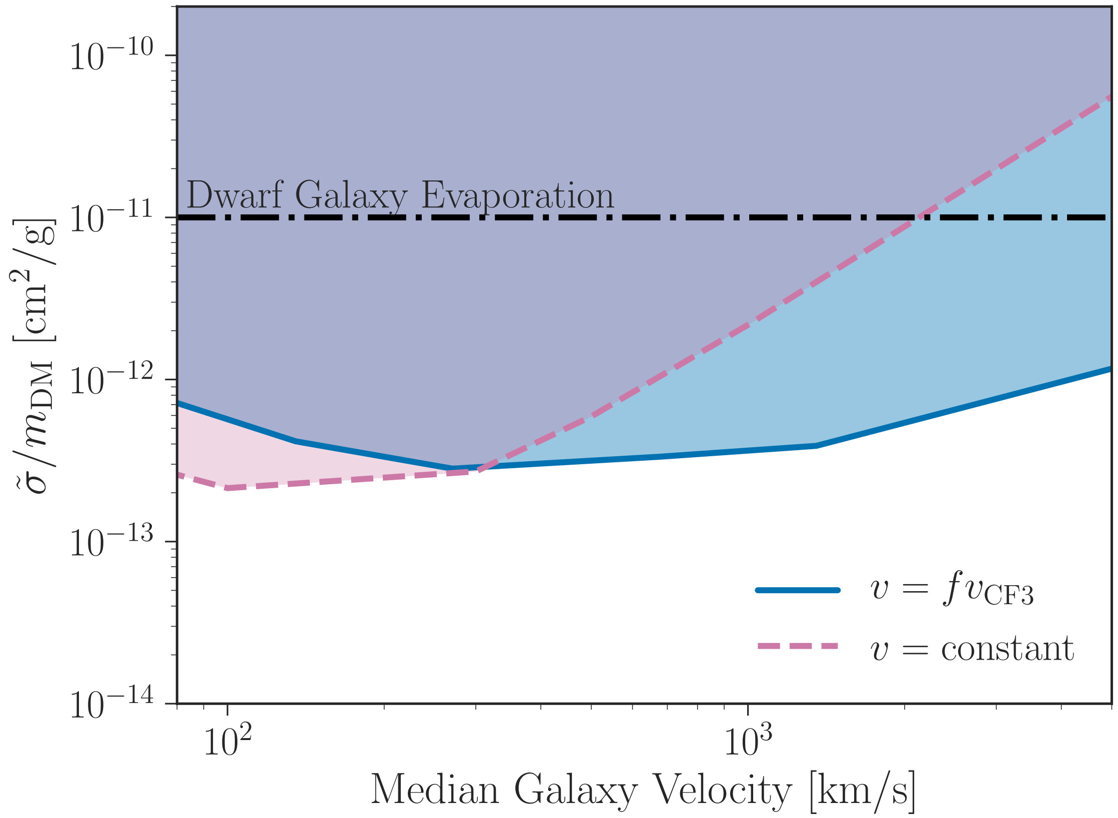

Figure 4.4: 68% upper limits on the SIDM cross section assuming a long-range interaction versus the median assumed velocity. We show our limits assuming all galaxies have the same relative velocities (dashed, pink) and assuming they have velocities set by some fraction of their CF3 velocities (solid, blue). The black, dotted-dashed line gives an upper limit from dwarf galaxy evaporation rates (Kahlhoefer et al., 2014).

introduce some uncertainty. Note also that we do *not* include uncertainties on the peculiar velocities in our likelihood function. Since the warp depends on the square of the velocity, including Gaussian (or log-normal) uncertainties always leads to a larger predicted warp and hence a tighter constraint on the cross section. Our model is therefore conservative in this regard.

Another possible systematic is the effect of baryonic physics on galaxy morphology. Most warps caused by tidal or baryonic effects are S-shaped (Binney, 1992), and are therefore effectively filtered out by our choice of warp statistic. Any non-SIDM contribution to w_1 is captured to leading order by our noise model (marginalization over σ_{w_1}), but only under the assumption that this contribution is Gaussian and independent of environment and galaxy/halo properties. Baryonic and tidal effects are likely to break this assumption to some degree. In addition, gas in the galaxy will experience hydrodynamical drag from interaction with gas in the intergalactic medium (IGM), which will lead to a U-shaped warp in the same direction as SIDM. Thus, including this IGM contribution would tighten our limits, making our current results again conservative. The location of the gas as well as the dependence of the measured warp on gas mass would help break the degeneracy between these two types of physics in the context of future, more precise constraints.

We also neglect the effects of tidal interactions, which could contribute to anisotropy in halo and galaxy profiles. However, this effect would be largest within clusters while our galaxies are mainly in the field, so we do not expect it to significantly bias our results..

On the theory side, we use the fluid approximation to derive the SIDM prediction for the warp. However, given the low background densities (like most late-types, our galaxies tend to reside in the field), the fluid approximation is likely not valid for the contact interaction case. The average background densities near our galaxies is $\rho_{\rm bg} = 330\ M_\odot/{\rm kpc}^3 \sim 2.4\rho_{\rm crit}$, where $\rho_{\rm crit}$ is the critical density today. For $v = 300\,{\rm km/s}$ and $\tilde{\sigma}/m_{\rm DM} = 1\ {\rm cm}^2/{\rm g}$ this gives an interaction time larger than $1/H_0$. We thus caution that the contact interaction results are subject to larger uncertainty. The long-range results also depend on the fluid approximation, but there are many more interactions because of the nature of the force – the interaction times for this case are closer ~ 50 Myr, which is less than the typical dynamical times for these galaxies. These results are therefore more robust.

Finally, we neglected to include the self-gravity of the disk in our calculations. Desmond et al. (2018a) found this to be a negligible effect, thus we do not include those calculations here. However, as imaging and analysis techniques improve, disk self-gravity may become a relevant systematic.

With the coming era of large and deep photometric surveys (e.g., LSST[6] (LSST Science Collaboration et al., 2009), WFIRST[7] (Spergel et al., 2013), and Euclid[8] (Laureijs et al., 2012)), we can expect to have a much larger sample of edge-on galaxies to test in the future. Assuming that we can continue to measure the properties of the DM background (density and velocity) in these survey volumes and the galaxies' peculiar velocities, we can expect these samples to yield considerably tighter constraints. To quantify this, we repeat our analysis for the contact interaction case (with $v = 300$ km/s and without the velocity dispersion and evaporation effects) using random subsets of size N of our galaxy sample. This produces a range of results depending on the subset of galaxies chosen. For each subset size, we record the 68% upper limits on $\tilde{\sigma}/m_{\mathrm{DM}}$. We find that the upper 16% of these limits is well fit by $\sigma/m_{\mathrm{DM}}|_{1\sigma} \propto N^{-0.9}$. In other words, in the worst case scenario that all of the future galaxies we obtain have the same constraining power as our least-constraining few hundred galaxies, we will tighten our limits by a factor of ∼2.8 with 10,000 galaxies. The median limits show that with this same number we can more likely expect at least an order of magnitude better constraints. Thus, with just 10,000 galaxies, we can expect limits capable of totally ruling out self-interactions as an astrophysically interesting DM property. This is even without accounting for any improvements in the velocity determination and other modeling. We can further improve these constraints by finding more thin, edge-on galaxies in high density environments – these would be expected to have the largest warp signature and thus the greatest constraining power. We would also want to choose galaxies at relatively low redshifts and with

---

[6] `https://www.lsst.org/`

[7] `https://wfirst.ipac.caltech.edu/`

[8] `https://www.euclid-ec.org/`

high stellar masses, which would reduce uncertainties both in measuring the warps and assigning halo properties to the galaxies.

In summary, we calculate the expected stellar disk warp due to DM self-interactions for a variety of interaction types and additional physical processes. We then compare these to the measured warps of edge-on disk galaxies in the SDSS to place constraints on SIDM parameters. Our constraints are competitive with limits from the Bullet Cluster and dwarf galaxy evaporation. These results are conservative given our treatment of the interstellar medium and velocity uncertainties, although there remain modeling challenges (e.g., the use of the fluid approximation and the precise values of galaxies' peculiar velocities). Given the strong constraints we have found so far, we believe this to be a fruitful avenue for future work. With more galaxies, better photometry, and more accurate velocities, we can hope to use galaxy structure either to detect SIDM or to rule it out as an astrophysically interesting possibility.

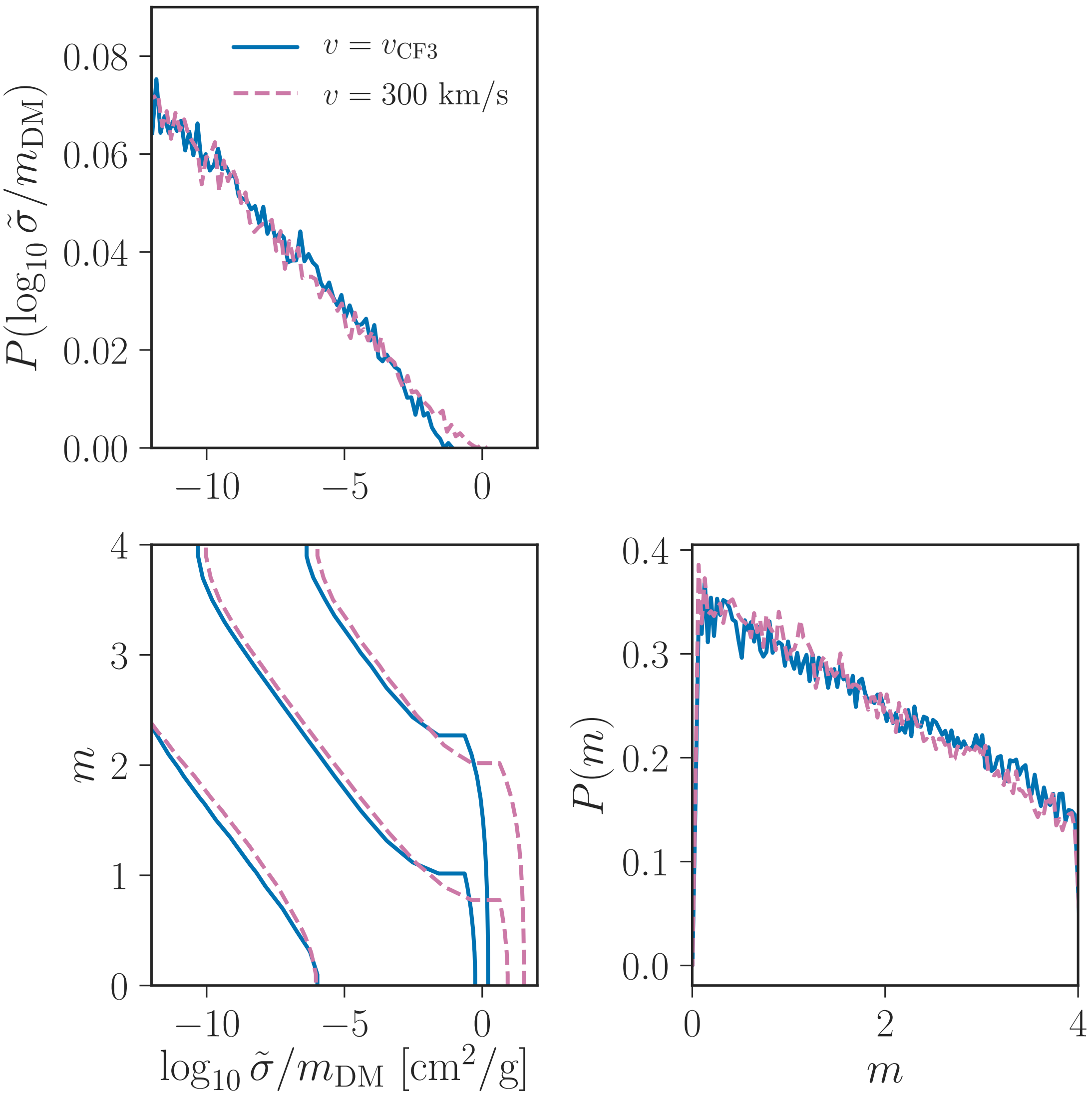

Figure 4.5: Corner plots for the intermediate-range interaction. We show our limits assuming all galaxies have $v = 300$ km/s (pink) and assuming they have velocities set by their CF3 velocities (blue). m determines the dependence of $a_{\rm drag}$ on the relative velocity of the halo and background (Equation 4.12). Note that because we use a Jeffrey's prior here for $\tilde{\sigma}/m_{\rm DM}$ and the posterior peaks at $\tilde{\sigma}/m_{\rm DM} = 0$ cm^2/g, the confidence levels depend sensitively on the arbitrary lower limit of the prior and should not be used: the contour lines in the off-diagonal panel are meant merely to show the degeneracy direction.

Chapter 5

Isolated Dwarf Galaxies & Emergent Gravity

In Emergent Gravity (EG) theory (Verlinde, 2017), gravity emerges from the entanglement of spacetime. According to this theory, dark energy has some entanglement entropy. Baryonic matter displaces dark energy and, due to the volume law contribution to entropy, this causes an elastic response force on the matter. This manifests itself as an extra gravitational force around massive objects. Verlinde (2017) uses this elastic response force ansatz to produce an equation for the "apparent dark matter" given some baryonic mass distribution.

In the limit of a point-source mass, the equation for the apparent dark matter (DM) in EG converges to the weak limit equation from Modified Newtonian Gravity (MOND) (Milgrom, 1983). Thus, Verlinde (2017) manages to derive the Tully-Fisher relation within his theory using *no free parameters* and directly connects the MOND acceleration, a_0, to the energy density in dark energy.

However, EG in its current formulation only applies to the current, deSitter-like Universe. The equations given in Verlinde (2017) are also only valid for spherically symmetric, isolated systems. Nonetheless, there have been several tests of this theory.

Brouwer et al. (2017) study the weak lensing of galaxy clusters, and find it to be consistent with EG. Ettori et al. (2017) find EG to agree with two large, roughly spherical galaxy clusters, and Diez-Tejedor et al. (2018) also find agreement with the mass-to-light ratios of the classical dwarf spheroidal satellite galaxies. Several studies claim that EG is inconsistent with observations: the initial mass functions of massive early-type galaxies (Tortora et al., 2018), the radial acceleration within the inner regions of spiral galaxies Lelli et al. (2017), and the perihelia of Solar system planets Hees et al. (2017). However, all of these tests attempt to apply EG outside of the currently narrow regime where it makes robust predictions: spherically symmetric, isolated systems in the nearby Universe.

In this paper, I extend the EG formalism to include more sophisticated mass profiles that are suitable for predicting the maximum velocities within isolated dwarf galaxies. I then compare these predictions to observations. These systems fulfill all of the requirements of the current formulation of EG, and thus provide the strongest constraints on EG. In Section 2, I derive the equations for specific spherical mass distributions along with the corresponding “apparent” dark matter predicted from EG. In Section 3, I describe how I apply these equations to isolated dwarf galaxies. In Section 4, I compare EG’s predictions for the velocities within isolated dwarf galaxies to those measured in a recent 21 cm study (Bradford et al., 2015). I discuss these results and conclude in Section 5.

5.1 Apparent DM Distribution Predictions from EG for Two Realistic Baryonic Mass Distributions

The goal of this section is to describe the velocity curve for an extended mass distribution in EG. Conservation of energy tells us that the circular velocity, $v(r)$, is given solely by the mass distribution. For standard ΛCDM, we simply use the mass distributions of both the baryonic and DM mass. In EG, we instead derive the apparent dark matter mass distribution from the baryonic mass distribution and then use both of these to find the velocity curve. In this section, I will derive the apparent dark matter mass distributions for a spherically symmetric baryonic mass distribution.

5.1.1 Spherically Symmetric Mass Distribution

For a spherically symmetric, isolated system, the apparent DM predicted by EG (Verlinde, 2017) is

$$\int_0^r \frac{GM_D^2(r')}{r'^2} dr' = \frac{a_0 r}{6} M_B(r) \ , \tag{5.1}$$

where G is Newton's gravitational constant, and $a_0 = cH_0$. By taking the derivative of both sides with respect to r, we find an equation for $M_D(r)$,

$$M_D^2(r) = \frac{a_0 r^2}{6G} \frac{d}{dr}\Big(rM_B(r)\Big) \ . \tag{5.2}$$

Note that if we allow M_B to be a point-mass, then $M_D^2(r) = \frac{a_0 r^2}{6G} M_B$, which would give a gravitational acceleration of

$$g_D(r) = \frac{GM_D(r)}{r^2} = \sqrt{\frac{a_0}{6} g_B(r)} \ . \tag{5.3}$$

This is just the MOND acceleration in the weak-field limit (Milgrom, 1983) with $a_M = \frac{a_0}{6}$. I only include this as an aside – dwarf galaxies are of course not describable as point-masses.

Instead, let us consider an extended mass distribution. In particular, let us employ a deprojected Sérsic profile. These profiles fit the stellar light of galaxies well, and since we are assuming there is no dark matter, this should also be a good measure of the mass.

The Sérsic profile of a galaxy is given by

$$I(R) = I_e \exp\left[1 - b_n \left(\frac{R}{R_e}\right)^{1/n}\right] , \tag{5.4}$$

where I_e and R_e are the intensity and projected radius at the half-light slice, respectively, and n is the so-called Sérsic index, which is a measure of the concentration of the light about the center. The constant b_n is given by gamma functions (see Appendix 5.A).

To find the mass profile, we must first deproject the Sérsic profile to give the luminosity density. Assuming spherical symmetry, we can then integrate in the angular directions to give the radial luminosity profile. Mazure & Capelato (2002) first found the exact solution for the radial luminosity profile given a general Sérsic profile, and I use their results here.

Since we are assuming that there is no dark matter, the mass must follow the light. Then, the stellar mass profile should be the same as the luminosity profile except for some scaling factor, the baryonic mass-to-light ratio, Υ. This ratio, along with the effective intensity simply give the normalization of the function, and thus we let $\Sigma = I_e \Upsilon$, where the process for setting this normalization constant is given in

Section 5.2.2. The final equation for the baryonic mass profile is

$$\begin{aligned} M_B(r) =& 2\pi c_1 \Sigma R_e^2 \left(\frac{r}{R_e}\right)^{\frac{2n+1}{n}} \\ & \times G^{2n,1}_{1,2n+1}\left(c_2 \left(\frac{r}{R_e}\right)^2 \middle| \begin{matrix} \{-\left(\frac{1}{2n}\right)\}, & \{\} \\ \{\beta_s\}, & \{-\left(\frac{2n+1}{2n}\right)\} \end{matrix} \right), \end{aligned} \tag{5.5}$$

where $G^{m,n}_{p,q}\left(z \middle| \begin{matrix} a_1, \ldots, a_p \\ b_1, \ldots, b_q \end{matrix} \right)$ is the Meijer G function (described in Appendix 5.A.2), and the c_1, c_2, and β_s are constants (described in Appendix 5.A.3). Then, the apparent DM predicted by EG due to this realistic mass distribution is given exactly by

$$\begin{aligned} M_D^2(r) =& \frac{\pi a_0 c_1 \Sigma R_e^2}{3G} \left(\frac{r}{R_e}\right)^{\frac{2n+1}{n}} r^2 \\ & \times \left[G^{2n,1}_{1,2n+1}\left(c_2 \left(\frac{r}{R_e}\right)^2 \middle| \begin{matrix} \{-\left(\frac{1}{2n}\right)\}, & \{\} \\ \{\beta_s\}, & \{-\left(\frac{2n+1}{2n}\right)\} \end{matrix} \right) \right. \\ & \left. + 2G^{2n,0}_{0,2n}\left(c_2 \left(\frac{r}{R_e}\right)^2 \middle| \begin{matrix} \{\} & \{\} \\ \{\beta_s\} & \{\} \end{matrix} \right) \right]. \end{aligned} \tag{5.6}$$

For a detailed description of these methods, see Appendix 5.A.

Since this is a spherically symmetric mass distribution, the circular velocity is given by

$$v(r) = \pm\sqrt{\frac{G(M_D(r) + M_B(r))}{r}} \tag{5.7}$$

5.2 Modeling Isolated Dwarf Galaxy Rotation Curves with EG

In this section, I apply my equations from Section 5.1 to real isolated dwarf galaxies. First, I describe the equations employed in the analysis and then I discuss the data.

5.2.1 Theory

Isolated dwarf galaxies contain a significant amount of HI gas that often exceeds the amount of stellar mass in the galaxy (Geha et al., 2006). This HI gas in dwarf galaxies typically extends far beyond the stellar disk (Broeils & Rhee, 1997). Thus, we must include the mass profiles of both the stellar mass and the HI gas mass to properly model the baryonic content of these galaxies.

In addition, real galaxies are not perfect spheres. The equations we have developed here are thus not entirely accurate. However, we expect them to give reasonable approximations. In the Newtonian case, the axisymmetric maximum rotation velocity differs from that of the spherical case by only 15%.

I model the starlight profile as a Sérsic profile with index, n. I model the HI mass profile as a sphere with an exponential density profile – a Sérsic profile with $n = 1$. The scale lengths for each case, $R_\star$ and R_{HI}, and the normalization constants, $\Sigma_\star$ and Σ_{HI}, are given by measured quantities, as described in the next section.

5.2.2 Data

To test EG, I use the Bradford et al. (2015) sample of isolated dwarf galaxies in SDSS DR 8. They choose all galaxies within the NASA Sloan Atlas[1] (NSA) catalog (Blanton et al., 2011) that have $z > 0.002$ and $M_r < 17.72$. They then select according to an isolation criteria: for stellar mass $M_\star < 10^{9.5} M_\odot$, a galaxy is isolated if $d_{\mathrm{host}} >$

---

[1] http://www.nsatlas.org

1.5 Mpc. The full Bradford et al. (2015) sample has 546 isolated dwarf galaxies ($M_\star < 10^{9.5}\ M_\odot$). For each of these galaxies, Bradford et al. (2015) measure the 21 cm peak flux and line width. The HI gas masses are calculated from the peak fluxes. The inferred maximum circular velocity in each galaxy is given by

$$v_{\rm max} = \frac{W_{20}}{2 \sin i\ (1+z)}\ , \tag{5.8}$$

where W_{20} is the width of the 21 cm line at 20% peak flux, i is the inclination of the galaxy, and z is the redshift.

It has been found that face-on galaxies (i.e. galaxies with inclinations below ~ 40 degrees), can have significant errors induced by inclination effects (c.f. Stark et al., 2009). To mitigate any effects from inclination, I select all galaxies with inclinations $i > 45$ degrees from the Bradford et al. (2015) sample. This leaves us with a final sample of 452 galaxies.

For each of the galaxies in the sample, I use the NSA catalog Sérsic fit values for n, $R_\star$, and $M_\star$, and I use the Bradford et al. (2015) values for the HI mass and the measured maximum circular velocities. There are no direct observations of the normalization constants, $\Sigma_\star$, $\Sigma_{d,\star}$, $\Sigma_{\rm HI}$, and $\Sigma_{d,{\rm HI}}$. Instead these must be inferred from other quantities. I set the normalization constant by assuming that the measured mass is contained within five effective radii.

To set the effective radius of the HI gas, $R_{\rm HI}$, I employ the relation by Lelli et al. (2016):

$$\log_{10} M_{\rm HI} = (1.87 \pm 0.03) \log_{10} R_{\rm HI} - (7.20 \pm 0.03)\ , \tag{5.9}$$

where $M_{\rm HI}$ is given in solar masses, and $R_{\rm HI}$ is given in kpc. The intrinsic scatter of the relation is $\sigma_{\rm int} = 0.06 \pm 0.01$ dex.

5.3 Results

Here I present the velocity curves predicted by EG. I also compare the predicted maximum circular velocities from EG to those measured in Bradford et al. (2015). This is a preliminary analysis and should be followed by a full analysis with rotation curves of these galaxies.

To give an idea of the typical velocity curve produced by EG, let us consider the velocity curve of a sample dwarf galaxy with the median values from the data described in Section 5.2.2. These values are all given in Table 5.1.

Parameters	Values
$M_\star$	$3.98 \times 10^8\ M_\odot$
$R_\star$	2.27 kpc
n	1.14
$\Sigma_\star$	$2.33 \times 10^7\ M_\odot$
$\Sigma_{\rm d,\star}$	$1.49 \times 10^7\ M_\odot$
$M_{\rm HI}$	$1.24 \times 10^9\ M_\odot$
$R_{\rm HI}$	10.31 kpc
$\Sigma_{\rm HI}$	$1.95 \times 10^6\ M_\odot\ {\rm kpc}^{-2}$
$\Sigma_{\rm d,HI}$	$1.86 \times 10^6\ M_\odot\ {\rm kpc}^{-2}$
$v_{\rm meas}$	82 km/s

Table 5.1: Median values for isolated dwarf galaxies in sample

The predicted velocity curves from EG for the spherical (solid) and point-source (dotted) cases are given as the blue curves in Figure 5.1. For comparison, I also include the prediction from Newtonian gravity (assuming only baryonic matter), which is given by the black line. The median measured maximum velocity from Bradford et al. (2015) is given by the orange, solid line as a reference.

Note that the maximum for all of the cases occurs at $r \sim 5 - 18$ kpc. This is many times the effective radius of the stellar content. However, it is $\sim 0.5 - 1.7 R_{\rm HI}$.

Thus, it is clear that the HI gas is the main driver behind the shape of the velocity curves, which agrees with the large gas fractions that are observed in these galaxies.

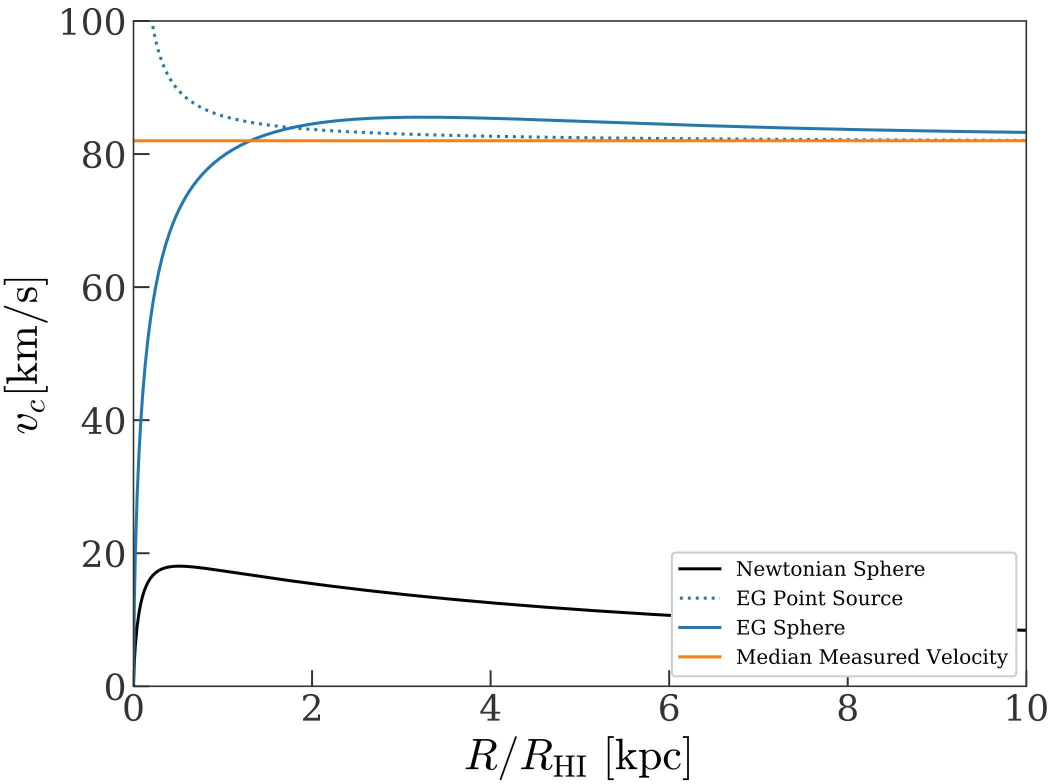

Figure 5.1: Circular velocity as a function of radius for an isolated dwarf galaxy. The blue lines give the prediction from EG assuming a spherical baryonic mass distribution (solid line) or point-source mass distribution (dotted line). The black line gives the Newtonian prediction (i.e. assuming there is only baryonic mass) for a spherical mass distribution. The orange, dashed line gives the median measured maximum velocity from Bradford et al. (2015).

Figure 5.2, shows the estimated maximum circular velocity from EG for the spherical case versus the measured maximum circular velocities from Bradford et al. (2015). If the theory and observations were perfect, then all of the points would lie on the line $y = x$ (black line).

I fit a best fit line to the model (assuming all of the galaxies can be treated independently) using a Markov chain Monte Carlo (MCMC) routine and plot this as the dashed line in Figure 5.2. The best fit slope for the spherical model (blue) is

$m = 0.83 \pm 0.02$ and the best fit intercept is $b = 16.01 \pm 1.35$. This fit does not allow for the "perfect agreement" line with $m = 1$ and $b = 0$. Even if we conservatively allow for twice the estimated error on the estimated velocities, the spherical model would not agree with the "perfect agreement" line. Overall, these are preliminary results and a more careful analysis with rotation curves is needed to provide robust statements.

5.4 Discussion & Conclusions

In this paper, I develop the equations for EG's velocity curve predictions based on a realistic baryonic mass profile. I then apply this model to isolated dwarf galaxies. These galaxies contain large amounts of HI gas, which must be treated separately from the stellar mass. Finally, I compare EG's predictions for the velocities with the HI 21-cm line width measurements from Bradford et al. (2015) for 452 isolated dwarf galaxies. As I show in the results section, the predicted velocities from EG do not agree with the measured velocities.

There are many assumptions made when modeling the baryonic gas mass and it is entirely possible that any of these could be biasing the EG predictions. Perhaps the most error-prone parts of the analysis are the choices for the distributions and the normalization routine.

The baryonic distribution I choose, a spherical distribution based on the Sérsic profile is highly idealistic. Since these galaxies are mostly composed of HI gas, we do expect them to be closer to thin disks than spheres. Specifically, HI gas tends to follow either an exponential or Gaussian distribution within galaxies (Swaters et al., 2002; Martinsson et al., 2016). Equation 5.2 shows that the apparent dark matter surface density increases for larger baryonic potential flux losses through a surface. In other words, the steeper the baryonic distribution, the more apparent dark matter should

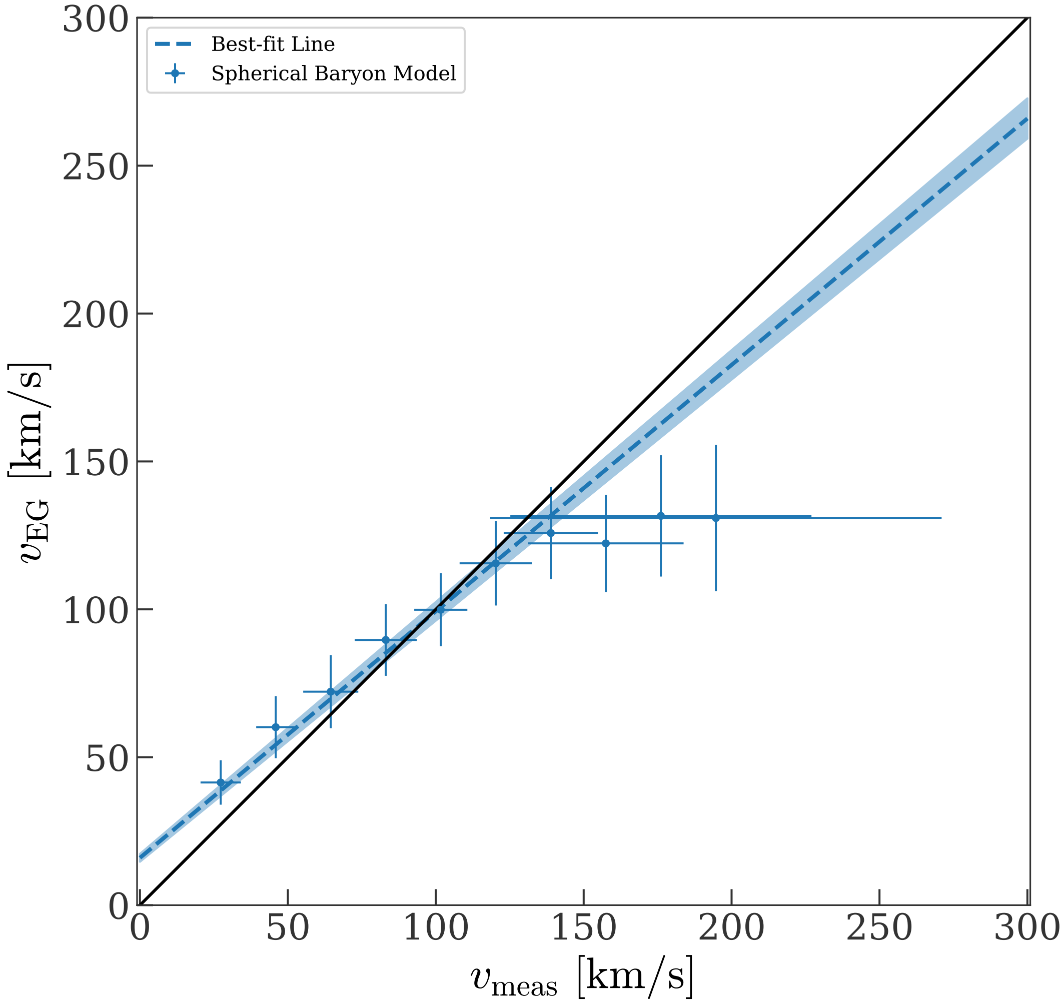

Figure 5.2: Binned predicted maximum circular velocity from EG versus measured maximum circular velocities for isolated dwarf galaxies. The blue points give the results for the spherically symmetric case. The best-fit line to the points is given as the blue, dashed line. The region around the line gives the 1σ confidence interval. If there was a perfect agreement with the measurements, all of the points would lie along the black line.

be in the system, according to EG. Thus, using Sérsic profiles, which are steeper than Gaussian profiles, gives an upper limit on the velocities EG would predict for a profile that mimicked these disk profiles. The use of a steeper distribution may alleviate some of the tension seen in Figure 5.2; however, it is not well supported by observational data.

As I describe in Section 5.2.2, I normalize the mass distribution functions by assuming that all of the mass is contained within five effective radii. This normalization routine for each of the profiles is somewhat arbitrary, and it does have a large effect on the final predicted rotation curves. However, it is not clear that changing the normalization routine would allow the predictions to match the data while remaining consistent with observations of the HI content in disk galaxies. The velocities scale as $v \propto (\Sigma_\star + \Sigma_{\rm HI})^{1/2}$. To achieve the measured velocities, we would need to increase the surface densities by a factor of at least four. This increase would also be mass-dependent, with the more massive galaxies requiring much greater surface densities. However, this does not agree with observations of HI in dwarf galaxies – many surveys have found that there exists a tight relationship between the HI mass and effective radius (Broeils & Rhee, 1997; Lelli et al., 2016). This implies a constant HI surface density. To be consistent with these observations, a constant normalization increase would need to be applied. This would only shift the points upward in Figure 5.2 but would not change the shape of the relationship. Thus, either the lowest mass galaxies would have overpredicted velocities or the highest mass galaxies would have underpredicted velocities.

In conclusion, I find a discrepancy between the predicted maximum circular velocities from EG and the measured maximum circular velocities around isolated dwarf galaxies for the most realistic mass distributions. We need rotation curves of these galaxies to identify if this discrepancy is due to modeling errors or the inability of EG to describe these systems. Given that EG is only equipped to handle systems of this type, it seems that these discrepancies should be taken seriously as a possible issue with the theory. The next step is to obtain rotation curves of these isolated dwarf galaxies. The framework provided in this chapter should allow for a robust test of EG with these rotation curves. This would provide the best test of EG at this time.

Appendix

Appendix 5.A Derivations of the EG Equations for a Deprojected Sérsic Profile

5.A.1 The Sérsic Profile

First, I repeat the equation describing the Sérsic profile

$$I(R) = I_e \exp\left[1 - b_n \left(\frac{R}{R_e}\right)^{1/n}\right] , \tag{5.10}$$

where b_n is defined by $\Gamma(2n) = 2\gamma(2n, b_n)$.

Note that $I(R)$ and R are *projected* quantities. They do not give the 3D, physical radius or intensity. To find the physical luminosity (and then the physical mass), we must deproject the Sérsic profile.

I begin by relating the intensity, $I(R)$, to the luminosity density, $n(r)$,

$$I(R) = 2\int_0^{\infty} dz\ n(r) , \tag{5.11}$$

where I assume the luminosity density is symmetric in z. Note that r is the radius in spherical coordinates and R is the projected radius (i.e. the radius in cylindrical coordinates). Now, we can change variables using $r^2 = R^2 + z^2$. This gives

$$I(R) = 2\int_R^{\infty} \frac{rn(r)}{\sqrt{r^2 - R^2}}\ dr . \tag{5.12}$$

I find $n(r)$ by inverting Equation 5.12 using the Abel Identity (cf. Appendix B.5 of Binney & Tremaine, 2008)

$$n(r) = -\frac{1}{\pi}\int_r^\infty \frac{dI}{dR}\frac{dR}{\sqrt{R^2 - r^2}} \tag{5.13}$$

This is unsolvable for generic $I(R)$. However, the analytic solution to this integral for the $I(R)$ given in Equation 5.10 can be expressed in terms of Meijer G functions (Mazure & Capelato, 2002).

5.A.2 The Meijer G functions

The Meijer G functions (see `http://functions.wolfram.com/HypergeometricFunctions/MeijerG/` and `http://dlmf.nist.gov/16` for more formulae involving the Meijer G functions) are generalized hypergeometric functions that give most of the special functions we know (i.e. trigonometric functions, Bessel functions, exponential function, etc.) as special cases. The Standard Meijer G function is defined as

$$G^{m,n}_{p,q}\left(z \,\middle|\, \begin{array}{c} a_1, \ldots, a_p \\ \\ b_1, \ldots, b_q \end{array} \right) = \frac{1}{2\pi i}\int_L \frac{\left(\prod_{k=1}^{m}\Gamma(s+b_k)\right)\prod_{k=1}^{n}\Gamma(1-a_k-s)}{\left(\prod_{k=n+1}^{p}\Gamma(s+a_k)\right)\prod_{k=m+1}^{q}\Gamma(1-b_k-s)} z^{-s} ds \tag{5.14}$$

A few useful identities of the Meijer G functions are [from DLMF]

$$G_{p,q}^{m,n}\left(z\,\middle|\,\begin{matrix}a_1,\ldots,a_p\\ \\ b_1,\ldots,b_q\end{matrix}\right) \equiv z^{-c}G_{p,q}^{m,n}\left(z\,\middle|\,\begin{matrix}a_1+c,\ldots,a_p+c\\ \\ b_1+c,\ldots,b_q+c\end{matrix}\right) \tag{5.15}$$

$$G_{p,q}^{m,n}\left(\frac{1}{z}\,\middle|\,\begin{matrix}a_1,\ldots,a_p\\ \\ b_1,\ldots,b_q\end{matrix}\right) \equiv G_{q,p}^{n,m}\left(z\,\middle|\,\begin{matrix}1-b_1,\ldots,1-b_q\\ \\ 1-a_1,\ldots,1-a_p\end{matrix}\right) \tag{5.16}$$

$$G_{p,q}^{m,n}\left(z\,\middle|\,\begin{matrix}a_1,\ldots,a_p\\ \\ b_1,\ldots,b_q\end{matrix}\right) \equiv G_{p+1,q+1}^{m,n+1}\left(z\,\middle|\,\begin{matrix}a_0,a_1,\ldots,a_p\\ \\ b_1,\ldots,b_q,a_0\end{matrix}\right) \tag{5.17}$$

The derivative of the Meijer G function leads to another Meijer G function [from Wolfram Functions]

$$\frac{\partial G_{p,q}^{m,n}\left(z\,\middle|\,\begin{matrix}a_1,\ldots,a_p\\ \\ b_1,\ldots,b_q\end{matrix}\right)}{\partial z} = G_{p+1,q+1}^{m,n+1}\left(z\,\middle|\,\begin{matrix}-1,a_1-1,\ldots,a_n-1,a_{n+1}-1,\ldots,a_p-1\\ \\ b_1-1,b_m-1,0,b_{m+1}-1,\ldots,b_q-1\end{matrix}\right) \tag{5.18}$$

By combining Equations 5.18 & 5.15, I find the following useful formula

$$\frac{\partial\left(z^{1-a_1}G_{p,q}^{m,n}\left(z\,\middle|\,\begin{matrix}a_1,\ldots,a_p\\ \\ b_1,\ldots,b_q\end{matrix}\right)\right)}{\partial z} = z^{-a_1}G_{p,q}^{m,n}\left(z\,\middle|\,\begin{matrix}a_1-1,a_2,\ldots,a_p\\ \\ b_1,\ldots,b_q\end{matrix}\right) \ . \tag{5.19}$$

By differentiating the left side of Equation 5.19, I find

$$\begin{aligned} z\frac{\partial}{\partial z}G_{p,q}^{m,n}\left(z\,\middle|\,\begin{matrix}a_1,\ldots,a_p\\ \\ b_1,\ldots,b_q\end{matrix}\right) &= G_{p,q}^{m,n}\left(z\,\middle|\,\begin{matrix}a_1-1,a_2,\ldots,a_p\\ \\ b_1,\ldots,b_q\end{matrix}\right) \\ &+ (a_1-1)G_{p,q}^{m,n}\left(z\,\middle|\,\begin{matrix}a_1,\ldots,a_p\\ \\ b_1,\ldots,b_q\end{matrix}\right) \ . \end{aligned} \tag{5.20}$$

5.A.3 The Radial Mass Profile

Here I will give the radial mass profile for a generic Sérsic profile following the treatment of Mazure & Capelato (2002). This is easily modified to give either the stellar or HI mass profiles using the correct n, R_e, and Σ.

Define the Sérsic profile in terms of dimensionless quantities

$$x \equiv \frac{r}{R_e} \tag{5.21}$$

$$s \equiv \frac{r}{R_e} \tag{5.22}$$

$$i(x) = \frac{I(R)}{I_e} = \exp[-b_n(x^{1/n}-1)] \tag{5.23}$$

$$\nu(s) = n(r)\frac{R_e}{I_e} = -\frac{1}{\pi}\int_s^\infty \frac{di}{dx}\frac{1}{\sqrt{x^2-s^2}}dx \ . \tag{5.24}$$

Then, the deprojected radial luminosity profile is given by

$$L(s) = 4\pi \int_0^s s'^2 \nu(s') ds' \; . \tag{5.25}$$

Since I am assuming that the mass follows the light, the radial mass profile is Equation 5.25 times the mass-to-light ratio, Υ,

$$M(s) = 4\pi\Upsilon \int_0^s s'^2 \nu(s') ds' \; . \tag{5.26}$$

Mazure & Capelato (2002) find that the analytic solution to this integral for a Sérsic profile is

$$M(s) = 2\pi\Upsilon c_1 s^{\frac{2n+1}{n}} G^{2n,1}_{1,2n+1}\left(c_2 s^2 \,\middle|\, \begin{array}{cc} \{-\left(\frac{1}{2n}\right)\}, & \{\} \\ \\ \{\beta_s\}, & \{-\left(\frac{2n+1}{2n}\right)\} \end{array} \right) \; , \tag{5.27}$$

where

$$c_1 \equiv \frac{b_n \exp[b_n]}{(2\pi)^n \sqrt{n}} \tag{5.28}$$

$$c_2 \equiv \left(\frac{b_n}{2n}\right)^{2n} \tag{5.29}$$

$$\beta_s \equiv \left\{ \left(\frac{j-1}{2n}\right)_{1\leq j\leq n} ; \left(\frac{j-2}{2n}\right)_{n+1\leq j\leq 2n} \right\} \; . \tag{5.30}$$

5.A.4 EG Predictions

To give values predicted by EG, I must find $\frac{dM}{dr}$. First, I differentiate Equation 5.27 using Equation 5.20, which gives

$$\frac{dM}{ds} = 4\pi\Upsilon c_1 s^{\frac{n+1}{n}} G^{2n,0}_{0,2n}\left(c_2 s^2 \middle| \begin{matrix} \{\} & \{\} \\ \\ \{\beta_s\} & \{\} \end{matrix} \right). \tag{5.31}$$

Now, I need to express dM/ds and $M(s)$ in terms of r instead. This is done using the definition for s given in Equation 5.21 and accounting for the extra factor of $1/R_e$ from the change of variable in the derivative. However, I also need to account for how I began with a *dimensionless* luminosity density by multiplying both dM/ds and $M(s)$ by $I_e R_e^2$. Then,

$$\begin{aligned}
M(r) &= 2\pi c_1 \Sigma R_e^2 \left(\frac{r}{R_e}\right)^{\frac{2n+1}{n}} G^{2n,1}_{1,2n+1}\left(c_2 \left(\frac{r}{R_e}\right)^2 \middle| \begin{matrix} \{-\left(\frac{1}{2n}\right)\}, & \{\} \\ \\ \{\beta_s\}, & \{-\left(\frac{2n+1}{2n}\right)\} \end{matrix} \right), \\
\frac{dM}{dr} &= 4\pi c_1 \Sigma R_e \left(\frac{r}{R_e}\right)^{\frac{n+1}{n}} G^{2n,0}_{0,2n}\left(c_2 \left(\frac{r}{R_e}\right)^2 \middle| \begin{matrix} \{\} & \{\} \\ \\ \{\beta_s\} & \{\} \end{matrix} \right), \\
M_D^2(r) &= \frac{\pi a_0 c_1 \Sigma R_e^2}{3G} \left(\frac{r}{R_e}\right)^{\frac{2n+1}{n}} r^2 \Bigg[G^{2n,1}_{1,2n+1}\left(c_2 \left(\frac{r}{Re}\right)^2 \middle| \begin{matrix} \{-\left(\frac{1}{2n}\right)\}, & \{\} \\ \\ \{\beta_s\}, & \{-\left(\frac{2n+1}{2n}\right)\} \end{matrix} \right) \\
&+ 2G^{2n,0}_{0,2n}\left(c_2 \left(\frac{r}{Re}\right)^2 \middle| \begin{matrix} \{\} & \{\} \\ \\ \{\beta_s\} & \{\} \end{matrix} \right) \Bigg],
\end{aligned}$$

where $\Sigma = I_e \Upsilon$.

Chapter 6

Baryon Acoustic Oscillations & General Modified Gravity Theories of Dark Matter

In Chapter 5, I discuss one particular type of modified gravity theory that attempts to explain dark matter. This is just one of many, wildly different theories, which are difficult to test in bulk. However, almost all of these theories specify a different gravitational force law that uniquely depends on the baryon and photon density fields. If we can directly measure how the baryon and photon density fields evolve with time, then we can calculate the predicted signal from these theories.

Cold dark matter (CDM) accurately explains how structure forms from initial density perturbations and how these perturbations are imprinted in the cosmic microwave background (CMB; Lifshitz, 1946; Peebles & Yu, 1970; Sunyaev & Zeldovich, 1970; Bond & Efstathiou, 1984). In short, CDM forms potential wells early in the Universe's history. Baryons attempt to fall into these potential wells and are then pushed out by the radiation, to which the baryons are coupled. This causes sound waves to form in the baryon and radiation structure. These baryon acoustic oscillations (BAO) are seen as oscillations in the CMB and in large-scale structure at low redshift. After recombination, the baryons are allowed to fall toward the CMB potential wells, eventually forming galaxies and clusters. Any modified gravity theory for dark matter must also explain this evolution.

In this chapter, here outline how to determine the infrared (IR; i.e., low-energy) behavior of any theory that does not have dark matter based on linking the baryon density field at recombination ($z \sim 1100$) to the baryon power spectrum at low redshift ($z \sim 0$). Any successful theory for dark matter must properly explain how the baryon density field at $z \sim 1100$ evolves to the one at $z \sim 0$. These density fields are typically probed indirectly through fitting the CMB power spectra and the matter power spectrum in tandem (e.g., Spergel et al., 2003; Planck Collaboration et al., 2018). This necessarily assumes ΛCDM (or some simple extension) as well as general relativity (GR). The test we propose here does not invoke GR nor a specific cosmology. Instead it relies solely on small-scale physics – Thomson scattering and the Newtonian continuity equation. Note that while similar tests have been proposed before (McGaugh, 2004; Dodelson, 2011), they have not been explicitly laid out or calculated for general modified gravity theories.

The polarization of the CMB on small scales is exclusively due to Thomson scattering, which itself only relies on the velocities of the electrons. Because protons and electrons are tightly coupled via Coulomb scattering at early times, we can assume that the velocities of the electrons exactly equals that of the protons. The CMB polarization spectrum then directly measures the velocity of the baryons at $z \sim 1100$. The Newtonian continuity equation relates the velocities of the baryons to their density field and is valid at small scales. Thus, the CMB polarization spectrum is a direct measurement of the small-scale baryon density field at $z \sim 1100$. At $z \sim 0$, the galaxy-galaxy correlation function traces the baryon density field at large scales. With these two direct measures of the baryon density field, it is straightforward to then define the form an alternate theory of dark matter must take in the IR. We will combine observations of the CMB and the galaxy power spectrum at low-redshift to determine the required Green's function of structure formation between these redshifts for these alternate theories. This Green's function has a distinctive form as it must suppress the baryon acoustic oscillations by nearly an order of magnitude, as well as greatly increase power on small scales.

Our chapter is organized as follows: Section 6.1 describes our theoretical framework for this test; Section 6.2 describes the data we use for our test; Section 6.3 gives our preliminary results and discusses our planned future work.

6.1 Theory

In this section, we describe the theoretical framework for determining the IR behavior of modified gravity theories for dark matter. We first outline the steps for finding the baryon power spectrum at both $z \sim 1100$ and $z \sim 0$. We then show how to use these both to define the IR behavior.

6.1.1 The Baryon Power Spectrum at $z \sim 1100$

The polarization of the CMB can be related to the velocity of the baryons as (Zaldarriaga & Harari, 1995):

$$\Delta_p(\hat{n}, \vec{x}) = Q(\hat{n}) + iU(\hat{n}) \approx 0.17 \Delta\tau_* \hat{m}^i \hat{m}^j \partial_i v_j \tag{6.1}$$

where Δ_p is the polarization fluctuation, Q and U are Stokes parameters, $\hat{n}$ is the direction of observation (i.e. into the sky), $\Delta\tau_*$ is the width of the last scattering surface, $\hat{m}$ is a 2D unit vector on the plane of the sky, and v is the baryon velocity on the sky[1].

As an example to gain more intuition, let $\hat{m} = \hat{x} + i\hat{y}$ and consider $\hat{n} = \hat{z}$. Then:

$$Q(\hat{n}) + iU(\hat{n}) \approx 0.17\Delta\tau_* \left[(\partial_x v_x - \partial_y v_y) + i(\partial_x v_y + \partial_y v_x)\right] \ . \tag{6.2}$$

In other words, $Q \propto \nabla \cdot v$ and $U \propto \nabla \times v$. Note that the velocity due to density perturbations is *irrotational*, which implies that $U = 0$. However, this is only for one particular direction (along the $\hat{z}$-axis). In general, we must consider all directions on the sky and there will be both Q and U polarization.

Now consider the small-angle approximation. Here we specify that all wavevectors, $\vec{k}$, are close to our $\hat{n}$. In Fourier space, this gives the equation:

$$\Delta_p(\hat{n}, \vec{k}) \approx 0.17\Delta\tau_* ikv_b \ , \tag{6.3}$$

where $k = |\vec{k}|$. Then, the polarization power spectrum on small scales is:

$$\langle \Delta_p(\hat{n}, \vec{k}) \Delta_p^*(\hat{n}, \vec{k}) \rangle \approx (0.17)^2 \Delta\tau_*^2 k^2 v_b^2 \tag{6.4}$$

Typically, polarization results are reported using E and B-modes, which are just a rotation of the Q-U basis. This basis is specifically chosen such that there are no B-modes on small scales in the early Universe – instead all of the polarization is given by E-modes. Thus, the polarization power spectrum is just the E-mode power spectrum[2]:

$$P_{EE}(k) \approx (0.17\Delta\tau_*)^2 k^2 v_b^2(k) \tag{6.5}$$

---

[1] Note that the dipole moment of the CMB temperature gives us the final component of the velocity, v_r.

[2] Note that there is an extra term related to fixing the basis for the E-B decomposition. However, this should be ~ 1 under the small-angle approximation.

Now we must connect this equation to the baryon density power spectrum. The continuity equation is a natural choice. At small scales, we can ignore any changes in the potential and simply treat the baryon-photon fluid as a normal Newtonian fluid. Then the continuity equation in Fourier space is:

$$\dot{\delta}_b(k) + ikv_b(k) = 0 \ , \tag{6.6}$$

where $\dot{} \equiv \frac{d}{d\tau}$ (conformal time).

We can simplify this equation by considering $\dot{\delta}_b(k)$ further. All linear modes evolve independently, thus we can parameterize $\delta(k,\tau) = \delta_b(k, \tau = \tau_*)D(\tau)$, where $D(\tau)$ is the growth function and we set $D(\tau = \tau_*) = 1$. Then:

$$\dot{\delta}_b(k) = \delta_b(k, \tau = \tau_*)\frac{dD(\tau)}{d\tau} = \delta_b(k,\tau) f_* H_* \ , \tag{6.7}$$

where f_* is the growth factor and H_* is the Hubble factor normalized such that they are both unity at τ_*.

Equating our two expressions for $\dot{\delta}_b(k,\tau)$ then gives an equation for the baryon density in terms of the velocity:

$$\delta_b(k,\tau) = \frac{-ikv_b(k,\tau)}{f_* H_*} \tag{6.8}$$

With this formalism, the baryon density power spectrum is:

$$P_{bb}(k, z \sim 1100) = \frac{k^2 v_b^2(k,\tau)}{f_*^2 H_*^2} \ . \tag{6.9}$$

Finally, we can equate this to the EE power spectrum using Equation 6.5:

$$P_{bb}(k, z \sim 1100) = \frac{P_{EE}(k)}{(0.17\Delta\tau_*)^2 f_*^2 H_*^2} \ . \tag{6.10}$$

In other words, the baryon power spectrum at $z \sim 1100$ is, up to a normalization factor, equal to the EE power spectrum.

6.1.2 The Baryon Power Spectrum at $z \sim 0$

The baryon power spectrum at $z \sim 0$ is more straightforward to deduce. The baryons at low redshift and large scales ($\gtrsim$ 10 Mpc) are well-traced by the galaxies. Thus, we can take the 3D power spectrum of galaxies as the baryon power spectrum. This is given by:

$$P_{bb}(k, z \sim 0) = b_{bg}^2 P_{gg}(k, z \sim 0) \, , \tag{6.11}$$

where b_{bg} is the bias of baryons relative to galaxies and P_{gg} is the 3D galaxy-galaxy power spectrum.

To find the galaxy-galaxy power spectrum, we measure the correlation function, $\xi(\vec{\theta})$ – this is just the Fourier transform of the 2D power spectrum. This must then be de-projected using the window function appropriate for the particular galaxy survey (see, e.g., Dodelson, 2003).

In reality, the galaxies are a biased tracer of the baryons. Most of the baryonic mass in the universe is in gas (de Graaff et al., 2019). However, we expect that for $k < 0.1$ Mpc^{-1} the bias, b_{bg}, approaches 1. This is seen in numerical simulations (e.g., Springel et al., 2018), and violating this would require moving baryons large distances. Thus, the galaxy-galaxy power spectrum should be a good measure of the baryonic power spectrum at these large scales.

6.1.3 Infrared Behavior of Modified Gravity

We now have the baryon power spectrum at $z = 1100$ and $z \sim 0$ from directly measurable quantities. Our goal is to use both to determine the necessary IR behavior of modified gravity theories. We use the formalism of the transfer function for this purpose.

In the absence of CDM, the cosmological evolution of large-scale structure is simple. We observe the large-scale distribution of baryons at $z \sim 1100$ and at $z \sim 0.3$. Any successful theory for dark matter must explain how the universe evolved between these two redshifts. Since the fluctuations on large scales are small, we expect that the theory will be perturbative and we can describe the growth of fluctuations by a linear transfer function.

In ΛCDM, baryons fall into the dark matter potentials. This imprints the large-scale distribution of the dark matter on the baryons. Thus, the transfer function of CDM, along with the initial spectrum of fluctuations, is all that is needed to accurately describe the matter power spectrum. The baryon power spectrum follows directly by using the CDM potential created by the evolution of these perturbations. However, if we no longer have CDM in our model, the baryon transfer function itself must encode all of this information. *In modified gravity theories of dark matter, the baryon transfer function must account for all of the changes in the baryon perturbations from early to late times.*

The matter power spectrum depends on the transfer function as: $P(k) \propto P_\phi(k)T^2(k)$, where P_ϕ is the primordial spectrum of perturbations. In analogy to this, we can define the transfer function:

$$\hat{T}_b^2(k) = \frac{P_{bb}(k, z \sim 0)}{P_{bb}(k, z = 1100)} \ . \tag{6.12}$$

$\hat{T}_b^2(k)$ describes how the baryon perturbations evolve from $z = 1100$ to $z \sim 0$. We use the hat here indicate this is different from the normal transfer function.

Any theory for dark matter must adequately explain both the shape and normalization of $\hat{T}_b^2(k)$. Our transfer function can be exactly represented with measurable data and does not rely on any assumptions about underlying theories, outside of the small-scale physics described above. It is also possible to find the theoretical solutions for any well-formed dark matter or modified gravity theories[3]. In this chapter, we will focus solely on the shape of $\hat{T}_b^2(k)$ – a more precise analysis is required to use the normalization as well.

As a way of building intuition, we will also consider the Fourier pair of the transfer function – the Green's function:

$$\hat{\mathcal{G}}_b(r) = G_0 \int dk \, \frac{k^2}{2\pi^2} \hat{T}_b(k) j_0(kr) \; , \tag{6.13}$$

where G_0 is a normalization term that we arbitrarily set such that $\hat{\mathcal{G}}(r=0) = 1$. This functions shows, in real space, how the perturbations evolve between these two redshifts.

6.2 Data

We require two main pieces of data: the EE power spectrum from the CMB and the galaxy-galaxy 3D power spectrum at low redshift. We describe how we obtain each of these and our modifications to the data below.

For the EE power spectrum, we use the Planck 2018 angular power spectrum (Planck Collaboration et al., 2019a). The data is given as multipoles, C_l^{EE}, of the 2D power spectrum. We must convert this to the 3D power spectrum, $P_{EE}(k)$. We approximate $l = k\eta_*$, where η_* is the conformal distance to the last scattering surface[4]

---

[3] We take "well-formed" to mean that a theory has a cosmology associated with it that allows for the evolution of initial perturbations to today.

[4] Note, that this does require setting a cosmology. We use the Planck Collaboration et al. (2018) measured distance to the last scattering surface. In principle, it may be possible to set η_* without setting a cosmology – instead, we might be able to use the alignment of the peaks in each of the power spectra. We leave this issue to future work.

Then, to order unity, the 3D power spectrum is (Bond & Efstathiou, 1984):

$$P_{EE}(k) \sim \frac{(2\pi)^3\eta_*^2}{k} C_{l=k\eta_*}^{EE} \, . \tag{6.14}$$

We bin the C_l^{EE} data into 50 l-bins to increase the signal-to-noise. We also only use $l < 1200$, due to the high noise seen in the data above this point.

We use the data from Beutler et al. (2016) for the galaxy-galaxy power spectrum at low-z. Beutler et al. (2016) measures the BAO signal from galaxies in from $z = 0.2 - 0.75$ using the Sloan Digital Sky Survey-III (SDSS-III; Eisenstein et al., 2011) Baryon Oscillation Spectroscopic Survey (BOSS) DR12 data set (Dawson et al., 2013; Alam et al., 2015). As part of this measurement, they also calculate the 3D galaxy-galaxy power spectrum in 3 different redshift bins. We use the lowest redshift bin, $z = 0.2 - 0.5$, which has an effective redshift of $z = 0.38$. The galaxy-galaxy 3D power spectrum is calculated from the correlation function, as explained briefly in Section 6.1.2. This is measured from $k = 0.016 - 0.15$ h Mpc^{-1}. We use their fiducial value of $h = 0.676$ to transform to physical units.

When the 3D power spectrum is measured, it is typically decomposed into multipoles:

$$P_l(k) = \sum_l P(k)\mathcal{L}_l(k) \, , \tag{6.15}$$

where $\mathcal{L}_l(k)$ are the Legendre polynomials. We here consider just the monopole, $l = 0$ moment of the power spectrum, which is the angle-averaged power spectrum. This effectively removes ‘fingers of god’ and other non-linear effects.

We only use the data from each survey where they both overlap in k. This range, $k = 0.01 - 0.126$ h Mpc^{-1}, corresponds to small scales (i.e. much smaller than the horizon) today and at recombination.

In Figure 6.1, we show the baryon power spectrum at $z = 1100$ and $z = 0.38$. As can be seen, the proper dark matter theory must somehow explain how the $z = 1100$

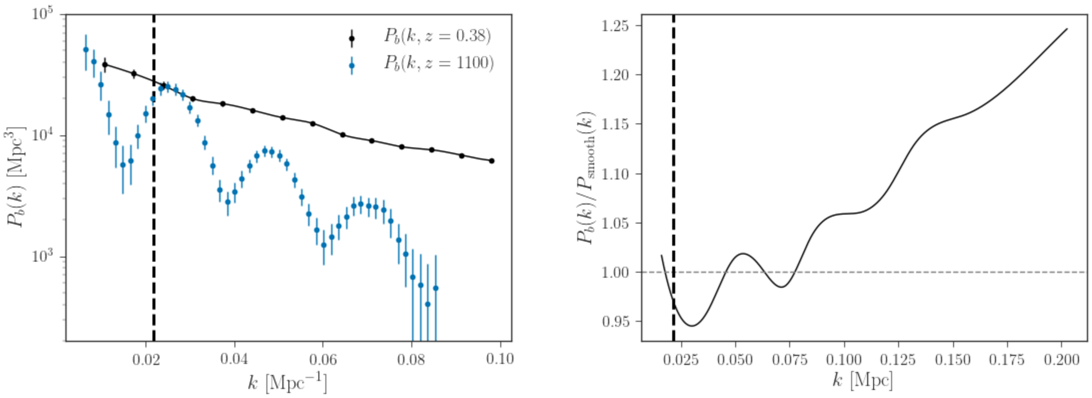

Figure 6.1: *Left:* Baryon power spectra at $z = 0.38$ (black) and $z = 1100$ (blue). The low-redshift power spectrum is derived from Beutler et al. (2016). The high-redshift power spectrum is derived from the Planck Collaboration et al. (2019a) EE power spectrum using Equation 6.10. The black, dashed line gives the acoustic scale, as given by Planck Collaboration et al. (2018). *Right:* The baryon power spectrum at $z = 0.38$ normalized by the smoothed power spectrum, as given by the no-wiggle form in Eisenstein & Hu (1998). This emphasizes the BAO signal in the low-redshift spectrum and it roughly agrees with previous simulations work (Seo et al., 2008). Note that the k-range in this panel is larger than in the left panel.

spectrum smooths out and increases in power on small scales. Note that the BAO 'wiggles' in the low-redshift power spectrum look much weaker than those in the CMB-derived spectrum. This is just due to the normal evolution of perturbations over time. Some authors plot the BAO spectrum in a way that emphasizes the wiggles (see, for example, Seo et al., 2008) by dividing out the 'smooth' power spectrum. We show this in the right panel of Figure 6.1, where we use the no-wiggle form of the transfer function given by Eisenstein & Hu (1998).

We also indicate the acoustic scale as the dashed, black line on all plots in this chapter. We use the (Planck Collaboration et al., 2018) value for θ_* to set the angular scale of the sound horizon. We then convert this to an l value via $l_* = \pi/\theta_*$. Finally, we obtain the k value using $k_* = l_*/\eta_*$.

6.3 Results & Discussion

Our transfer function is shown in Figure 6.2. This makes the exact evolution of perturbations needed apparent. Power should grow the most on small scales. This aligns with the standard CDM picture.

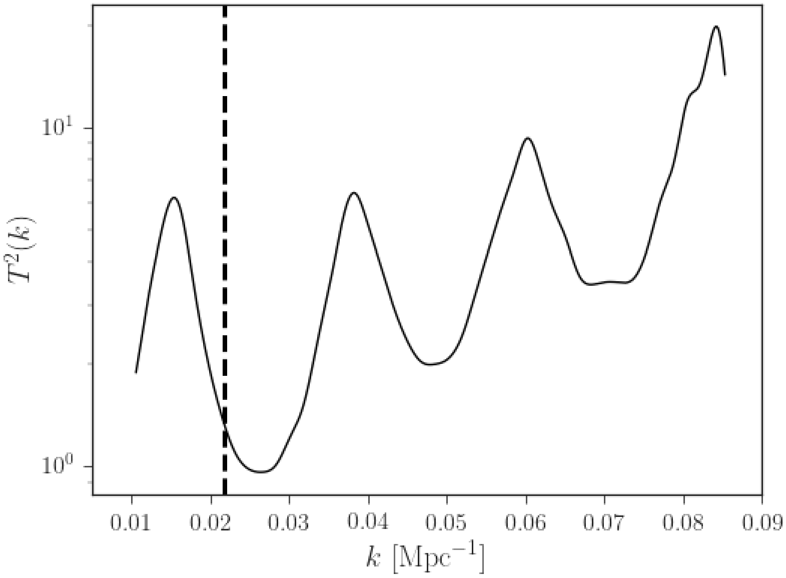

Figure 6.2: Baryon transfer function from $z = 1100$ to $z = 0.38$. This shows how the baryons perturbations must evolve. Any dark matter theory must reproduce this transfer function.

We show the associated Green's function in Figure 6.3. This shows, in physical space, how the matter must move between these two redshifts. Namely, we expect extra matter at centrally peaked positions. This is exactly the effect we expect from CDM. Note that the exact form of the Green's function depends heavily on the behavior of the transfer function at high-k. We cannot directly probe this with our current data and so we try a few different assumptions: 1) $T^2(k > k_{\rm max}) = 0$ (black line); 2) $T^2(k > k_{\rm max}) = T^2(k_{\rm max})$ (blue, solid line); 3) $T^2(k > k_{\rm max}) > T^2(k_{\rm max})$, with a cubic spline fit used to find the form (blue, dashed line). These assumptions mostly change the height and phase of the secondary peaks in the Green's function.

Regardless of the form at high-k, the Green's function shows oscillations near the BAO scale. Thus, any alternative gravity theory would need to contain this scale to suppress the BAO features over time – changing them from dominant at $z \sim 1100$ to very low amplitude at $z \sim 0.4$.

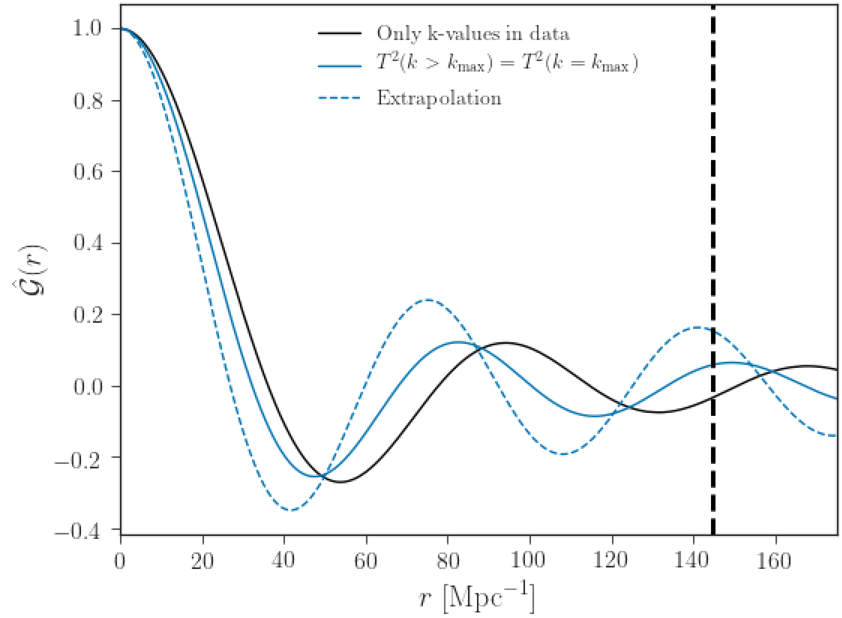

Figure 6.3: Green's function for the transfer function in Figure 6.2. This shows, in real space, where the extra mass must be located to produce the correct perturbations at $z = 0.38$. Note that the shape here depends on the assumed shape of the transfer functions at $k \gtrsim 0.1$ Mpc^{-1}. The black line shows the results when we set this range to 0. The blue line gives the results if we set $T^2(k > k_{\rm max}) = T^2(k = k_{\rm max})$. The dashed, blue line shows the results if we use a cubic spline fit to extrapolate the transfer function – this assumes that the transfer function continues to increase at higher k.

We can go one step further here. First, consider the momentum equation:

$$\dot{v} + \frac{\dot{R}}{R} v = a \; , \tag{6.16}$$

where R is the scale factor and a is the acceleration. Taking the time derivative of Equation 6.6, the divergence of Equation 6.16, and combining we find:

$$a = \frac{i\ddot{\delta}}{k} - \frac{\dot{R}}{R}v \ . \tag{6.17}$$

In GR, $ika = k^2\Psi$, where Ψ is the Newtonian potential. This produces the equation $\ddot{\delta} + ik\frac{\dot{R}}{R}v = -k^2\Psi = 4\pi G\rho$.

If a modified gravity theory is just a linear modification of GR, then we can write the acceleration as:

$$a = F(k)a_{\mathrm{GR}} = -ikF(k)\Phi = -ikF(k)T_{\mathrm{GR}}(k)D(t)\Phi_p(k) \ \ , \tag{6.18}$$

where $F(k)$ is the modification to GR, T_{GR} is the GR transfer function, $D(t)$ encodes all of the time dependence, and $\Phi_p(k)$ is the primordial potential (again, assuming GR).

In other words, if we measure the transfer function accurately, we get:

$$T(k) = F(k)T_{\mathrm{GR}}(k) \ . \tag{6.19}$$

Thus, if we can accurately measure the transfer function, we can determine the form the acceleration equation of a modified gravity theory must take.

Any local modified gravity theory *must* satisfy the constraint we have laid out in this chapter. However, it is possible for nonlinear theories to evade this test – we assumed that modes were independent. A more general version of this test would include mode-mixing. Namely, the transfer function would be:

$$P_{bb}(k, z \sim 0.3) = \int dk' P_{bb}(k', z = 1100)T^2(k, k') \ . \tag{6.20}$$

We can also consider this in terms of the acceleration picture we discuss above. It must be linear to first order since we see that fluctuations on large scales (and at early times) are linear. If we make the further assumption that the acceleration at $\delta = 0$ is $a = 0$, then, to second-order the acceleration relation must be:

$$a(k) = f_1(k)\delta(k) + \int f_2(k, k')\delta(k)\delta(k')dk' \; . \tag{6.21}$$

From the Equation 6.18, we see that F can act as a either a transfer function or as a modification to the primordial spectrum. Thus, $f_2(k, k')$ can be constrained by limits on primordial non-Gaussianity.

However, this would be subject to the constraints on primordial non-Gaussianity. The best current constraints on local non-Gaussianity are $f_{\mathrm{NL}}^{\mathrm{local}} = -0.9 \pm 5.1$ (Planck Collaboration et al., 2019b), where f_{NL} is defined as:

$$\delta(\vec{k}) = \delta_G(\vec{k}) + \frac{3}{5} f_{\mathrm{NL}} \frac{1}{(2\pi)^3} \int d^3\vec{k}' \delta(\vec{k})\delta(\vec{k}') \tag{6.22}$$

There is also a low-redshift constraint on f_{NL} using a combination of large-scale structure data (mostly galaxy surveys) of $-29 < f_{\mathrm{NL}} < 70$ (Slosar et al., 2008). We defer further discussion of these issues to future work.

Two popular theories of modified gravity, modified Newtonian dynamics (MOND; Milgrom, 1983) and Emergent Gravity (Verlinde, 2017), do not seem to have forms suitable for the Green's function we show here. While neither of these theories have actual cosmologies associated with them, their Newtonian forms at large scales do not seem promising. The accelerations in both theories scale as $\sim \sqrt{GM}/R$. This would then predict a power-law Green's function: nothing like what is needed to fit the cosmological observations noted in this chapter. In particular, neither predict a special scale at the BAO scale. Perhaps, mode-mixing at early times could allow for this to be remedied (McGaugh, 2004); however, it is unclear how this could occur while still leading to the $1/R$ force law and not defying primordial non-Gaussianity constraints.

The work in this chapter is preliminary. In the future, we would like to make our calculations more robust, particularly the transformation of the C_l's to a 3D power spectrum. We also hope to make our test totally independent of cosmology by mapping the l's to k's without the use of the distance to last scattering. Finally, we would like to develop the acceleration picture further, particularly with respect to using the primordial non-Gaussianity constraints to place limits on nonlinear theories. In fact, it might be possible to show that a nonlinear theory that produces the BAO feature at the correct scale is incompatible with current non-Gaussianity constraints.

In this chapter, we outline the steps needed to test modified gravity theories using the baryon power spectra at $z \sim 1100$ and $z \sim 0.4$. We found the high-redshift power spectrum by using the CMB EE polarization spectrum, as measured by Planck Collaboration et al. (2019a). We take our low-redshift power spectrum from the SDSS BOSS galaxy power spectrum results (Beutler et al., 2016). We find that whatever modified gravity theory for dark matter that takes us from $z \sim 1100$ to $z \sim 0.4$ must have a very peculiar and specific form, as illustrated by the transfer function in Figure 6.2. This work is preliminary, but we think it shows promise for determining the necessary IR behavior of modified gravity theories without dark matter.

Chapter 7

Conclusion

This dissertation contributes some ways we can use gravitational waves to test theories of gravity and black hole dynamics, and some tests of dark matter theories. Hopefully, the tests outlined here will be useful as we continue to gather more data on our universe. In summary, here are the main takeaways from each chapter:

- Chapter 2: The agreement between the distances derived from gravitational waves and electromagnetic waves to GW170817 show that we do not live in extra spatial dimensions – or at least, if we do, then they must be very small or behave just like 3+1 dimensions until very large scales. We also know that the graviton must have a lifetime greater than $\sim$ 500 Myr.

- Chapter 3: We found a binary supermassive black hole system and we use it to predict that we should observe the gravitational wave background within a decade. If we do not see the signal by that point, then there may be a final parsec problem.

- Chapter 4: Self-interacting dark matter would produce U-shaped warps in disk galaxies. We do not see these warps in the galaxies that should have them, so we can place competitive limits on the strength of dark matter self-interactions.

With more galaxies, we will be able to totally rule out self-interacting dark matter as an interesting candidate for dark matter.

- Chapter 5: Verlinde's Emergent Gravity theory does not properly predict the rotation velocities of isolated dwarf galaxies, which are perfectly suited for testing the theory. The results are not conclusive, but the formalism given in the chapter should allow for conclusive results once enough rotation curves are obtained for these galaxies.

- Chapter 6: We can use both the cosmic microwave background polarization spectrum and the low-redshift galaxy power spectrum to show the form a modified gravity theory must take to explain the evolution of structure in the universe.

What are the interesting next steps? I think there are two avenues that are exciting to pursue after this work: 1) continue to look for more binary supermassive black holes and further develop what a pulsar timing array detection of the gravitational wave background will tell us about supermassive black holes; 2) find more tests of dark matter properties.

For the binary supermassive black hole work, we have already begun this next step. We recently obtained data for many objects like the one featured in Chapter 3. A preliminary analysis seems to show that this is indeed a good method for finding supermassive black hole pairs reliably. Another work I have been involved in shows that several different estimates for the stochastic background, based on supermassive black hole populations, seem to give remarkably similar answers. This is all tentative, but I am excited to see what we can learn about the GWB and what it can teach us about black hole dynamics and supermassive black hole evolution.

The next decade will bring several new survey telescopes (e.g., WFIRST, LSST, and Euclid) that will give us invaluable data on the structure of matter in our galaxy and the universe. How can we best use this data to learn more about dark matter? Can we totally rule out modified gravity theories? Can we confirm any other properties of dark matter? Compelling data for a specific property of dark matter would totally revolutionize our understanding of this mysterious substance, and perhaps lead us closer to its true nature. I am eager to keep working on these tests.

Bibliography

Abbott, B. P., Abbott, R., Abbott, T. D., et al. 2016, Phys. Rev. Lett., 116, 061102

—. 2017a, Nature, 551, 85

—. 2017b, ApJL, 848, L13

—. 2017c, Physical Review Letters, 119, 161101

Adams, J. C. 1846, MNRAS, 7, 149

Agathos, M., Del Pozzo, W., Li, T. G. F., et al. 2014, Phys. Rev. D, 89, 082001

Akerib, D. S., et al. 2017, Phys. Rev. Lett., 118, 021303

Alam, S., Albareti, F. D., Allende Prieto, C., et al. 2015, ApJS, 219, 12

Alexander, D. M., Chary, R. R., Pope, A., et al. 2008, ApJ, 687, 835

Amendola, L., Sawicki, I., Kunz, M., & Saltas, I. D. 2018, J. Cosmology Astropart. Phys., 2018, 030

Andriot, D., & Lucena Gómez, G. 2017, Journal of Cosmology and Astro-Particle Physics, 2017

Aprile, E., et al. 2018, Phys. Rev. Lett., 121, 111302

Arai, S., & Nishizawa, A. 2018, Phys. Rev. D, 97, 104038

Arzoumanian, Z., Brazier, A., Burke-Spolaor, S., et al. 2016, ApJ, 821, 13

Arzoumanian, Z., Baker, P. T., Brazier, A., et al. 2018, ApJ, 859, 47

Baker, T., Bellini, E., Ferreira, P. G., et al. 2017, Physical Review Letters, 119, 251301

Baldauf, T., Desjacques, V., & Seljak, U. 2015, Phys. Rev. D, 92, 123507

Banerjee, A., Adhikari, S., Dalal, N., More, S., & Kravtsov, A. 2019, arXiv e-prints, arXiv:1906.12026

Begelman, M. C., Blandford, R. D., & Rees, M. J. 1980, Nature, 287, 307

Behroozi, P. S., Wechsler, R. H., & Wu, H.-Y. 2013, ApJ, 762, 109

Bekenstein, J. D. 2004, Phys. Rev. D, 70, 083509

Belgacem, E., Dirian, Y., Foffa, S., & Maggiore, M. 2018, Phys. Rev. D, 97, 104066

Berti, E., Barausse, E., Cardoso, V., et al. 2015, Classical and Quantum Gravity, 32, 243001

Beutler, F., Blake, C., Koda, J., et al. 2016, MNRAS, 455, 3230

Biagetti, M., Desjacques, V., Kehagias, A., & Riotto, A. 2014, Phys. Rev. D, 90, 103529

Binney, J. 1992, Annu. Rev. Astron. Astrophys., 30, 51

Binney, J., & Tremaine, S. 2008, Galactic Dynamics: Second Edition (Princeton University Press)

Blanton, M. R., Kazin, E., Muna, D., Weaver, B. A., & Price-Whelan, A. 2011, AJ, 142, 31

Bond, J. R., & Efstathiou, G. 1984, ApJL, 285, L45

Bonetti, M., Sesana, A., Barausse, E., & Haardt, F. 2018, MNRAS, 477, 2599

Boylan-Kolchin, M., Bullock, J. S., & Kaplinghat, M. 2011, MNRAS, 415, L40

Bradford, J. D., Geha, M. C., & Blanton, M. R. 2015, ApJ, 809, 146

Broeils, A. H., & Rhee, M. H. 1997, A&A, 324, 877

Brouwer, M. M., Visser, M. R., Dvornik, A., et al. 2017, MNRAS, 466, 2547

Bullock, J. S., & Boylan-Kolchin, M. 2017, ARA&A, 55, 343

Burke-Spolaor, S., Taylor, S. R., Charisi, M., et al. 2019, A&A Rev., 27, 5

Carrick, J., Turnbull, S. J., Lavaux, G., & Hudson, M. J. 2015, MNRAS, 450, 317

Chen, C.-T. J., Hickox, R. C., Goulding, A. D., et al. 2017, ApJ, 837, 145

Chen, H.-Y., Fishbach, M., & Holz, D. E. 2018a, Nature, 562, 545

Chen, J., Zhang, P., Zheng, Y., Yu, Y., & Jing, Y. 2018b, ApJ, 861, 58

Creminelli, P., & Vernizzi, F. 2017, Phys. Rev. Lett., 119, 251302

Dalal, N., Holz, D. E., Hughes, S. A., & Jain, B. 2006, Phys. Rev. D, 74, 063006

Dawson, K. S., Schlegel, D. J., Ahn, C. P., et al. 2013, AJ, 145, 10

de Graaff, A., Cai, Y.-C., Heymans, C., & Peacock, J. A. 2019, A&A, 624, A48

Deffayet, C., & Menou, K. 2007, ApJL, 668, L143

Dehnen, W. 1993, MNRAS, 265, 250

Desmond, H., Ferreira, P. G., Lavaux, G., & Jasche, J. 2018a, Phys. Rev. D, 98, 083010

—. 2018b, MNRAS, 474, 3152

Dey, L., Gopakumar, A., Valtonen, M., et al. 2019, Universe, 5, 108

Diez-Tejedor, A., Gonzalez-Morales, A. X., & Niz, G. 2018, MNRAS, 477, 1285

Dodelson, S. 2003, Modern cosmology (Academic Press)

—. 2011, International Journal of Modern Physics D, 20, 2749

Dubois, Y., Pichon, C., Welker, C., et al. 2014, MNRAS, 444, 1453

Dvali, G., Gabadadze, G., & Shifman, M. 2001, Physics Letters B, 497, 271

Einstein, A. 1916, Sitzungsberichte der Königlich Preußischen Akademie der Wissenschaften (Berlin), 688

—. 1918, Sitzungsberichte der Königlich Preußischen Akademie der Wissenschaften (Berlin), 154

Eisenstein, D. J., & Hu, W. 1998, ApJ, 496, 605

Eisenstein, D. J., Weinberg, D. H., Agol, E., et al. 2011, AJ, 142, 72

Ettori, S., Ghirardini, V., Eckert, D., Dubath, F., & Pointecouteau, E. 2017, MNRAS, 470, L29

Ezquiaga, J. M., & Zumalacárregui, M. 2017, Physical Review Letters, 119, 251304

Fabbiano, G., Wang, J., Elvis, M., & Risaliti, G. 2011, Nature, 477, 431

Faber, S. M., & Jackson, R. E. 1976, ApJ, 204, 668

Finlez, C., Nagar, N. M., Storchi-Bergmann, T., et al. 2018, MNRAS, 479, 3892

Foreman-Mackey, D., Hogg, D. W., Lang, D., & Goodman, J. 2013, PASP, 125, 306

Fu, H., Yan, L., Myers, A. D., et al. 2012, ApJ, 745, 67

Galle, J. G. 1846, MNRAS, 7, 153

Geha, M., Blanton, M. R., Masjedi, M., & West, A. A. 2006, ApJ, 653, 240

Gnedin, O. Y., & Ostriker, J. P. 2001, ApJ, 561, 61

Gould, A., & Rix, H.-W. 2000, ApJ, 532, L29

Goulding, A. D., Alexander, D. M., Mullaney, J. R., et al. 2011, MNRAS, 411, 1231

Greene, J. E., Pooley, D., Zakamska, N. L., Comerford, J. M., & Sun, A.-L. 2014, ApJ, 788, 54

Grogin, N. A., Kocevski, D. D., Faber, S. M., et al. 2011, ApJS, 197, 35

Guidorzi, C., Margutti, R., Brout, D., et al. 2017, ApJL, 851, L36

Harrison, C. M., Alexander, D. M., Mullaney, J. R., & Swinbank, A. M. 2014, MNRAS, 441, 3306

Harvey, D., Massey, R., Kitching, T., et al. 2013, Mon. Not. R. Astron. Soc., 433, 1517

Hees, A., Famaey, B., & Bertone, G. 2017, Phys. Rev. D, 95, 064019

Hellings, R. W., & Downs, G. S. 1983, ApJL, 265, L39

Hickox, R. C., Mullaney, J. R., Alexander, D. M., et al. 2014, ApJ, 782, 9

Holz, D. E., & Hughes, S. A. 2005, ApJ, 629, 15

Hopkins, P. F., Richards, G. T., & Hernquist, L. 2007, ApJ, 654, 731

Jasche, J., Kitaura, F. S., Wandelt, B. D., & Enßlin, T. A. 2010, MNRAS, 406, 60

Jasche, J., & Lavaux, G. 2015, MNRAS, 447, 1204

Jasche, J., & Lavaux, G. 2019, Astron. Astrophys., 625, A64

Jasche, J., Leclercq, F., & Wandelt, B. D. 2015, J. Cosmology Astropart. Phys., 2015, 036

Jasche, J., & Wandelt, B. D. 2012, MNRAS, 425, 1042

—. 2013, MNRAS, 432, 894

Kahlhoefer, F., Schmidt-Hoberg, K., Frandsen, M. T., & Sarkar, S. 2014, Mon. Not. R. Astron. Soc., 437, 2865

Kauffmann, G., & Heckman, T. M. 2009, MNRAS, 397, 135

Kauffmann, G., Heckman, T. M., Tremonti, C., et al. 2003, MNRAS, 346, 1055

Kelley, L. Z., Blecha, L., Hernquist, L., Sesana, A., & Taylor, S. R. 2017, MNRAS, 471, 4508

Kim, S. Y., Peter, A. H. G., & Hargis, J. R. 2018, Phys. Rev. Lett., 121, 211302

Koss, M. J., Blecha, L., Bernhard, P., et al. 2018, Nature, 563, 214

Kravtsov, A. V., Berlind, A. A., Wechsler, R. H., et al. 2004, ApJ, 609, 35

Kummer, J., Kahlhoefer, F., & Schmidt-Hoberg, K. 2018, Mon. Not. R. Astron. Soc., 474, 388

Laureijs, R., Gondoin, P., Duvet, L., et al. 2012, in Proc. SPIE, Vol. 8442, Space Telescopes and Instrumentation 2012: Optical, Infrared, and Millimeter Wave, 84420T

Lavaux, G., & Hudson, M. J. 2011, MNRAS, 416, 2840

Lavaux, G., & Jasche, J. 2016, MNRAS, 455, 3169

Le Verrier, U. J. 1846a, Astronomische Nachrichten, 25, 85

—. 1846b, Astronomische Nachrichten, 25, 65

—. 1859, Annales de l'Observatoire de Paris, 5, 1

Lehmann, B. V., Mao, Y.-Y., Becker, M. R., Skillman, S. W., & Wechsler, R. H. 2017, ApJ, 834, 37

Lelli, F., McGaugh, S. S., & Schombert, J. M. 2016, AJ, 152, 157

—. 2017, MNRAS, 468, L68

Lifshitz, E. M. 1946, Zhurnal Eksperimentalnoi i Teoreticheskoi Fiziki, 16, 587

Linder, E. V. 2018, J. Cosmology Astropart. Phys., 3, 005

Liu, X., Civano, F., Shen, Y., et al. 2013, ApJ, 762, 110

Liu, X., Greene, J. E., Shen, Y., & Strauss, M. A. 2010, ApJL, 715, L30

Lombriser, L., & Lima, N. A. 2017, Physics Letters B, 765, 382

Lombriser, L., & Taylor, A. 2016, J. Cosmology Astropart. Phys., 3, 031

Loredo, T. J. 2004, in American Institute of Physics Conference Series, Vol. 735, American Institute of Physics Conference Series, ed. R. Fischer, R. Preuss, & U. V. Toussaint, 195–206

Loutrel, N., Yunes, N., & Pretorius, F. 2014, Phys. Rev. D, 90, 104010

LSST Science Collaboration, Abell, P. A., Allison, J., Anderson, S. F., et al. 2009, arXiv e-prints, arXiv:0912.0201

Mandel, I., Farr, W. M., & Gair, J. R. 2019, MNRAS, 486, 1086

Marconi, A., Risaliti, G., Gilli, R., et al. 2004, MNRAS, 351, 169

Markevitch, M., Gonzalez, A. H., Clowe, D., et al. 2004, Astrophys. J., 606, 819

Martinsson, T. P. K., Verheijen, M. A. W., Bershady, M. A., et al. 2016, A&A, 585, A99

Mashchenko, S., Wadsley, J., & Couchman, H. M. P. 2008, Science, 319, 174

Massey, R., Kitching, T., & Nagai, D. 2011, Mon. Not. R. Astron. Soc., 413, 1709

Mazure, A., & Capelato, H. V. 2002, A&A, 383, 384

McGaugh, S. S. 2004, ApJ, 611, 26

McGaugh, S. S., Rubin, V. C., & de Blok, W. J. G. 2001, AJ, 122, 2381

Merloni, A., & Heinz, S. 2008, MNRAS, 388, 1011

Milgrom, M. 1983, ApJ, 270, 365

Mingarelli, C. M. F. 2019, Nature Astronomy, 3, 8

Mingarelli, C. M. F., Lazio, T. J. W., Sesana, A., et al. 2017, Nature Astronomy, 1, 886

Miralda-Escudé, J. 2002, ApJ, 564, 60

Misner, C. W., Thorne, K. S., & Wheeler, J. A. 2017, Gravitation (Princeton University Press)

Mullaney, J. R., Alexander, D. M., Fine, S., et al. 2013, MNRAS, 433, 622

Müller-Sánchez, F., Nevin, R., Comerford, J. M., et al. 2018, Nature, 556, 345

Navarro, J. F., Frenk, C. S., & White, S. D. M. 1997, ApJ, 490, 493

Navarro, J. F., Ludlow, A., Springel, V., et al. 2010, MNRAS, 402, 21

Nersisyan, H., Lima, N. A., & Amendola, L. 2018, ArXiv e-prints, arXiv:1801.06683

Nishizawa, A. 2018, Phys. Rev. D, 97, 104037

Nissanke, S., Holz, D. E., Dalal, N., et al. 2013, ArXiv e-prints, arXiv:1307.2638

Nissanke, S., Holz, D. E., Hughes, S. A., Dalal, N., & Sievers, J. L. 2010, ApJ, 725, 496

Nobili, A. M., & Will, C. M. 1986, Nature, 320, 39

Peebles, P. J. E., & Yu, J. T. 1970, ApJ, 162, 815

Peng, C. Y., Ho, L. C., Impey, C. D., & Rix, H.-W. 2010, AJ, 139, 2097

Peter, A. H. G., Rocha, M., Bullock, J. S., & Kaplinghat, M. 2013, MNRAS, 430, 105

Phinney, E. S. 2001, arXiv e-prints, astro, astro-ph/0108028

Planck Collaboration, Aghanim, N., Akrami, Y., Ashdown, M., et al. 2019a, arXiv e-prints, arXiv:1907.12875

Planck Collaboration, Ade, P. A. R., Aghanim, N., et al. 2016, A&A, 594, A13

Planck Collaboration, Aghanim, N., Akrami, Y., et al. 2018, arXiv e-prints, arXiv:1807.06209

Planck Collaboration, Akrami, Y., Arroja, F., et al. 2019b, arXiv e-prints, arXiv:1905.05697

Quinlan, G. D. 1996, New Astronomy, 1, 35

Randall, L., & Sundrum, R. 1999, Phys. Rev. Lett., 83, 4690

Randall, S. W., Markevitch, M., Clowe, D., Gonzalez, A. H., & Bradač, M. 2008, Astrophys. J., 679, 1173

Riess, A. G., Macri, L. M., Hoffmann, S. L., et al. 2016, ApJ, 826, 56

Robertson, A., Massey, R., & Eke, V. 2017, MNRAS, 465, 569

Rocha, M., Peter, A. H. G., Bullock, J. S., et al. 2013, MNRAS, 430, 81

Rodriguez, C., Taylor, G. B., Zavala, R. T., et al. 2006, ApJ, 646, 49

Rubin, V. C., Ford, W. K., J., & Thonnard, N. 1980, ApJ, 238, 471

Ryu, T., Perna, R., Haiman, Z., Ostriker, J. P., & Stone, N. C. 2018, MNRAS, 473, 3410

Sakstein, J., & Jain, B. 2017, Physical Review Letters, 119, 251303

Salvatier, J., Wiecki, T. V., & Fonnesbeck, C. 2016, PeerJ Computer Science, 2, e55

Sampson, L., Cornish, N. J., & McWilliams, S. T. 2015, Phys. Rev. D, 91, 084055

Schutz, B. F. 1986, Nature, 323, 310

Secco, L. F., Farah, A., Jain, B., et al. 2018, Astrophys. J., 860, 32

Seo, H.-J., Siegel, E. R., Eisenstein, D. J., & White, M. 2008, ApJ, 686, 13

Sesana, A., & Khan, F. M. 2015, MNRAS, 454, L66

Sesana, A., Shankar, F., Bernardi, M., & Sheth, R. K. 2016, MNRAS, 463, L6

Sesana, A., Vecchio, A., & Colacino, C. N. 2008, MNRAS, 390, 192

Shankar, F., Bernardi, M., Sheth, R. K., et al. 2016, MNRAS, 460, 3119

Shen, Y., Liu, X., Greene, J. E., & Strauss, M. A. 2011a, ApJ, 735, 48

Shen, Y., Richards, G. T., Strauss, M. A., et al. 2011b, ApJS, 194, 45

Skillman, S. W., Warren, M. S., Turk, M. J., et al. 2014, arXiv e-prints, arXiv:1407.2600

Slosar, A., Hirata, C., Seljak, U., Ho, S., & Padmanabhan, N. 2008, J. Cosmology Astropart. Phys., 2008, 031

Spergel, D., Gehrels, N., Breckinridge, J., Donahue, M., et al. 2013, arXiv e-prints, arXiv:1305.5425

Spergel, D. N., & Steinhardt, P. J. 2000, Phys. Rev. Lett., 84, 3760

Spergel, D. N., Verde, L., Peiris, H. V., et al. 2003, ApJS, 148, 175

Springel, V., Di Matteo, T., & Hernquist, L. 2005, ApJ, 620, L79

Springel, V., Pakmor, R., Pillepich, A., et al. 2018, MNRAS, 475, 676

Stark, D. V., McGaugh, S. S., & Swaters, R. A. 2009, AJ, 138, 392

Sun, A.-L., Greene, J. E., & Zakamska, N. L. 2017, ApJ, 835, 222

Sunyaev, R. A., & Zeldovich, Y. B. 1970, Ap&SS, 7, 3

Swaters, R. A., van Albada, T. S., van der Hulst, J. M., & Sancisi, R. 2002, A&A, 390, 829

Taylor, S. R., Vallisneri, M., Ellis, J. A., et al. 2016, ApJL, 819, L6

Tortora, C., Koopmans, L. V. E., Napolitano, N. R., & Valentijn, E. A. 2018, MNRAS, 473, 2324

Tulin, S., & Yu, H. B. 2018, Phys. Rep., 730, 1

Tully, R. B., Courtois, H. M., & Sorce, J. G. 2016, AJ, 152, 50

Tully, R. B., & Fisher, J. R. 1977, A&A, 500, 105

Verlinde, E. 2017, SciPost Physics, 2, 016

Vikram, V., Cabré, A., Jain, B., & Vand erPlas, J. T. 2013, J. Cosmology Astropart. Phys., 2013, 020

Visinelli, L., Bolis, N., & Vagnozzi, S. 2018, Phys. Rev. D, 97, 064039

Volonteri, M., Haardt, F., & Madau, P. 2003, ApJ, 582, 559

Woo, J.-H., Cho, H., Husemann, B., et al. 2014, MNRAS, 437, 32

Xu, D., & Komossa, S. 2009, ApJL, 705, L20

York, D. G., Adelman, J., Anderson, John E., J., et al. 2000, AJ, 120, 1579

Yu, Q., & Tremaine, S. 2003, ApJ, 599, 1129

Zaldarriaga, M., & Harari, D. D. 1995, Phys. Rev. D, 52, 3276

Zhu, X.-J., Cui, W., & Thrane, E. 2019, MNRAS, 482, 2588

Zwicky, F. 1933, Helvetica Physica Acta, 6, 110